Winter 2009

Light Scattering in Ultracold High Density Rubidium Vapor

Salim Balik
Old Dominion University

Recommended Citation

Balik, Salim. "Light Scattering in Ultracold High Density Rubidium Vapor" (2009). Doctor of Philosophy (PhD), dissertation, Physics, Old Dominion University, DOI: 10.25777/y6yw-z292
https://digitalcommons.odu.edu/physics_etds/21

LIGHT SCATTERING IN ULTRACOLD HIGH DENSITY RUBIDIUM VAPOR

by

Salim Balik
B.S. June 2000, Bogazici University
M.S. May 2004, Old Dominion University

A Dissertation Submitted to the Faculty of
Old Dominion University in Partial Fulfillment of the
Requirement for the Degree of

DOCTOR OF PHILOSOPHY

PHYSICS

OLD DOMINION UNIVERSITY
December 2009

Approved by:

Mark D. Havey (Director)

Gail Dodge

Charles Sukenik

Anatoly Radyushkin

Mecit Cetin

ABSTRACT

LIGHT SCATTERING IN ULTRACOLD HIGH DENSITY RUBIDIUM VAPOR

Salim Balik
Old Dominion University, 2009
Director: Dr. Mark D. Havey

Recent developments in laser cooling and trapping opened the door to a world full of new opportunities for research in atomic, molecular and optical physics as well as condensed matter physics. It became possible to do experiments under conditions that are hard to achieve in condensed matter systems but recently have been observed in atomic systems. Bose Einstein Condensation, the Mott insulator transition, and superfluidity are examples of such achievements. Another considerable interest to both condensed matter and atomic physics is Anderson localization of light. The localization phenomenon is named after P. W. Anderson who suggested the possibility of localization of electrons in a disordered medium. Localization of light is an interference effect in a disordered medium and there have been a number of observations in different types of media. It has still not been observed in atomic systems in three dimensions. We report experimental results obtained from an ultracold ^{87}Rb gas of atoms near the localization limit from the F=2 to F=3 transition. I will discuss the sample formation, characterization of the sample and the progress made towards achievement of light localization in an ultracold atomic gas, including difficulties which so far have frustrated observation.

ACKNOWLEDGMENTS

I owe a great debt of gratitude to my advisor Dr. Mark Havey for giving me the chance to work with him. I have learned a great deal not only from his advice but also from watching him working in the lab. This dissertation work could not have been completed without his continuous support, guidance and patience. I would like to especially thank Dr. Charles Sukenik for offering guidance and thoughtful training. He was always there to help with his experience and insights. I am indebted to him for providing us with his equipment on loan whenever we needed it. I would also like to acknowledge the contributions of my other committee members, Dr. Gail Dodge, Dr. Anatoly Radyushkin and Dr. Mecit Cetin.

I would like to thank many graduate students with whom I have had the privilege to work with. I would like to thank Dr. Pasad Kulatunga for his help and guidance when I first joined the group. I would like to thank Dr. Rocio Gisel Olave for her friendship, for always being helpful and supportive as a member of the research group and for the valuable conversations we have had over the years. I also would like to thank Aye Lu Win for his help in data acquisition. I am confident that he will move the research forward and be successful. I thank Jack Mills, Oguz Er and Chris Hopper for their help and friendship. I also thank Minarni, Michael Shaffer, Gambhir Ranjit, Eman Ahmed, Serkan Golge, Islam Bedir and Bayram Torayev for their continuous friendship. This work would not have been possible without them.

I also would like to give special thanks to my wife Meral for always being supportive and patient. I could not have made it through graduate school without her. I am thankful to my daughters Hilal and Neval for being in my life. They have always brought comfort, peace and joy in my life even in the most stressful moments. I also would like express my sincere thanks to Mustafa and Yeter Canan for their continuous support and help. I am thankful to my parents, my brother Zuhtu and my sisters Hatice and Fati and my other family members. Without them this would have not been possible.

TABLE OF CONTENTS

Page

Chapter

APPENDICES

LIST OF TABLES

LIST OF FIGURES

CHAPTER I

INTRODUCTION

I.1 LIGHT SCATTERING

Light scattering is observed in many different aspects of life. Light scattering occurs when light passes through solids, liquids or gases. For example Rayleigh scattering, which is named after the English physicist Lord Rayleigh, is the quasi-elastic scattering of light that is responsible for the blue sky during the day and red-yellow-blue color gradient during the sunrise and the sunset. Rayleigh predicted the λ^{-4} wavelength dependence of light scattering which causes the shorter wavelength blue color to be scattered more than other colors that results in the richly colored views of the sky. People also use light scattering as a tool in art, medical imaging, photography, radars and in spectacular laser shows.

In the context of this thesis, light scattering is a fundamental physical process which has attracted scientists' attention for centuries. Many physicists, including Planck, Einstein, Compton, Bragg, Rayleigh, Raman and Mie in the early days of quantum mechanics studied light-matter interactions and contributed to current understanding of light scattering. For example Max Planck in 1899 indicated first that light might be quantized and he modeled the blackbody radiation. Later, in 1905 Albert Einstein published his famous theory of the photoelectric effect which introduced the "photon", a discrete quantum of light. Another example is from the 21st century, as Roy J. Glauber won the Nobel prize in 2005 for his contributions to the quantum theory of optical coherence. One might think that light scattering would be fully understood by now but this is not the case. There are still mysteries in the field of light scattering waiting for the right time to be discovered.

In Rodney Loudon's *"The Quantum Theory of Light"* light scattering is expressed as a second order process in which the destruction of a photon of energy $\hbar w$ from the incident beam is followed by the creation of a photon of energy $\hbar w_{sc}$ in the scattered beam. The scattering process takes place for all frequency values of the incident beam but it is strongest for the frequencies closer to the resonance frequency of the particular atomic transition [1].

The scattered light is divided into two broad categories; quasi-elastic and inelastic.

This disertation follows the style of *The Physical Review*

The elastic component, or the Rayleigh contribution to the scattered field, comes from the light where the frequency w_{sc} essentially equals the incident frequency w. The inelastic contributions include all of the remaining components of w_{sc} different from the incident frequency w. If, after the light scattering process, the atom is left in a different state than before the scattering, the process is called inelastic Raman scattering. In this thesis we are mostly dealing with quasi-elastic light scattering from the ^{87}Rb D_2 $F = 2 \rightarrow F' = 3$ closed transition and inelastic contribution of the components of the scattered light are usually minimal.

I.2 MULTIPLE SCATTERING

This thesis specifically deals with the multiple scattering of light in a medium of spatially random atomic scatterers where light propagation involves many free propagation and scattering events. Usually multiple scattering from such disordered systems is a difficult problem, especially if the complex internal quantum mechanical nature of the atomic gases is involved. Early studies of multiple scattering of light mostly were in the area of "radiation trapping", and directed toward the study of radiation transport in stellar atmospheres. The name radiation trapping comes from the fact that the light spends a lot more time in the medium than the ballistic propagation time for leaving the medium. This is because light performs, in many cases, a random walk inside a disordered medium rather than ballistically escaping through the boundaries of the sample. The time frame that the light is "trapped" inside the medium is usually much longer for atomic systems because light scattering from atoms is scattering dominated in contrast to other media where it is free propagation dominated [2].

Multiple scattering of light in a disordered medium is generally considered to be equivalent to diffusion of light. The language that is used to describe the diffusion and multiple scattering is largely interchangeable in the context of this thesis. The dynamics of the radiation in the medium is characterized by the mean free path ℓ, the average distance between two scattering events, which for a dilute gas depends only on the light scattering cross section σ and the density of the medium n as given by $\ell = 1/n\sigma$. When the mean free path is much larger than the wavelength of the light λ divided by 2π, $\ell \gg \lambda/2\pi$, the motion of light satisfies the diffusion equation

$$D\nabla J = -J \tag{1}$$

where

$$D = \frac{1}{3} v_{tr} \ell. \tag{2}$$

Here D is defined as the diffusion coefficient, v_{tr} is the transport velocity and J is the average current of radiation which satisfies the continuity equation [3],

$$\frac{\partial I}{\partial t} = -\nabla \cdot J. \tag{3}$$

One important point in Eq. 2 is that the transport velocity v_{tr} (sometimes it is referred to as v_E in the literature [2]) is much smaller than the phase velocity due to the fact that the Wigner time delay [4], the time spent by the light inside the single scattering region, is much longer than the time it takes for light to travel from one scattering site to another with group velocity $v_g \sim c$. Here c is the speed of light in vacuum. The diffusion coefficient decreases as the transport velocity v_{tr} and the mean free path ℓ decreases.

This approach clearly neglects all of the interference effects between multiply scattered waves. These interference effects increase the probability of recurrent scattering, in which scattering paths form closed loops and interferometrically decrease the diffusion coefficient D. When the amount of disorder in the system reaches a critical level the diffusion coefficient becomes zero and the diffusion of light stops, this effect is called the localization of light. Note that localization is purely an interference effect and in this regime the diffusion theory is inadequate to describe radiative transport in the system.

I.3 LOCALIZATION OF LIGHT

The term localization is generally used in two contexts of research among those of the atomic, molecular and optical physics (AMO) and condensed matter physics community who study light scattering. One is called weak localization of light, which occurs in a medium where the mean free path ℓ is much larger than the wavelength of the light. The name weak localization comes from the fact that interference effects, which are considered the building blocks of the light localization, reveal themselves in a fascinating phenomenon called coherent backscattering of light. Coherent backscattering can be observed when light scatters many times in a disordered medium. Because of time-reversal symmetry every path of light has a counter-propagating partner. When the phase accumulation along these two paths are equal they usually constructively interfere. One spatial zone where these paths constructively interfere is the backwards direction. This interference effect leads to a cone shaped intensity enhancement in the backwards direction. The coherent backscattering event has been observed in many systems from solid state samples to ultracold samples. Coherent backscattering of light was first reported in 1984 in the condensed matter community [5–7]. First reports of measurements of coherent backscattering from ultracold atomic samples were made by the Kaiser group in 1999 [8, 9]. Since then many theoretical and experimental studies have been done to investigate the magnetic field, spectral variations, polarization, optical saturation and time dependence of coherent backscattering of light [10–21].

Even though coherent backscattering is termed weak localization of light, it is not a real localization effect in the sense that was first proposed by P.W. Anderson *et al* (1958) [22]. In his famous article of *"Absence of Diffusion in Certain Random Lattices"* he suggested that beyond a critical amount of impurity scattering, electron diffusion in conductors will come to a halt and the material becomes an insulator. Last year was the 50th anniversary of his theory of localization, from which all general localization phenomenon caused through interference are termed Anderson localization.

The transition to Anderson localization, as formulated by Ioffe and Regel [23], is expected to happen when the dimensionless parameter $k\ell$ is approximately equal to one, where the wavevector k is given by $k = 2\pi/\lambda$. According to this criteria, localization happens in a regime where the mean free path ℓ is smaller than a characteristic wavelength. This may be the optical wavelength in the medium, sound wavelength or the de Broglie wavelength in the case of matter waves.

Anderson's paper on localization of electrons stimulated a great amount of theoretical and experimental studies, especially in solid state physics. In the theory of Anderson localization of electrons, the repulsive electron-electron interactions are neglected. Inclusion of these lead to another type of phase transition, the Mott-insulator transition [24]. Since electromagnetic waves do not interact with each other, light propagation in a disordered medium becomes an ideal candidate for localization studies. Since the 1980s there has been great amount of effort to experimentally observe Anderson localization of light. Initial experiments looked for a faster decay of the transmission of light than $\propto 1/L$, the rate in a diffusive medium. Here L is the thickness of the medium. First experimental results in three-dimensional localization of light came from the condensed matter physics community. Wiersma *et al.* claimed in a Nature article the first experimental observation of light localization in semiconductor GaAs powders [25]. The results that they presented as evidence for Anderson localization are questioned by some physicists who argue that absorption leads to a similar result as localization. A different approach may be needed to observe unambiguously the signatures of Anderson localization. In more recent experiments, Maret's group examined the time evolution of transmission of light through bulk powders of TiO_2 with $k\ell$ values as low as 2.5 [26–28]. Their results exhibit a strong deviation from diffusive transmission that can not readily be explained by absorption. Other experimental realizations of Anderson localization include the transverse localization for a 2D lattice by Schwartz et al. and a 1D lattice by Lahini et al. [29, 30]. Recently Hu et al. reported the Anderson localization of ultrasonic waves in a 3D disordered medium [31]. Anderson localization of matter waves in one dimension has been recently reported in Bose-Einstein condensates subjected to a disordered potential by Roati et al. and Billy et al. [32, 33].

Recent developments in laser cooling and trapping of atoms have opened new opportunities for research in the atomic, molecular and optical physics community. It has become became possible to do experiments under conditions that are hard to achieve in condensed matter systems but recently have been observed in atomic systems. Bose Einstein Condensation, the Mott insulator transition, and superfluidity are examples of such achievements [34–36]. Another considerable interest to both condensed and atomic physics is Anderson localization of light. Ultracold atomic gases are basically absorption free systems which makes them ideal for localization studies. Moreover, ultracold atomic systems provide tunable experimental parameters that makes it possible to exert precise control of the physical system.

In this dissertation we first present basic theoretical aspects of light scattering, coherent backscattering, Anderson localization and laser cooling and trapping. Then the instrumentation of the experimental apparatus is described in detail in Chapter III. Some technical details and drawings related to experimental instrumentation are given in the Appendix at the end of this thesis. The sample characterization procedures and techniques will be explained in Chapter IV. The results and the analysis of the experimental results will be presented Chapter V. The thesis will end with discussion and conclusions based on the experimental results.

CHAPTER II

THEORETICAL BACKGROUND

In this chapter I present some simplified models of results that are needed in analysis and interpretation of the experiments. An important approximation made throughout is that the applied radiation is described as a classical field. The interaction with the atoms, which are described quantum mechanically, is taken to be electric dipole.

II.1 TWO LEVEL ATOM

To understand the light scattering from a collection of atoms it is first necessary to consider the light scattering from a single atom. Let us now consider the near resonant light scattering so we can ignore the other transitions and consider the atom in a two-level approximation. The time dependent Schrödinger equation is

$$H|\psi\rangle = i\hbar\frac{\partial}{\partial t}|\psi\rangle \tag{4}$$

where H is the Hamiltonian in the existence of a perturbation V,

$$H = H_0 + V. \tag{5}$$

First we expand the wavefunctions, which form a complete set, as

$$|\psi\rangle = \sum_k a_k(t)|k\rangle e^{-iw_k t} \tag{6}$$

where $|k\rangle$ are the eigenstates of the unperturbed Hamiltonian, H_0 with $E_k = \hbar w_k$ are the eigenenergies;

$$H_0|k\rangle = \hbar w_k|k\rangle. \tag{7}$$

These states are also normalized and orthogonal,

$$\langle k|n\rangle = \delta_{kn} \tag{8}$$

$a_k(t)$ are the time dependent probability amplitudes of the respective states with

$$\sum_k |a_k(t)|^2 = 1 \tag{9}$$

and $|a_k(t)|^2$ is the probability of finding the atom in state $|k\rangle$. Substituting Eq. 6 in Eq. 4 gives,

$$(H_0 + V)|\psi\rangle = i\hbar\sum_k(\dot{a}_k(t)|k\rangle e^{-iw_k t} - iw_k a_k(t)|k\rangle e^{-iw_k t}). \tag{10}$$

This yields

$$\dot{a}_k(t) = -\frac{i}{\hbar}\sum_k a_k(t)\langle n|V|k\rangle e^{-iw_{kn}t} \tag{11}$$

where

$$w_{kn} = w_k - w_n. \tag{12}$$

In the case of an electric dipole interaction between the light and the atom the interaction operator is given by

$$V = -\mathbf{d}\cdot\mathbf{E}(t) \tag{13}$$

where $\mathbf{d}$ is the electric dipole moment operator of the atom,

$$\mathbf{d} = -e\mathbf{r} \tag{14}$$

and $\mathbf{E}$ is the classical electric field of the light,

$$\mathbf{E} = E_0\hat{\epsilon}\cos(kz - wt). \tag{15}$$

Here $\hat{\epsilon}$ is the polarization vector of the monochromatic light with an amplitude E_0 having angular frequency w and traveling in the z direction. Here text in bold represents a vector operator. We will ignore the spatial dependence of the field because the size of the atom is much smaller than the wavelength of the light. Spatially distributed collective interactions are thus ignored. The interaction operator can also be written as,

$$V = eE_0\left(\frac{e^{iwt} + e^{-iwt}}{2}\right)\hat{\epsilon}\cdot\mathbf{r}. \tag{16}$$

It is important to note here that in first order perturbation treatment of this problem because of the odd parity of the V operator, only the off diagonal matrix elements in Eq. 11 survive.

Now if we go back to the case of a two level atom under the influence of the light field where the ground state is defined as $|0\rangle$ and the excited state is $|1\rangle$ with associated unperturbed energies of $E_0 = \hbar\omega_0$ and $E_1 = \hbar\omega_1$, Eq. 11 can be written as

$$\dot{a}_0(t) = -\frac{i}{\hbar}eE_0a_1(t)\frac{\langle 0|\hat{\epsilon}\cdot\mathbf{r}|1\rangle}{2}(e^{i(w-w_{10})t} + e^{-i(w+w_{10})t}) \tag{17}$$

and

$$\dot{a}_1(t) = -\frac{i}{\hbar}eE_0a_0(t)\frac{\langle 1|\hat{\epsilon}\cdot\mathbf{r}|0\rangle}{2}(e^{i(w+w_{10})t} + e^{-i(w-w_{10})t}). \tag{18}$$

Now it is useful to introduce the Rabi frequency which is defined as,

$$\Omega_{kn} = \frac{eE_0}{\hbar}\langle n|\hat{\epsilon}\cdot \mathbf{r}|k\rangle. \tag{19}$$

If we consider the light field is weak such that

$$a_1(t) \sim 0 \quad \text{and} \quad a_0(t) \sim 1 \tag{20}$$

and

$$a_1(0) = 0 \quad \text{and} \quad a_0(0) = 1 \tag{21}$$

we can solve for $a_1(t)$, the excited state probability amplitude as

$$a_1(t) = -\frac{i\Omega}{2}\int_o^t (e^{i(w+w_{10})t} + e^{-i(w-w_{10})t})dt. \tag{22}$$

The result of the integration is

$$a_1(t) = -\frac{i\Omega}{2}\left[\frac{e^{i(w+w_{10})t} - 1}{i(w+w_{10})} + \frac{e^{-i(w-w_{10})t}}{-i(w-w_{10})}\right]. \tag{23}$$

For the near resonant light scattering, the light field angular frequency w is close to w_{10} and we can make rotating wave approximation (RWA). We assume

$$w + w_{10} \gg |w - w_{10}| \tag{24}$$

and the second term dominates the equation. Dropping the first term we get

$$a_1(t) = \Omega\frac{e^{i(w-w_{10})t/2}}{(w-w_{10})}\left[\frac{e^{i(w-w_{10})t/2} - e^{-i(w-w_{10})t/2}}{2}\right]. \tag{25}$$

The transition probability of the atom started in the ground state to be found in the excited state at time t is then given by

$$P_1(t) = |a_1(t)|^2 = |\Omega|^2\frac{\sin^2[(w-w_{10})t/2]}{(w-w_{10})^2}. \tag{26}$$

II.2 LIGHT SHIFT

In the presence of the light field the energy levels of the atom are shifted. The light shift can be found by replacing the probability amplitudes $a_0(t)$ and $a_1(t)$ in Eqs. 17, 18 by

$$\tilde{a}_0(t) = a_0(t) \tag{27}$$

and

$$\tilde{a}_1(t) = a_1(t)e^{i(w-w_{10})t}. \tag{28}$$

After making the RWA in Eqs. 17, 18, substituting the Rabi frequency Ω and defining

$$\delta = w - w_{10} \tag{29}$$

we have

$$\dot{a}_0(t) = -ia_1(t)\frac{\Omega}{2}e^{i\delta t} \tag{30}$$

and

$$\dot{a}_1(t) = -ia_0(t)\frac{\Omega}{2}e^{-i\delta t}. \tag{31}$$

Differentiating Eqs. 27, 28 with respect to time gives

$$\dot{\tilde{a}}_0(t) = \dot{a}_0(t) \tag{32}$$

and

$$\dot{\tilde{a}}_1(t) = \dot{a}_1(t)e^{i\delta t} + i\delta a_1(t)e^{i\delta t}. \tag{33}$$

After substituting Eqs. 27, 28, 32 and 33 into Eqs. 30 and 31, we can bring these two equations in the following form:

$$\begin{aligned} i\hbar\dot{\tilde{a}}_0(t) &= \frac{\hbar\Omega}{2}\tilde{a}_1(t) & (34)\\ i\hbar\dot{\tilde{a}}_1(t) &= \frac{\hbar\Omega}{2}\tilde{a}_0(t) - \hbar\delta\tilde{a}_1(t). & (35)\end{aligned}$$

The Eqs. 35 and 34 in the matrix form is,

$$i\hbar\frac{d}{dt}\begin{pmatrix}\tilde{a}_0(t)\\ \tilde{a}_1(t)\end{pmatrix} = \begin{pmatrix}0 & \frac{\hbar\Omega}{2}\\ \frac{\hbar\Omega}{2} & -\hbar\delta\end{pmatrix}\begin{pmatrix}\tilde{a}_0(t)\\ \tilde{a}_1(t)\end{pmatrix}. \tag{36}$$

The eigenenergies of the the system are given by

$$\begin{aligned} E_{0,1} &= \frac{\hbar}{2}\left(-\delta \pm \sqrt{\delta^2+\Omega^2}\right)\\ &= \frac{\hbar}{2}\left(-\delta \pm \delta\sqrt{1+\Omega^2/\delta^2}\right) & (37)\end{aligned}$$

In the limit where $\Omega \ll |\delta|$ the term in the square root can be expanded by utilizing the binomial theorem and the energy shift due to the light field becomes,

$$E_{0,1} = \pm\frac{\hbar\Omega^2}{4\delta} \tag{38}$$

In real atoms the energy level structure is more complex than that is described here. The generalized multi level atom energy shift of level i without the rotating wave approximation is given by [37]

$$E_i = -\frac{E_0^2}{4\hbar}\sum_{i\neq f}|\langle i|\hat{\epsilon}\cdot \mathbf{r}|f\rangle|^2\left(\frac{1}{w_{if}-w}+\frac{1}{w_{if}+w}\right). \tag{39}$$

II.3 SPONTANEOUS EMISSION

So far in the derivations the damping of the excited state is ignored. In the absence of atomic collisions this damping is called the spontaneous emission rate or excited state decay rate. Relaxation processes are more properly treated through a density matrix approach to the atomic populations and coherence. However, it is sufficient here to treat the basic interactions between the electromagnetic field and the atoms as explained in a phenomenological theory made by Einstein [1]. According to this theory there are three fundamental interactions between light and atoms; absorption, stimulated and spontaneous emission. The absorption and the stimulated emission coefficients $B_{12}=B_{21}$ for the two level atom that is treated quantum mechanically in this section. Now we will consider that the light is turned off at time t = 0 and the excited state population N_2 is allowed to decay to the ground state. Note that in this section energy levels are labeled as 0 and 1 but to keep the notation parallel with the literature, 1 and 2 will be used to identify the levels when Einstein coefficients and rate equations are mentioned. The rate equation for N_2 is

$$\frac{dN_2}{dt} = -N_2A_{21} \tag{40}$$

where A_{21} is the Einstein coefficient for spontaneous emission. The excited state population decays as

$$N_2 = N_2(0)e^{-t/\tau} \tag{41}$$

where the time constant $\tau = 1/A_{21}$. Here τ is called the radiative lifetime of the excited state and $A_{21} = \gamma$ is the natural linewidth of the excited state,

$$\gamma = A_{21} = B_{12}\left(\frac{\hbar\omega^3}{\pi^2c^3}\right). \tag{42}$$

We now introduce the mean energy density of radiation of an applied field as $\langle W\rangle$ at frequency w,

$$P_1(t) = |a_1(t)|^2 = B_{12}\langle W\rangle t \tag{43}$$

where $\langle W\rangle = I/c$ [1]. This equation defines the relation between the excitation/absorption rate and probability. Here I is the intensity of the radiation which is given for an incident plane wave as

$$I = \frac{1}{2}\epsilon_0 c|E|^2 = \frac{|E|^2}{2\mu_0 c}. \tag{44}$$

The mean energy density of the radiation $\langle W\rangle$ becomes

$$\langle W\rangle = \frac{1}{2}\epsilon_0|E|^2 = \frac{|E|^2}{2\mu_0 c^2}. \tag{45}$$

Then Eq. 42 can be written as,

$$\gamma = A_{21} = \frac{|a_1(t)|^2}{\langle W\rangle t}\left(\frac{\hbar\omega^3}{\pi^2 c^3}\right). \tag{46}$$

In the derivation of $|a_1(t)|^2$ we assumed the w_{10} is an exact value. It does not include the statistical spread of the width of the transition, γ. The correct form of the excitation probability is

$$P_1(t) = |a_1(t)|^2 = \Omega^2\int_{-\infty}^{+\infty}\frac{\sin^2[(w-w_{10})t/2]}{(w-w_{10})^2}dw. \tag{47}$$

To solve the integral we make a change of variables, $(w-w_{10})t/2 = x$. Then with $dx = t/2dw$ the integral becomes

$$\frac{t}{2}\int_{-\infty}^{+\infty}\frac{sin^2 x}{x^2}dx = \pi\frac{t}{2}. \tag{48}$$

Then Eq. 47 can be written as

$$|a_1(t)|^2 = \Omega^2\pi\frac{t}{2}. \tag{49}$$

Before writing the excited state population decay γ, we need to average over the random spatial orientations of the transition dipole moment. The Rabi frequency can then be written as

$$\langle\Omega^2\rangle = \frac{2e^2}{3\epsilon_0\hbar^2}|\langle 1|r|0\rangle|^2\langle W\rangle. \tag{50}$$

Now we can write the excitation probability as

$$|a_1(t)|^2 = \frac{2\mu^2}{3\varepsilon_0\hbar^2}\langle W\rangle\pi\frac{t}{2} \tag{51}$$

where we defined $\mu = e\langle 1|r|0\rangle$. From Eqs. 51 and 46 the excited state population decay rate γ becomes

$$\gamma = \frac{w^3\mu^2}{3\pi\epsilon_0\hbar c^3} \tag{52}$$

The amplitude of the excited state decays at a rate $\gamma/2$ to ensure the population decays with γ. Now we can rewrite the amplitude equations Eqs. 30 and 31 by adding an additional damping term $-\gamma/2a_1(t)$ to the right side of $\dot{a}_1(t)$ equation as

$$\dot{a}_0(t) = -ia_1(t)\frac{\Omega}{2}e^{i(w-w_{10})t} \tag{53}$$

and

$$\dot{a}_1(t) = -ia_0(t)\frac{\Omega}{2}e^{-i(w-w_{10})t} - \frac{\gamma}{2}a_1(t). \tag{54}$$

Again we make weak field approximation, $a_0(t) \sim 1$. To solve these equations let us define

$$\begin{aligned} \tilde{a}_1 &= a_1 e^{\gamma t/2} && (55) \\ \dot{\tilde{a}}_1 &= \dot{a}_1 e^{\gamma t/2} + \frac{\gamma}{2}a_1 e^{\gamma t/2} \\ \dot{a}_1 &= \dot{\tilde{a}}_1 e^{-\gamma t/2} - \frac{\gamma}{2}a_1. && (56) \end{aligned}$$

A comparison between Eq. 56 and Eq. 54 gives

$$\begin{aligned} \dot{\tilde{a}}_1(t) &= -i\frac{\Omega}{2}e^{(-i(w-w_{10})+\gamma/2)t} \\ \tilde{a}_1(t) &= -i\frac{\Omega}{2}e^{\gamma t/2}\frac{e^{-i(w-w_{10})t}}{-i(w-w_{10})+\gamma/2} && (57) \end{aligned}$$

where we made an indefinite integration. From Eq. 57 and 55 the amplitude equations become,

$$\begin{aligned} a_0(t) &\sim 1 && (58) \\ a_1(t) &= \frac{\Omega}{2}\frac{e^{-i(w-w_{10})t}}{(w-w_{10})+i\gamma/2}. && (59) \end{aligned}$$

II.4 LIGHT SCATTERING CROSS SECTION

Now we turn to a macroscopic electrodynamical treatment of an isotropic, homogenous dilute gas of atoms. We will relate the dipole moment of a single atom to the polarization of the gas which will be useful in coming sections. The index of refraction of the medium is a complex quantity and it is given by

$$n = n_r + in_i. \tag{60}$$

For a plane wave

$$\mathbf{E} = \hat{\epsilon}E_0 e^{i(\mathbf{k}\cdot\mathbf{r}-wt)} \tag{61}$$

where $\mathbf{k} = \frac{w}{c} n\hat{\mathbf{k}}$ and for $\hat{\mathbf{k}} = \hat{\mathbf{z}}$ we can write $\mathbf{E}$ as

$$\mathbf{E} = \hat{\epsilon} E_0 e^{i\frac{w}{c}n_r} e^{-iwt} e^{-\frac{w}{c}n_i z}. \tag{62}$$

So the Poynting vector equals

$$I = \epsilon_0 c^2 \langle \mathbf{E} \times \mathbf{B} \rangle = \frac{E_0^2}{2\mu_0 c} e^{-\frac{2w}{c}n_i z}. \tag{63}$$

This equation describes the attenuation of the initial intensity of the light field $I_0 = E_0^2/2\mu_0 c$ as it travels through the medium. The absorption coefficient of the medium is defined as

$$\kappa = \frac{2w}{c} n_i \tag{64}$$

and the optical depth is defined as $b = \kappa z$ such that

$$I = I_0 e^{-b}. \tag{65}$$

The relation between the complex dielectric function $\varepsilon(w)$ and index of refraction n is given by

$$(n_r + in_i)^2 = \varepsilon(w) = 1 + \chi(w) \tag{66}$$

where $\chi(w)$ is the linear susceptibility [1] which is related to the polarization density $\mathbf{P}$ as

$$\mathbf{P} = \epsilon_0 \chi(w) \mathbf{E}. \tag{67}$$

Now Eq. 66 becomes

$$(n_r^2 - n_i^2) + i2n_r n_i = 1 + \chi(w). \tag{68}$$

If we write $\chi(w) = \chi_r(w) + i\chi_i(w)$ then the real and imaginary parts of the susceptibility are

$$\chi_r(w) = n_r^2 - n_i^2 - 1 \tag{69}$$

$$\chi_i(w) = 2n_r n_i. \tag{70}$$

From Eqs. 69 and 70 it follows that

$$n_r = 1 + \frac{1}{2}\chi_r(w) \tag{71}$$

$$n_i = \frac{1}{2}\chi_i(w) \tag{72}$$

The total polarization of the medium $P(t)$ is given by the expectation value of the dipole moment $p(t)$ as

$$P(t) = Np(t) = N\langle \psi | -e\hat{\epsilon} \cdot \mathbf{r} | \psi \rangle \tag{73}$$

where

$$|\psi\rangle = a_0(t)|0\rangle e^{-iw_0t} + a_1(t)|1\rangle e^{-iw_1t}. \tag{74}$$

Here N is the number density. Then

$$\langle p(t)\rangle = -e\left(a_0^*(t)\langle 0|e^{iw_0t} + a_1^*(t)\langle 1|e^{iw_1t}\right)\hat{\epsilon}\cdot\mathbf{r}\left(a_0(t)|0\rangle e^{-iw_0t} + a_1(t)|1\rangle e^{-iw_1t}\right). \tag{75}$$

Again the diagonal matrix elements vanish because of the odd parity of position operator and as a result the polarization is

$$\langle p(t)\rangle = -e\left(a_0^*(t)a_1(t)\langle 0|\hat{\epsilon}\cdot\mathbf{r}|1\rangle e^{-iw_{10}t} + a_1^*(t)a_0(t)\langle 1|\hat{\epsilon}\cdot\mathbf{r}|0\rangle e^{iw_{10}t}\right). \tag{76}$$

If we substitute $a_1(t)$ and $a_0(t)$ from Eqs. 58 and 59 into Eq. 76 we get

$$\langle p(t)\rangle = \frac{E_0e^2|\langle 1|\hat{\epsilon}\cdot\mathbf{r}|0\rangle|^2}{2\hbar}\left(\frac{e^{-iwt}}{w_{10}-w-i\gamma/2} + \frac{e^{iwt}}{w_{10}-w+i\gamma/2}\right). \tag{77}$$

With the dipole moment $p(t)$ averaged over all directions the total polarization $P(t)$ becomes

$$\langle P(t)\rangle = \frac{NE_0e^2|\langle 1|r|0\rangle|^2}{2\hbar}\frac{1}{3}\left(\frac{e^{-iwt}}{w_{10}-w-i\gamma/2} + \frac{e^{iwt}}{w_{10}-w+i\gamma/2}\right). \tag{78}$$

From Eq. 67, the total polarization can be written as

$$\langle P(t)\rangle = \frac{1}{2}\epsilon_0E_0\chi(w)e^{-iwt} + \frac{1}{2}\epsilon_0E_0\chi^*(w)e^{iwt}. \tag{79}$$

A comparison of Eqs. 78 and 79 yields

$$\chi(w) = \frac{1}{3}\frac{Ne^2}{\epsilon_0\hbar}|\langle 1|r|0\rangle|^2\frac{1}{w_{10}-w-i\gamma/2}. \tag{80}$$

From Eq. 80 the real part of the susceptibility is

$$\chi_r(w) = \frac{1}{3}\frac{Ne^2}{\epsilon_0\hbar}|\langle 1|r|0\rangle|^2\frac{w_{10}-w}{(w_{10}-w)^2+(\gamma/2)^2} \tag{81}$$

the imaginary part of the susceptibility is

$$\chi_i(w) = \frac{1}{3}\frac{Ne^2}{\epsilon_0\hbar}|\langle 1|r|0\rangle|^2\frac{\gamma/2}{(w_{10}-w)^2+(\gamma/2)^2}. \tag{82}$$

So from the Eqs. 64, 72 and 82 the absorption coefficient κ is

$$\kappa = \frac{1}{3}\frac{Ne^2}{\epsilon_0\hbar}|\langle 1|r|0\rangle|^2\left(\frac{w}{c}\right)\frac{\gamma/2}{(w_{10}-w)^2+(\gamma/2)^2}. \tag{83}$$

The absorption coefficient can be written in this form;

$$\kappa = N\left(\frac{\lambda^2}{2\pi}\right)\frac{1}{1+(2\delta/\gamma)^2} \tag{84}$$

where we substituted γ,

$$\gamma = \frac{1}{3}\frac{w^3}{\pi\epsilon_0\hbar c^3}e^2|\langle 1|r|0\rangle|^2 \tag{85}$$

and

$$\frac{\lambda}{2\pi} = \frac{c}{w} \tag{86}$$

into Eq. 83. So far we didn't include the degeneracy of the energy levels in the derivations but to get the exact solution the ratio of the degeneracies g_1/g_0 should be included in the equations. So from $\kappa = N\sigma$,

$$\sigma = \frac{g_1}{g_0}\frac{\lambda^2}{2\pi}\frac{1}{1+(2\delta/\gamma)^2} \tag{87}$$

where σ is the light scattering cross section.

II.5 MULTIPLE LIGHT SCATTERING

Propagation of light in a dilute atomic gas can be thought of as successive scattering of light from randomly distributed scatterers (atoms). The scattered light is assumed to have a random probability to propagate in any direction. Because of this randomness, multiple scattering of light in atomic medium is generally considered as a diffusion process with a Poissonion type statistics. The main parameter to describe the diffusive medium is the mean free path ℓ. If we consider the light is performing a random walk in the medium, the mean free path is the average distance that the light travels before it experiences another scattering. The first person to treat light propagation with diffusion was Compton in 1922 [38]. Since the time that the light spends in the medium is longer than the radiative lifetime of an individual atom τ, this process is also called "radiation trapping".

In particle diffusion the density of the diffusing material at location **r** and time t is given by the diffusion equation,

$$\frac{\partial\rho(\mathbf{r},t)}{\partial t} = D\nabla^2\rho(\mathbf{r},t) \tag{88}$$

which is also called the heat flow equation. Here D is defined as the diffusion coefficient [39]. The relation between the diffusion coefficient D and the mean free path is given by

$$\begin{aligned} D &= \frac{1}{3}\frac{\ell^2}{\tau_{tr}} && (89) \\ &= \frac{1}{3} v_{tr}\ell. && (90) \end{aligned}$$

Here τ_{tr} is the average transport time per scattering event and v_{tr} is the average transport velocity of the scatterers such that

$$v_{tr} = \frac{\ell}{T_{tr}}. \qquad (91)$$

The solution to the partial differential equation is

$$\rho(\mathbf{r}, t) = \frac{1}{(4\pi Dt)^{3/2}} e^{-r^2/4Dt} \qquad (92)$$

for particles start to spread from the origin at t =0 [39].

Even though the diffusion model in general describes the light scattering processes in an atomic medium especially in ultracold samples, there are fundamental extensions required.

Among these is treatment of the quite complex atomic internal energy level structure which can give rise to inelastic scattering, in turn changes the mean free path. Another is the role of spectral redistribution of scattered light. For pure elastic scattering the step length distribution between two scattering events is given by the exponential distribution,

$$P(\mathbf{r}) = \frac{1}{\ell(w)} e^{(-r/\ell(w))} \qquad (93)$$

where $\ell(w)$ is the frequency dependent mean free path [40]. For incoherent light with inelastic spectral distribution $F(w)$, Eq. 93 is given by

$$P(\mathbf{r}) = \int dw \frac{F(w)}{\ell(w)} e^{(-r/\ell(w))}. \qquad (94)$$

Holstein pointed out that the line broadening mechanisms can give rise to a Lévy type statistical distribution of the free path distribution [40, 41],

$$P(r) \sim \frac{1}{r^{3/2}}. \qquad (95)$$

In Lévy statistics the steps of the random walk can have extremely long jumps which are also called Lévy flights [42].

There are a number of dephasing effects and inelastic processes that are important in light scattering from atomic medium. One is the Doppler broadening due to the random motion of the atoms. This effect, which completely randomizes the phase of the light after a few scattering events for atoms at room temperature, can be minimized by cooling the atoms. Even in ultracold atomic samples with high scattering orders, it is an important parameter that eventually dephases the light.

Other related dephasing occurs because of the recoil of the atom after each scattering event. In the course of light scattering, because of recoil, the phase shift in the frequency of the light performs a random walk which increases the overall phaseshift by $\sqrt{N}$ with N scattering orders, see Appendix A. In our experiments we can produce samples with optical depth b of $\sim$ 165 (10). The relation between the scattering order and optical depth in diffusion theory is given by

$$N = \frac{3}{\alpha\pi^2}b^2 \tag{96}$$

where α is a geometrical numerical factor 5.35 for inhomogeneous sphere with gaussian density profile) [2]. Here b is the optical depth of the sample which is given by

$$b = \sqrt{2\pi} n_0 \sigma r_0 \tag{97}$$

where n_0 is the peak density, r_0 is the Gaussian radius of the sample and σ is the light scattering cross section which is given by

$$\sigma = \frac{2F' + 1}{2F + 1}\frac{\lambda^2}{2\pi}\frac{1}{1 + (2\delta/\gamma)^2} \tag{98}$$

from Eq. 87. The optical depth b of $\sim$ 165 corresponds to $N > 1500$ scattering orders. When we consider a recoil shift of $\sim$ 50 kHz per scattering, the total light frequency drift is $\sim$ 2 MHz. This is only for the radial direction of the atomic sample that we obtain in our experiments. In the axial direction where the optical depth is $\sim$ 4000 the results are even more dramatic.

Some of these dephasing effects can be minimized by cooling the sample to lower temperatures but inelastic scattering components from Raman transitions and recoil shifts still exist. Under these circumstances ultracold gases with $k\ell \ll 1$ can be treated with diffusion equations. Here $k = 2\pi/\lambda$. This inequality corresponds to a mean free path length of the scattering much larger than the wavelength of the light.

Another difference of light scattering from atomic gases compared to particle diffusion is that, in particle diffusion the main contribution to the transport time comes from the propagation time between the scattering events. In the atomic case, the transport time is given by

$$\tau_{tr} = \tau_W + \frac{\ell}{v_g} \sim \tau_{nat} \tag{99}$$

where τ_W is the Wigner time delay for the scattering and ℓ/v_g is the free propagation time [2]. Here v_g is the group velocity of the light in the medium. Since the Wigner time delay $\tau_W \sim \tau_{nat} \sim 27$ ns [43] is much larger than the free propagation time $\ell/v_g \sim \ell/c \sim 1$ ps, the transport time is predicted to be essentially equal to the natural lifetime of the atom.

In the experiments described in this thesis, we are interested in time dependent light scattering measurements. This is done by sending a pulse of laser light into the sample for a period of time usually longer than the time for the system to reach the steady state. Then we look at the dynamics after the laser beam is extinguished. The diffusion coefficient in terms of $k\ell$ is given approximately by

$$D \approx D_0 \left[1 - 1/(k\ell)^2\right] \tag{100}$$

where D_0 is the diffusion coefficient for weak localization regime where $k\ell \ll 1$. In this regime where the dynamics is determined by diffusion the decay of the scattered light is interpreted as a sum of decaying exponentials each of which are called "Holstein modes." At later times, the decay is dominated by the longest lived mode where the signal decays with a single exponential time constant τ_0 which is given by

$$\tau_0 \simeq \frac{3}{\alpha\pi^2}\tau_{nat}b^2. \tag{101}$$

where α is a numerical factor whose value is 5.35 for an inhomogeneous sphere with Gaussian density distribution. From this equation and Eq. 89 it is possible to estimate the diffusion coefficient of the medium [2].

II.6 WEAK LOCALIZATION

Up to now we have ignored any interference effects that are possible in multiple light scattering. Even though light propagation in dilute atomic gases can be largely considered diffusive, interference effects play an important role. For instance, it is interference effects that gives rise to a speckle pattern in space as light passes through or scatters from a random media. Light scattered from different scatterers interferes constructively or destructively, which forms a random interference pattern depending

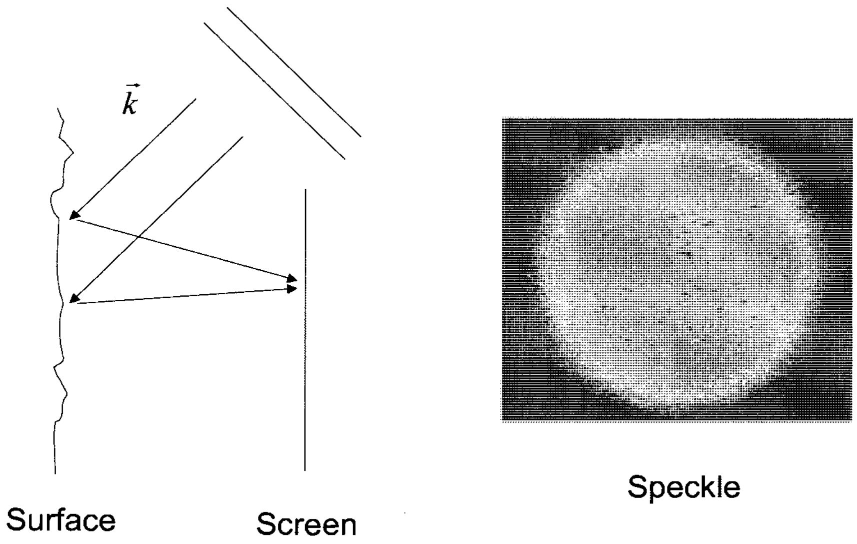

FIG. 1: Light scattered from a random surface exhibits a speckle pattern because of interference effects.

on the locations of the scatterers as shown in Fig. 1. As the locations of the scatterers are moved, different configurations forms different speckle patterns and the sum of the detected field smooths out and gives a nearly angle independent pattern.

Another manifestation of interference effects is the enhanced backscattering intensity as a result of coherent backscattering. As a result of the previous configuration averaging the speckle pattern smooths in all direction except in the backwards direction and in a narrow angular region. The enhancement shows up in the backwards direction because of constructive interference of light propagated in reverse paths that do not depend on the location of the scatterers. This effect is called coherent backscattering (CBS), which is also called weak localization of light because it is a manifestation of coherent radiative transport [6, 7, 39, 40, 44, 45].

To understand the origin of the CBS effect, we consider two paths for an incoming ray that are equally possible as shown in Fig. 2. The blue path has an extra phase of $-k_f \cdot r$ due to the extra path length at exit and the green path has an extra phase of $k_i \cdot r$ due to the extra path length at incidence. It is clear from the picture that when $k_i = -k_f$, the total phase difference between two paths is zero which causes constructive interference in the backwards direction ($\theta = 0$). This result is independent of the configuration. The total intensity in the backwards direction (at any θ) has other interference terms that depend on configuration but only the

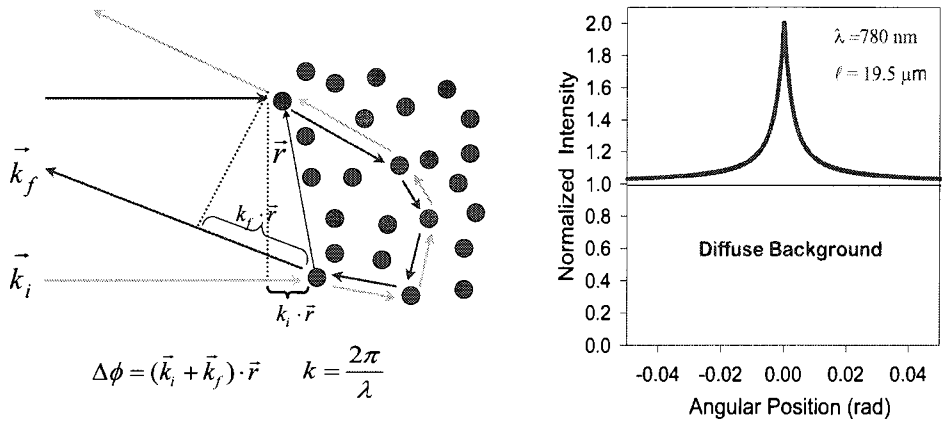

FIG. 2: Schematic illustration showing two ray paths in a scattering medium and profile of the backscattered intensity around $\theta = 0$. It has a narrow cone shaped profile with a maximum enhancement of 2 over the background.

interference at $\theta = 0$ survives configuration averaging. The backscattered intensity $I(\theta)$ can be expressed as a sum of three terms;

$$I(\theta) = I_S(\theta) + I_L(\theta) + I_C(\theta) \tag{102}$$

where $I_S(\theta)$ is the single scattering intensity, $I_L(\theta)$ is called the ladder term which is the multiple scattering intensity without interference and $I_C(\theta)$ is the crossed term which is the multiple scattering intensity with interference between direct and reverse paths [39]. The enhancement α is defined as the ratio of the intensity at $\theta = 0$, I(0) to the average background intensity $I_S(\theta) + I_L(\theta)$ at large θ and is given by,

$$\alpha = 1 + \frac{I_C(0)}{I_S(\theta) + I_L(\theta)}. \tag{103}$$

The coherent backscattering intensity for a semi-infinite slab of disordered scattering medium has a narrow cone shaped profile given by [39],

$$\frac{I(\mathbf{k_i}, \mathbf{k_f})}{I_0} \cong \frac{3(z_o + C)}{4\pi\ell} \left\{1 + \frac{1 - exp[-2|\mathbf{k_i} + \mathbf{k_f}|(z_o + C)]}{2|\mathbf{k_i} + \mathbf{k_f}|(z_o + C)}\right\}. \tag{104}$$

Here I_0 is the incident intensity and the extrapolation length C is given by

$$C = \left(\frac{2\ell}{3}\right)\left(\frac{1+\rho}{1-\rho}\right) \tag{105}$$

where ρ is the reflection coefficient at the sample surface, ℓ is the mean free path and $z_0 \cong \ell$. The full width at half maximum of the backscattered cone is given by,

$$\triangle\theta \approx \frac{0.5}{k\ell} \tag{106}$$

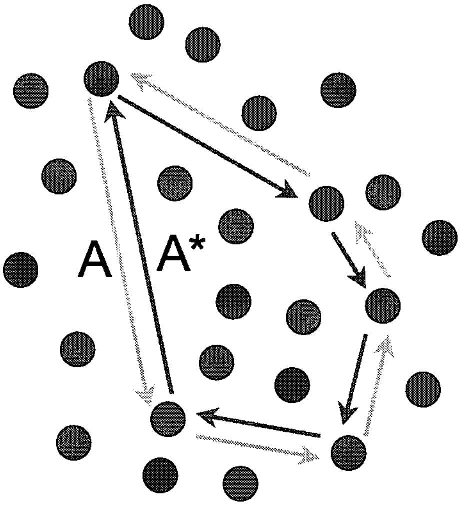

FIG. 3: Schematic illustration showing recurrent scattering of two counter propagating paths in a scattering medium.

where k is $2\pi/\lambda$ [7, 39]. Fig. 2 shows the shape of the cone for an effective medium with mean free path of $\ell = 19.5$ μm and for an incident light with wavelength $\lambda = 780$ nm.

II.7 STRONG LOCALIZATION

Coherent backscattering of light, which is a result of interference of multiply scattered waves, has been demonstrated in various systems [6,7,46,47] including ultracold gases [8, 9, 19, 21]. Another interference effect that has not been observed yet in a three dimensional atomic system is the localization of light. Localization of light is considered as a disorder induced second order phase transition or a cross-over from a diffusive system to a localized system in the transport properties of the electromagnetic wave in strongly scattering medium [48].

In the previous section we mentioned that the interference of the counter propagating paths in the sample constructively interfere in the backscattering direction. Now let us assume that these two counter propagating paths come together inside the sample and form a closed loop as shown in Fig. 3. Here we assume that the scatterers are not moving. The two counter propagating paths of the light have the same probability amplitude. Since these two reciprocal paths have zero phase difference, they constructively interfere at the starting/meeting point. Further, since these two waves are coherent, the relative probability of this event happening is determined by $P = |A + A^*|^2 = |A|^2 + |A^*|^2 + 2|AA^*| = 4|A|^2$. If the interference effects are ignored the amplitudes are added incoherently resulting $P = |A|^2 + |A^*|^2 = 2|A|^2$. As it can be seen from this example, because of the interference of the two paths, the probability to form closed loops is enhanced which in turn decreases the probability of diffusion. When the amount of the disorder reaches a critical boundary these closed loops lead to a suppression of diffusive transport. This critical boundary was parametrized by Ioffe and Regel, when the mean free path ℓ is less than the wavelength of the light λ [23]. The Ioffe-Regel boundary states that localization happens when $k\ell = 1$ but Maret *et al.* observed the onset of localization in his samples around $k\ell \sim 4$ [26,27].

This criteria is a hard one to achieve, especially for ultracold samples, as it requires densities greater than 10^{13} atoms/cm^3. Recent developments in laser cooling and trapping techniques made it possible to achieve such densities in ultracold atomic systems but there are still challenges in the observation of light localization phenomenon.

One such challenge is that, if light localization is possible and the light cannot emerge from the sample, how can one put the light in the medium? This problem potentially can be solved by using a temporal increase of $k\ell$ by implementing a quickly switchable far off resonant laser. Application of this laser beam results in a shift in energy levels of the atom that decreases the scattering cross section. This technique will be explained in detail in the experiment and results chapters.

Another challenge is: how one can know if the light is localized? What are the signatures of localization? Anderson *et al.* predicted that a conducting electronic system becomes an insulator in the localization regime [22]. The electrons normally move diffusively in a conductor as described by Ohm's Law. This results in a decrease in transmission with sample size as 1/L. When electrons are localized Anderson has predicted the transmission to be given by

$$T(L) = T_0 e^{(-L/L_{loc})} \tag{107}$$

where L_{loc} is defined as the localization length [3,49]. In the localized regime the diffusion coefficient vanishes and the transmission is suppressed exponentially, as only the tails of the probability distribution can escape from the sample [26]. So a transmission measurement can reveal if the system is localized or not. This type of measurement is not practical for the samples prepared in our experiments, because the sample size is very small, $\sim 20\ \mu m$, usually much less than the experimental spatial resolution.

Localization experiments can also be done in the time domain. The time dependent transmission or fluorescence measurements allows direct determination of the diffusion coefficient as given by Eqs. 101 and 89 in a diffusive medium. As was mentioned before, the fluorescence emerging from the sample after the light field is extinguished decays with a single exponential time constant at long times. This time constant allows measurement of the diffusion coefficient. Aegerter *et al.* used the diffusion coefficient dependence to characterize the approach to localization [28]. The transition to localization in terms of the localization exponent is given by the ansatz

$$D \propto t^{-a} \quad 0 \leq a \leq 1. \tag{108}$$

The limiting cases of a = 1,0 represents the localized and diffusive state respectively. Another way to detect localization in principle is by measuring the critical fluctuations in the scattered light intensity near the localization threshold. The speckle pattern that was discussed in the previous section is expected to show fluctuations as recurrent scattering slows the diffusion near the localization regime [50].

Finally, all dephasing effects mentioned in the previous sections, such as Doppler broadening and recoil shifts, work against localization and remain as a potential challenge in light localization experiments in ultracold atomic samples. Even though these have deleterious effects on localization in atomic samples, condensed matter systems have their own problems. Among those, absorption of the light by the medium is an important one. Absorption can show similar results to localization and it is not always trivial to differentiate one from another. Atomic samples are nearly lossless systems in this sense. Also atomic systems has advantages in terms of control and manipulation of the localization parameters while localization is happening. For example a far off resonant light can be used to shift the energy levels and the system can be switched back and forth between a localized and diffusive state. In condensed matter systems this type of control over the sample is very limited.

II.8 LASER COOLING AND TRAPPING

In 1997 Steven Chu, Claude Cohen-Tannoudji and William D. Phillips shared the Nobel prize for the development of methods to cool and trap atoms with light. Since the first demonstration of laser cooling and trapping in 1985, research with cold atom sample has become very popular in the Atomic Molecular and Optical Physics (AMO) community. Now different types of laser cooling and trapping instrumentation have become standard equipment in many AMO research lab dealing with atom-atom or atom-light interactions. The laser cooling and trapping techniques have been developed and improved continuously by the researchers around the world since its first demonstration.

In our experiments the need for a cold atom sample arises from the fact that inhomogeneous Doppler broadening in warm atoms causes frequency redistribution of the scattered light. As was discussed before, the two parameters that are important to describe light scattering from atoms are the transition frequency w_0, and the transition width Γ. Because of the Doppler shift associated with the motion of the atoms the effective light scattering cross section,

$$\sigma = \frac{(2F'+1)}{(2F+1)}\frac{\lambda^2}{2\pi}\frac{1}{(1+(2\delta/\gamma^2))} \tag{109}$$

decreases where δ is the detuning of the light from the resonant $F \rightarrow F'$ transition of the atom and λ is the wavelength of the light [51]. Since the frequency of the light is Doppler shifted by kv where v is distributed according to the Maxwell-Boltzmann law, this shift shows up as a detuning in the cross section equation, Eq. 109. This means that scattering events have different strength and introduces a random phase shift to the light field. Interference effects are the key in realization of light localization and as the phase of the scattered light randomized the interferences are expected to be averaged out. For example, the average phase shift of the light after two scattering event is on the order of

$$\Delta\phi_2 \simeq \frac{k\sqrt{\langle v^2 \rangle}}{\Gamma} \tag{110}$$

where $\langle v^2 \rangle$ is the root mean square velocity of the atoms [52]. For Rb with $\Gamma/k \sim$ 5 m/s, to see any interference effects in light scattering from atoms, the atomic sample needs to be cooled, with temperatures below one mK. For light scattering experiments involving higher order scattering, this requirement is even more severe.

In this experiment the necessary cooling and trapping of ^{87}Rb atoms is obtained by applying a combined Magneto Optical Trap (MOT) and CO_2 laser based dipole trap; the basic theory of operation will be explained in this chapter.

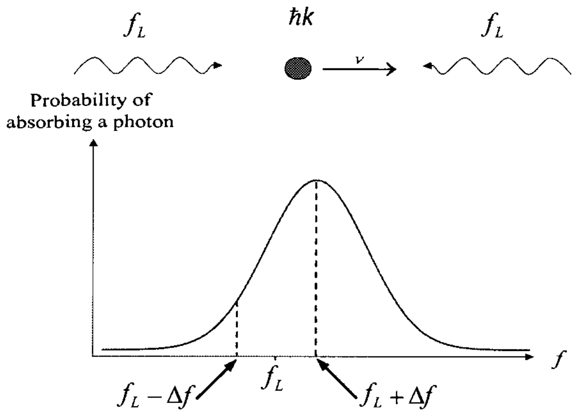

FIG. 4: Doppler broadened absorption spectrum. An atom moving towards the the laser beam is closer to resonance among the two counter propagating beams in atom's rest frame.

II.8.1 Magneto Optical Trap

In this section, general concepts of laser cooling and trapping and magneto optical traps (MOT) with details important to the experiment will be discussed. The actual MOT formation and instrumentation is explained in detail in the next chapter. The method of laser cooling is in principle simple. Since light carries momentum it can exert a force on atoms where the momentum kick that the atom experiences in scattering a single photon is on the order of $\hbar k$. The total scattering rate γ_p of light from the light field is given by

$$\gamma_p = \frac{s_0 \gamma / 2}{1 + s_0 + (2\delta/\gamma)^2} \tag{111}$$

where s_0 is the saturation parameter and is given by

$$s_0 = I/I_s = \frac{2\Omega^2}{\gamma^2}. \tag{112}$$

Here γ is the excited state decay rate and I_s is the saturation intensity which is ~ 1.7 mW/cm^2 for the ^{87}Rb cooling transition [43]. So the net force on the atoms is [53]

$$F = \hbar k \gamma_p. \tag{113}$$

For example, a Rb atom at room temperature has a velocity of $\sim$ 200 m/s. The maximum recoil velocity after each momentum kick is given by,

$$v_r = \frac{\hbar k}{m} \sim 0.6 \text{ cm/s} \tag{114}$$

where $k = 2\pi/\lambda$ and m is the mass of Rb atom. With a properly arranged laser this atom can be brought close to rest in less than a millisecond.

The Maxwell-Boltzmann velocity distribution of atoms at temperature T is given by [53]

$$f(v)d^3v = \sqrt{\frac{m}{2\pi k_B T}}\, exp\left(-\frac{mv^2}{2k_B T}\right) d^3v. \tag{115}$$

Because of the Doppler shift, the atoms moving towards the light with velocity

$$v = c\left(\frac{f}{f_L} - 1\right) \tag{116}$$

are in resonance with the incident light. On the average this causes broadening of the absorption line of the atom which is called Doppler broadening. The width of the Doppler broadened absorption line for a gas of Rb atoms at 300 K is $\sim$ 500 MHz. By adjusting the frequency of the light one can achieve velocity selective cooling of the atoms. An atom moving towards the laser beam tuned $\Delta f = f - f_L$ below the atomic resonance transition f, scatters more photons than an atom moving in the opposite direction. This way atoms moving towards the laser beam are preferentially selected and cooled as seen in Fig. 23.

If laser beams are incident on the atom from all six directions, the movement of the atoms in the intersection region can be restricted. This environment, which is called optical molasses, is a viscous sea of photons from all directions that limits the motion of atoms. It is important to note that optical molasses does not trap the atoms. It cools the atoms in the intersection region but it does not exert a position dependent force that will collect the atoms at the center or restore the atoms that have been displaced from the center.

The position dependent force comes from the operation of both the inhomogeneous magnetic fields and optical molasses. This type of trap is called a magneto optical trap (MOT) and was first demonstrated in 1987 [54]. The optical molasses provides the necessary cooling and the magnetic field gradient together with optical molasses loads atoms into the trap.

The magnetic quadrupole field as shown in Fig. 5 is generated by using two identical coils with current going in opposite directions. This arrangement of coils generates a magnetic field of zero strength at the trap center and increasing in all directions away from the center. This magnetic field gradient results in a position dependent Zeeman shift of energy levels given by

$$\Delta E_{\pm} = \pm\mu' B \tag{117}$$

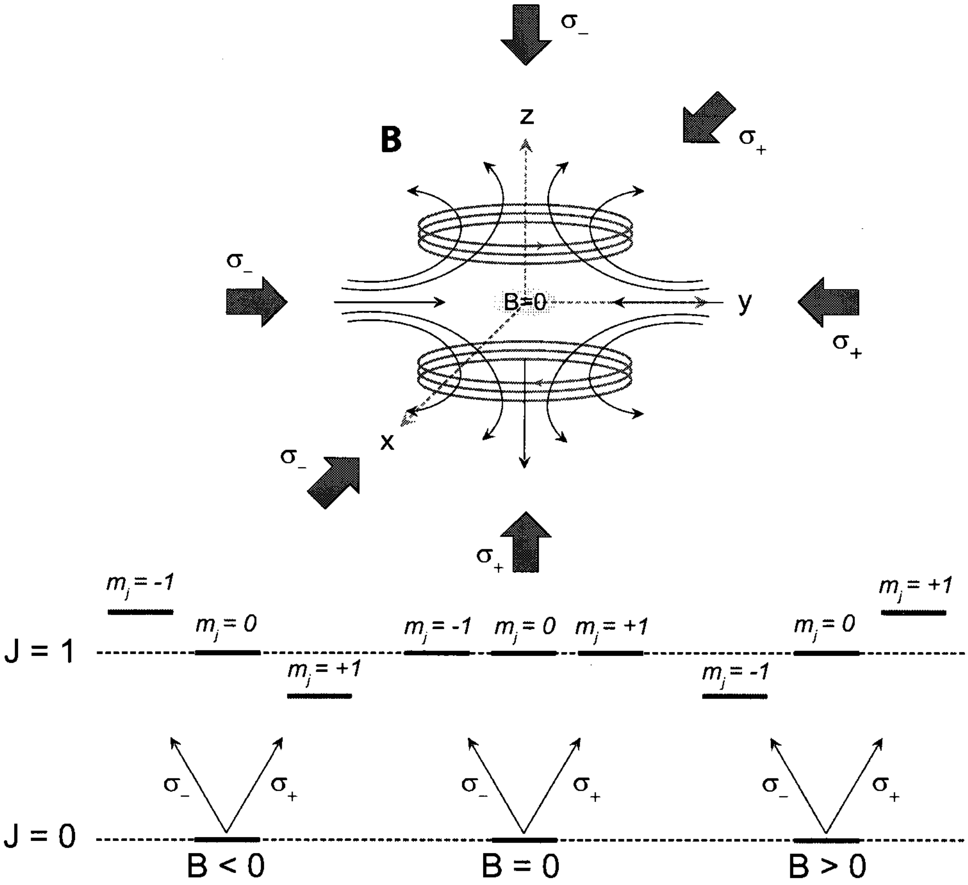

FIG. 5: A magnetic field shifts the Zeeman energy levels and together with appropriate selection of σ_- and σ_+ polarized light the atoms are cooled and trapped at the trap center, where B=0.

where $\mu' = (g_e M_e - g_g M_g)\mu_B$ is the effective magnetic moment for the $J, M_g \longrightarrow J', M_e$ transition. Here $M_{e,g}$ are the magnetic quantum numbers and $g_{e,g}$ is the Landé g-factor [53].

Fig. 5 illustrates a simplified scheme of a $J = 0 \longrightarrow J' = 1$ cooling transition of an atom in a magneto optical trap. For the atoms in the region where $B > 0$ the excited state $m' = +1$ Zeeman level is shifted up and $m' = -1$ Zeeman level is shifted down in energy. Since left circularly polarized (σ_-) light excites $m_j = 0 \rightarrow m'_j = -1$ transition and right circularly polarized (σ_+) light excites $m_j = 0 \longrightarrow m'_j = +1$ transition, in the region where $B > 0$ a σ_- polarized laser beam tuned below resonance is closer to resonance than a σ_+ polarized laser beam. As a result more σ_- photons are scattered than σ_+ photons. This is a similar situation to optical molasses, except that the force acting on the atoms in the magnetic field gradient is position dependent. In the region where $B > 0$, the atoms are being pushed towards the center of the MOT where $B = 0$. This scenario is the same for all three directions.

II.8.2 Optical Dipole Trap

In the previous section we mentioned optical light forces that slow down and cool the atoms. This same process also causes heating of the sample because of the random recoils of the atom. The competition between these heating and cooling processes results in a steady state temperature of the atomic sample. The same heating mechanism causes outward radiation pressure that limits the density of the atom cloud.

Optical dipole traps, on the other hand, rely on the dipole force which results from the interaction of the atom with the light field. The heating due to scattering of this light is kept extremely low by using a far detuned optical dipole trap.

In this section we will explore the basic concepts behind optical dipole traps by using the tools developed in the previous sections. We will first explain the nearly conservative dipole force and then we will derive the equations for the induced electric dipole interaction potential and the photon scattering rate. The section will end with the explanation of the operation of the quasi-electrostatic trap (QUEST). Details of the QUEST formation will be described in the chapters on experiment and sample characteristics.

An atom in an electric field **E** has an induced dipole moment that is given by

$$\mathbf{p} = \alpha(w)\mathbf{E} \tag{118}$$

where α is the complex polarizability of the atom, which depends on the driving frequency w. The polarizability of an atom is a measure how well a dipole can be induced in the presence of an electric field. This induced dipole then interacts with the applied field and the interaction potential of the induced dipole moment is given by

$$U = -\frac{1}{2}\langle \mathbf{p} \cdot \mathbf{E} \rangle \tag{119}$$

where the angular brackets denote the time average of the product. The 1/2 in front of the equation indicates that the dipole is induced, not a permanent one. This treatment assumes that the field has a linear response to the electric field as $\alpha\mathbf{E}$.

The resulting dipole force is given by the gradient of the potential U,

$$\mathbf{F}(\mathbf{r}) = -\nabla U(\mathbf{r}). \tag{120}$$

From Eqs. 118 and 119 the potential in terms of the Poynting vector I is

$$U = -\frac{Re(\alpha)}{2\epsilon_0 c} I(r, z) \tag{121}$$

from which the dipole force can be written as

$$F = \frac{Re(\alpha)}{2\epsilon_0 c} \nabla I(r, z). \tag{122}$$

From Eq. 122 we see that the potential is attractive or repulsive depending on the sign of the polarizability α. Atoms with positive polarizability are forced towards the higher intensity regions and the atoms with negative polarizability are repelled.

The intensity of a focused Gaussian laser beam in cylindrical coordinates is given by

$$I(r, z, \phi) = I_0 \frac{1}{1 + (z/z_R)^2} \exp(-2r^2/\varpi_0^2) \tag{123}$$

where ϖ_0 is the $1/e^2$ beam waist at the focus and z_R is called the Rayleigh range with $z_R = \pi\varpi_0^2/\lambda$. Here λ wavelength of the laser. This type of trap provides three dimensional confinement in the form of an elliptically shaped cloud of atoms.

The polarizability of the atom can be found from the equations derived in section II.4 for the susceptibility of the atom. From Eqs. 67, 73 and 118 we can relate the complex polarizability to the total polarization as,

$$\begin{aligned} P &= \epsilon_0 \chi(w) \mathbf{E} \\ &= Np(t) = N\langle \psi | - e\hat{\epsilon} \cdot \mathbf{r} | \psi \rangle \\ &= N\alpha(w)\mathbf{E} \end{aligned} \tag{124}$$

Then $\alpha(w)$ becomes

$$\alpha(w) = \frac{\epsilon_0 \chi(w)}{N}. \tag{125}$$

A comparison of Eq. 125 and Eq. 80 yields

$$\alpha(w) = \frac{e^2}{\hbar} |\langle 1|\hat{\epsilon} \cdot r|0\rangle|^2 \frac{1}{w_{10} - w - i\gamma/2}. \tag{126}$$

From Eq. 126 the real part of polarizability $Re(\alpha)$ is

$$Re(\alpha) = \frac{e^2}{\hbar} |\langle 1|\hat{\epsilon} \cdot r|0\rangle|^2 \frac{w_{10} - w}{(w_{10} - w)^2 + (\gamma/2)^2} \tag{127}$$

and the imaginary part of the polarizability $Im(\alpha)$ is

$$Im(\alpha) = \frac{e^2}{\hbar} |\langle 1|\hat{\epsilon} \cdot r|0\rangle|^2 \frac{\gamma/2}{(w_{10} - w)^2 + (\gamma/2)^2}. \tag{128}$$

where we removed the average over random directions as the induced dipole is in phase with the field. From Eqs. 127 and 121 we can write the dipole potential as

$$U = -\frac{1}{4}\frac{e^2}{\hbar} |\langle 1|\hat{\epsilon} \cdot r|0\rangle|^2 \frac{w_{10} - w}{(w_{10} - w)^2 + (\gamma/2)^2}. \tag{129}$$

Substituting the Rabi frequency in Eq. 129 we get

$$U = -\frac{\hbar\Omega^2}{4} \frac{w_{10} - w}{(w_{10} - w)^2 + (\gamma/2)^2}. \tag{130}$$

where

$$\Omega = \frac{eE_0}{\hbar} |\langle 1|\hat{\epsilon} \cdot r|0\rangle|. \tag{131}$$

It is convenient to introduce the detuning δ:

$$\delta = w_{10} - w \tag{132}$$

For large enough detuning, and ignoring the radiative decay, the potential derived here agrees with Eq. 38;

$$U = -\frac{\hbar\Omega^2}{4\delta}. \tag{133}$$

It is also important to derive the scattering rate due to the applied field. A high scattering rate in dipole traps heats the atoms and decreases the lifetime of the trap. The scattering rate is given by,

$$\Gamma_{sc} = \frac{1}{2\hbar} Im(\alpha) E_0^2. \tag{134}$$

Substituting $Im(\alpha)$ from Eq. 128 into Eq. 134 yields

$$\Gamma_{sc} = \frac{e^2 E_0^2}{4\hbar^2} |\langle 1|\hat{\epsilon} \cdot r|0\rangle|^2 \frac{\gamma}{(w_{10} - w)^2 + (\gamma/2)^2}. \tag{135}$$

Simplifying with substituting δ and Ω into Eq. 135 brings the scattering rate Γ_{sc} to a form of

$$\Gamma_{sc} = \frac{\Omega^2}{4} \frac{\gamma}{\delta^2 + (\gamma/2)^2}. \tag{136}$$

From the Eqs. 136 and 133 we can write the scattering rate in terms of the potential as

$$\Gamma_{sc} = -\frac{\gamma}{\hbar\delta} U. \tag{137}$$

From comparison of the equations of the scattering rate and the dipole potential we can immediately see the advantage of the dipole traps. The scattering rate is proportional to $1/\delta^2$ and the potential is proportional to $1/\delta$ which allows us to decrease the scattering rate without reducing the well depth. The high powered CO_2 lasers with 10.6 μm wavelength offers extremely low scattering rates and good potential well depths. But if the detuning is too big, as in the case of the CO_2 laser, the rotating wave approximation that is applied up to this point does not hold. This case is explained in the next section.

II.8.3 Quasi-Electrostatic Traps

As it was mentioned earlier when the frequency of the light field is much smaller then the resonance frequency of the first excited state of the atom the light field can be considered as a quasi static electric field and the rotating wave approximation can not be made. The traps employed by using such light field are called quasi electrostatic trap (QUEST). The neglected counter rotating terms should also be included in the derivations. Then the susceptibility including the counter rotating term can be written from Eq. 80 as

$$\chi(w) = \frac{Ne^2}{\epsilon_0 \hbar} |\langle 1|\hat{\epsilon} \cdot r|0\rangle|^2 \left(\frac{1}{w_{10} - w - i\gamma/2} + \frac{1}{w_{10} + w + i\gamma/2} \right). \tag{138}$$

From Eq. 138 the real part of the polarizability $Re(\alpha)$ is

$$Re(\alpha) = \frac{e^2}{\hbar} |\langle 1|\hat{\epsilon} \cdot r|0\rangle|^2 \left(\frac{w_{10} - w}{(w_{10} - w)^2 + (\gamma/2)^2} + \frac{w_{10} + w}{(w_{10} + w)^2 + (\gamma/2)^2} \right) \tag{139}$$

and the imaginary part of the susceptibility $Im(\alpha)$ is

$$Im(\alpha) = \frac{e^2}{\hbar}|\langle 1|\hat{\epsilon}\cdot r|0\rangle|^2 \left(\frac{\gamma/2}{(w_{10}-w)^2+(\gamma/2)^2} + \frac{\gamma/2}{(w_{10}+w)^2+(\gamma/2)^2}\right). \tag{140}$$

In the quasi electrostatic limit we can take $w \rightarrow 0$ and $w_{10} \gg \gamma$. Then the real part of the polarizability $Re(\alpha)$ is given by

$$Re(\alpha) = \frac{e^2}{\hbar}|\langle 1|\hat{\epsilon}\cdot r|0\rangle|^2 \left(\frac{2}{w_{10}}\right) \tag{141}$$

and the imaginary part of the polarizability $Im(\alpha)$ is

$$Im(\alpha) = \frac{e^2}{\hbar}|\langle 1|\hat{\epsilon}\cdot r|0\rangle|^2 \left(\frac{\gamma}{w_{10}^2}\right). \tag{142}$$

The polarizability in Eq. 121 is the static dc polarizability of the atom in the electrostatic approximation. Then the dipole potential of the QUEST U is

$$U \sim -\frac{\hbar\Omega^2}{2w_{10}}. \tag{143}$$

The relation between the scattering rate Γ_{sc} and the potential U is given by [55]

$$\Gamma_{sc} = 2\left(\frac{w}{w_{10}}\right)^3 \frac{\gamma}{w_{10}}U. \tag{144}$$

When this equation is compared with the scattering rate equation of far off resonance traps (FORT) in Eq. 137 QUEST scattering rate is less by a factor of $2(w/w_{10})^3\delta/w_{10}$.

CHAPTER III

EXPERIMENTAL INSTRUMENTATION

III.1 INTRODUCTION

A main ingredient of this dissertation project was the design and construction of the experimental instrumentation. At the initiation of the project to study Anderson localization of light in an ultracold atomic gas, there was no experimental apparatus or supporting instrumentation to achieve that goal. The aim of this chapter is to describe in some detail the experimental apparatus that was constructed, and its basic operation. Further, more technical details, are presented in an appendix. In addition, the procedures by which the ultracold sample of ^{87}Rb is formed in a magneto optical trap, and subsequently compressed into a high density optical dipole atom trap, are described.

The global setup of the instrumentation is shown in Fig. 6. The various experimental zones, as schematically shown there, consist of the vacuum system and sample chamber, the various diode lasers and the carbon dioxide laser used, and optical arrangement used to route the and control the various laser beams used in the various experiments performed. In the following sections, each of these zones, and their subsequent operation is described in detail.

III.2 VACUUM CHAMBER

The ultrahigh vacuum chamber shown in Fig. 7 consists of 12 viewports, 8 of which are 2-3/4" Del-Seal conflat (CF) flanges with antireflection (AR) coating at 780nm. Six of these quartz windows are used for MOT beams and 2 of them are used for probing and imaging purposes. (MDC part number:450002) The 2 off axis quartz viewports that are positioned between detection and MOT windows are 2-1/8" size and these are not AR coated to allow detection of fluorescent different than 780 nm. These two windows are used for probing and to implement a light shift laser for the experiments that are explained in this thesis. The two 4-1/2" windows are made of ZnSe and they are AR coated at 10.6 μm. These two windows are purchased from Insulator Seal (ISI), Florida(Part Number 9792903). These windows are used for the entrance and exit of the CO_2 laser beams. ZnSe windows allow transmission of some

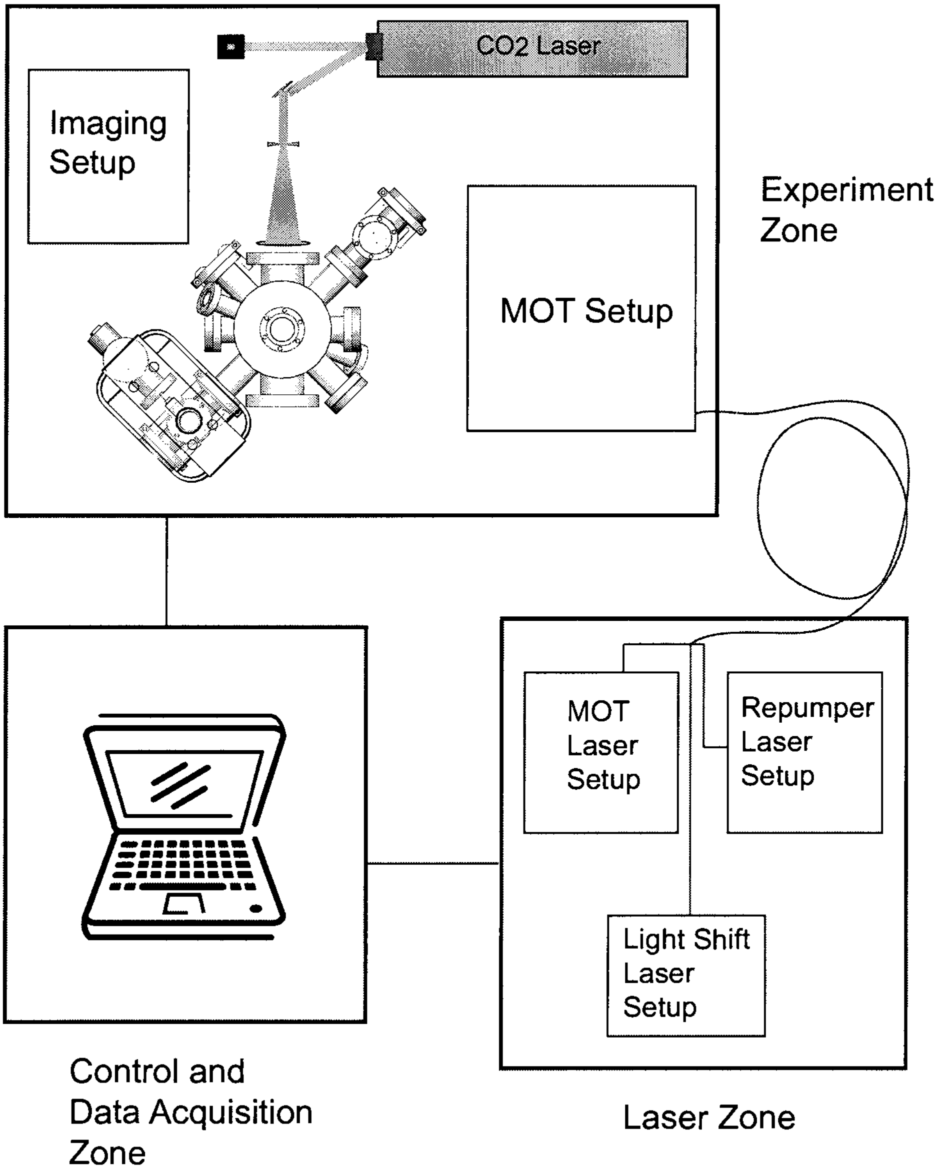

FIG. 6: Schematic diagram of various experimental zones explained in this chapter.

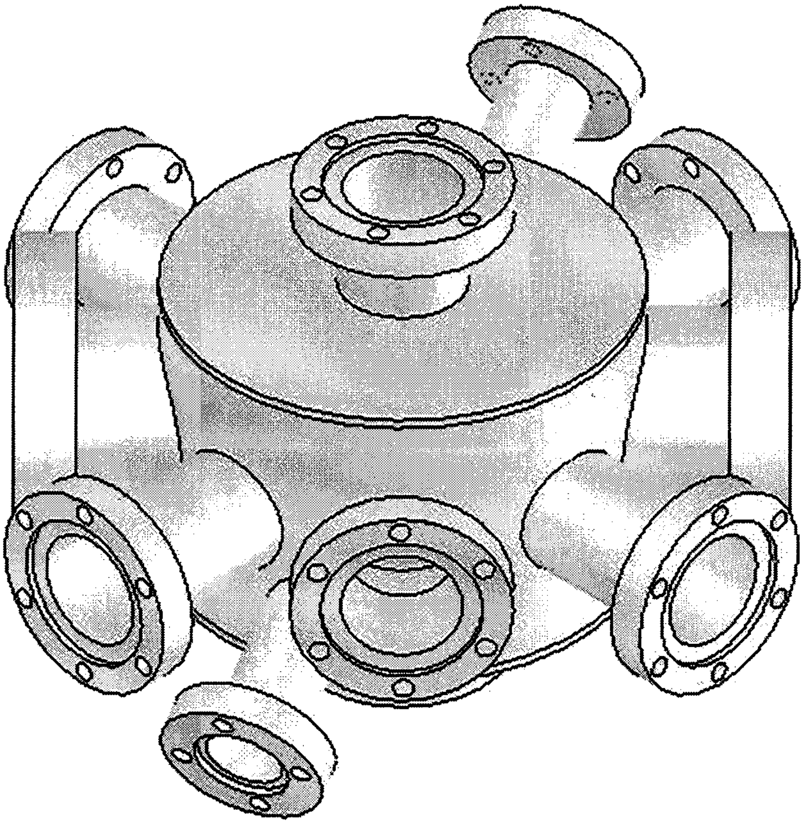

FIG. 7: The vacuum chamber consists of 12 viewports; 8 of 2-3/4" diameter AR coated for 780nm, 2 of 2-1/8" diameter and 2 of 4-1/2" diameter ZnSe windows. Detailed CAD drawings of this chamber can be found in Appendix A

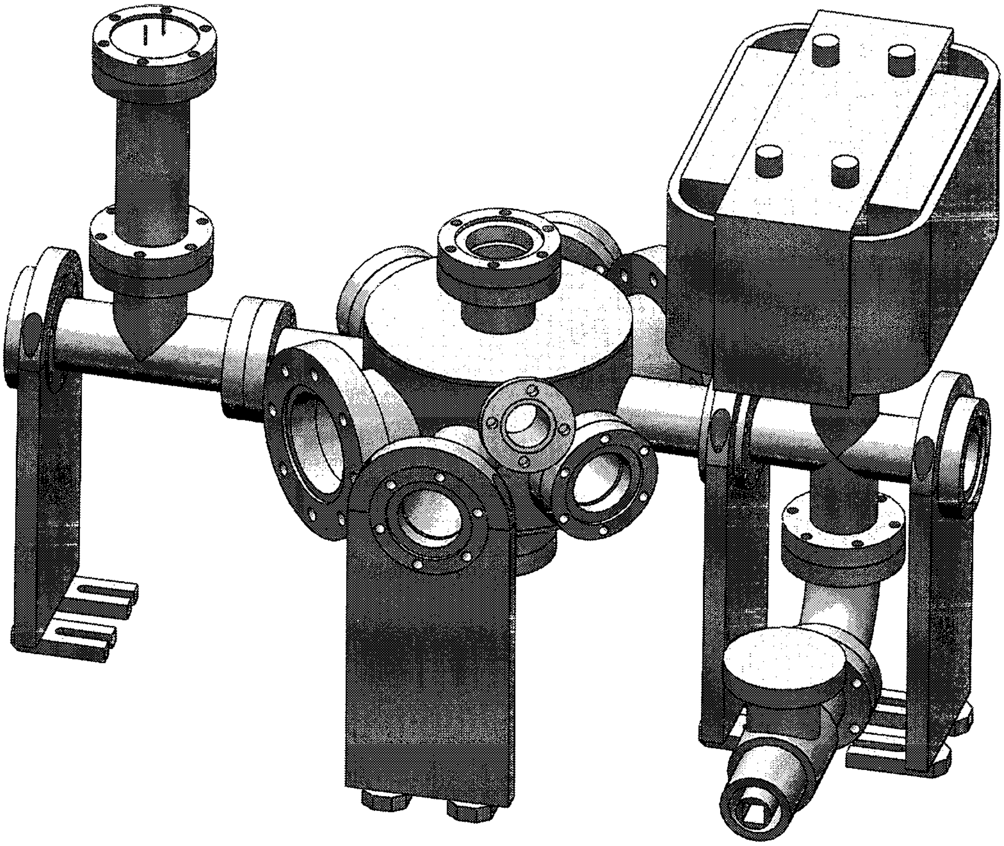

FIG. 8: The complete vacuum assembly consists of the main chamber, a 20 liter/s ion pump, SAES getters attached to an electrical feedthrough and valve.

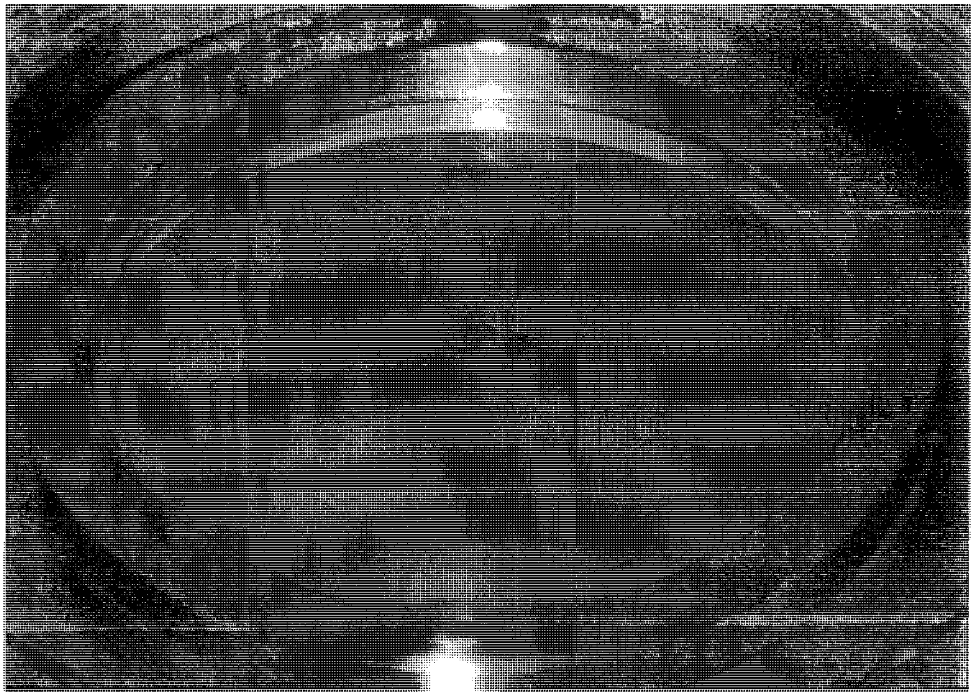

FIG. 9: Contamination of ZnSe window

visible light enabling easier alignment of the CO_2 laser by using 780 nm light or a HeNe laser. Because of its low absorptivity at infrared wavelengths ZnSE is used in high power CO_2 laser applications. I would like to mention one strange problem about these windows that we experienced. A few other groups have documented the same problem [56]. After 3 years of continuous operation of the apparatus we recognized a dramatic drop 75% in laser power transmission through these ZnSe windows. After closely examining these two windows we saw a speckled layer on the vacuum side of these windows, see Fig. 9. We initially thought this would be Rb build up in time inside the chamber and decided to bake the windows to remove the layer. Baking the windows up to 150 degrees resulted in no improvement. During a vacuum break we tried to clean these windows and we were partially successful in that. We were able to restore the transmission of the CO_2 laser to 75% after both windows. We put the less dirty window on the CO_2 entrance side of the chamber. We still don't know the source of the contamination but it could be a reaction between the coating and Rb vapor.

The vacuum chamber has $\sim 10^{-9}$ Torr pressure after three months of baking the chamber at 473 K. The change in the vacuum pressure vs current during the

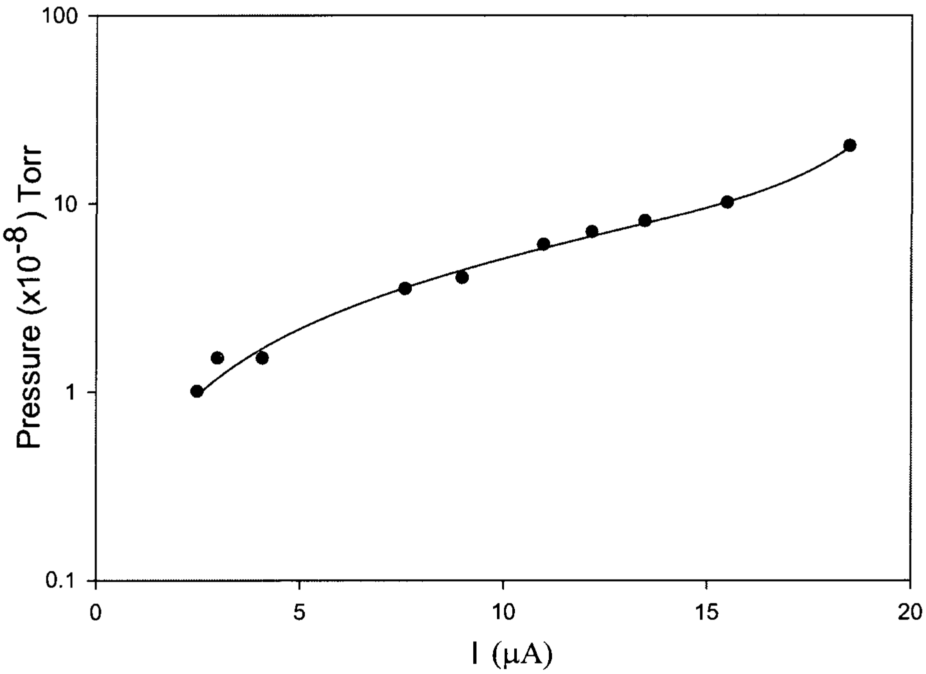

FIG. 10: Pressure vs current curve during the vacuum formation.

whole process is shown in Fig. 10. The sensitivity of the pressure gauge of the ion pump goes to a minimum of 10^{-8} Torr but lower pressures can be measured from the current scale of the same gauge. The minimum current read on the gauge is 0.4 μA which is estimated to be $\sim 9{\cdot}10^{-10}$ torr. The stainless steel chamber came cleaned, leak tested and ready for ultrahigh vacuum (UHV) installation from MDC. All components of the chamber were washed in a high temperature detergent bath followed by multiple tap and deionized water rinses by MDC. After the last rinse, parts were also blown dry with dry nitrogen and packaged and sent to us.

The total vacuum assembly is shown in Fig. 8. The pressure in the chamber is achieved and maintained by a 20 liter/s Varian ion pump. The ion pump has large magnets attached to it which causes a stray B-Field gradient accross the chamber. To overcome this we initially covered the ion pump with Mu-metal. This had little effect. The measured magnetic field at the center of the trap is less than 0.3 G which can be compensated easily with shim magnetic field coils distributed around the chamber. These coils also balance the field not only from the ion pump but also from magnetic materials around the chamber and the Earth's field. An ideal configuration would be 6 coils with 2 coils paired in Helmholtz configuration each direction but because of geometrical reasons we used 3 coils with 1 for each direction. Two additional anti-Helmholtz coils are also installed in the z (vertical) dimension to provide the necessary magnetic field for the magneto optical trap. This magnetic field can be completely shut off electronically within 1 ms but induced magnetic fields are present that arise from induced currents in the MOT quadrupole coils, the MOT shim magnetic field coils, and eddy currents in the MOT chamber and other conducting or magnetizable materials in the vicinity of the apparatus.

One component seen in the Fig. 8 sticking out on the left side of the main chamber is the electrical feed-through (Kurt J. Lescer CO; part number EFT0044033) that provides current to the SAES Rb getter-dispensers (Part number:Rb/NF/3.4/12 FT 10+10) welded to its pins. Acording to the specifications of these getters the Rb should start evaporating around 5 A but running at 3.4 A for our setup was sufficient to produce enough flow of Rb in the chamber. We only ran the getters at 5 A during the initial loading of the MOT. Then we had to run these getters continuously for a few days to achieve enough coating inside the walls of the chamber. Another factor in the low current that we use is the MOT quadrupole coils running at 12 A. This leads to heating the chamber walls and releasing the Rb into the chamber. Later we switched to a technique called LIAD (Light induced atomic desorption) and we only used the getters once a week or so to coat the walls of the chamber again with Rb. The windows of the chamber are 780 nm coated and have very little transmission at 400 nm, the wavelength at which this method is most effective [57]. For that reason we used 14 high power Ultra violet (UV) light emitting diodes (LED) each of which dissipate about 200 mW. Very little of this power is reaching inside the chamber because of the geometry and coated windows. The LEDs are bought from *www.superbrightleds.com* (Part number; XR7090UVV XLamp 1 Watt LED). All of these LEDs are distributed around the chamber and directed towards the inside of the chamber from the side of the window. Three or four LEDs are placed on each window. Lens kits that fit on these LEDs are also used to collimate the beam a little so that most of the light can enter the chamber. One other important thing is heat dissipation on these LEDs. Initially they were mounted without heat sinks but this caused problems like power output loss of the LEDs as they get heated. Later small heat sinks were installed behind the individual LEDs or were mounted them on a big heat sink and with a hole in the middle to let the MOT beams go through. If the chamber had a UV coated window that looks inside the chamber one of these LEDs would have been sufficient for the experiment.

Components of the chamber were put together by using silver plated screws with plate nuts and copper gaskets. Lint free gloves were worn during the whole process. Leak test grooves were aligned and all the bolts were hand tightened initially. The complete tightening process was done gradually in 1/4 to 1/2 turn increments in an alternating crisscross pattern in order to form an even gasket compression and deformation.

III.3 LASERS

III.3.1 Diode Lasers

Diode lasers have became popular within the scientific community during the last 20 years because of their low cost and ease of use. Especially diode lasers with wavelengths close to those of diodes used in the CD/DVD players offers great advantage with this respect. For example, this encouraged many physicists working on ultracold atoms to use Rb atoms which has a cooling transition at 780 nm. For example one can buy a 120 mW 780 nm diode for about $20. Other advantages of diode lasers include having a narrow linewidth in an external cavity and being tunable within a wide range easily via optical feedback, temperature and diode injection current. It is also important to note that these diodes can stay stable and locked to a specific wavelength for a long time by using proper locking mechanisms.

Diode lasers are one of the two main optical light sources that are used in this experiment. External cavity diode lasers (ECDL) that are designed in Littrow or Littman-Metcalf configurations are used to produce necessary beams for formation of the magneto optical trap, probing samples and as a light shift laser that will be explained in subsequent sections. Fig. 11 and Fig. 12 shows two common configurations of ECDLs. The Littrow design offers wider tuning capability without a mode hop and higher optical output than the Littman-Metcalf design. On the other hand in the Littrow design without additional optics, the beam moves during the alignment. The Littman-Metcalf design was used primarily in our labs until this problem was solved by adding an additional mirror attached to the same mount that holds the grating. This way the grating and the mirror turn in opposite directions and as a result the beam only moves laterally which usually is not a problem in our

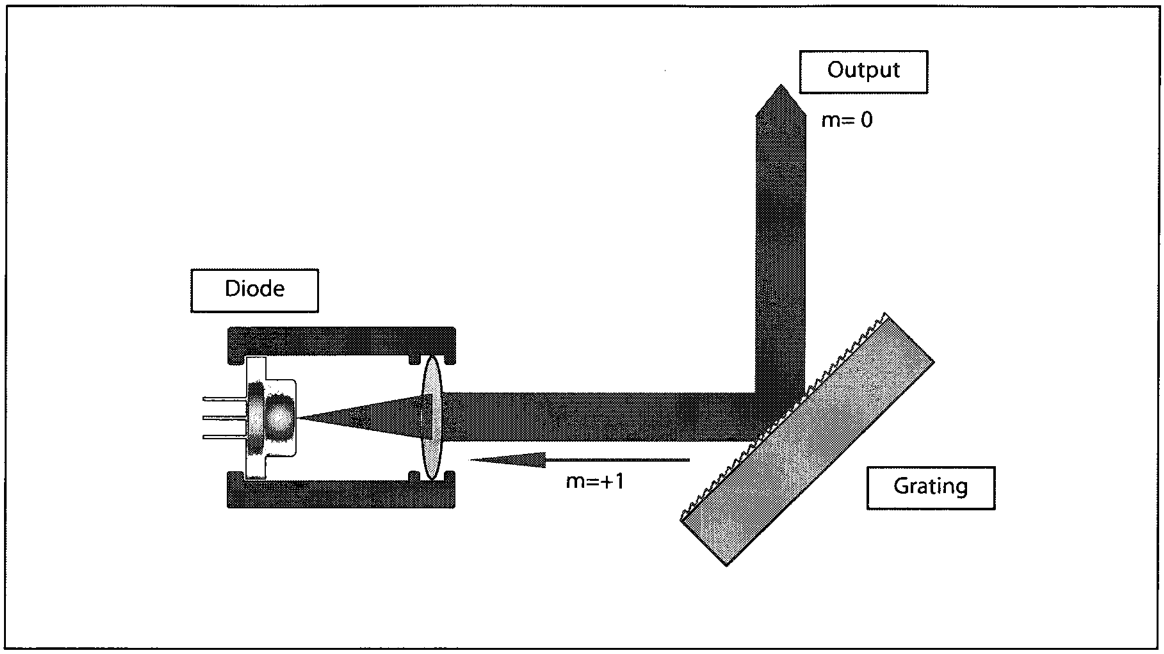

FIG. 11: Littrow Configuration

experiments.

The ECDL design that is now primarily used in our experiments is in Littrow configuration. A schematic of the design is shown in Fig. 13. The laser diode is 120 mW maximum power single mode SHARP GH0781JA2C that was purchased from Digikey for $20. This diode is put into a collimation tube (Model LT230P-B) with a 4.51 mm focal length aspheric lens (C230TME-B) that was purchased from Thorlabs. The collimation tube assembly is put into a custom made mount that we call a collimation tube holder that is attached with two screws that are premounted on the ultra-stable kinematic mirror mount (Thorlabs; model KS1D) to lock the actuators. This mirror mount is also further modified to be able to attach a grating holder and a correcting mirror holder as shown in Fig. 13. This mirror mount and the grating holder is attached to the front plate of the Thorlabs mirror mount that is milled and sanded for proper installation. In Littrow configuration the grating is adjusted such that the first order reflected beam (m = 1) is injected into the diode for tuning the laser frequency. In Littrow configuration the angle of incidence is equal to the angle of refraction which reduces the grating equation to this form:

$$m\lambda = 2dsin\theta \tag{145}$$

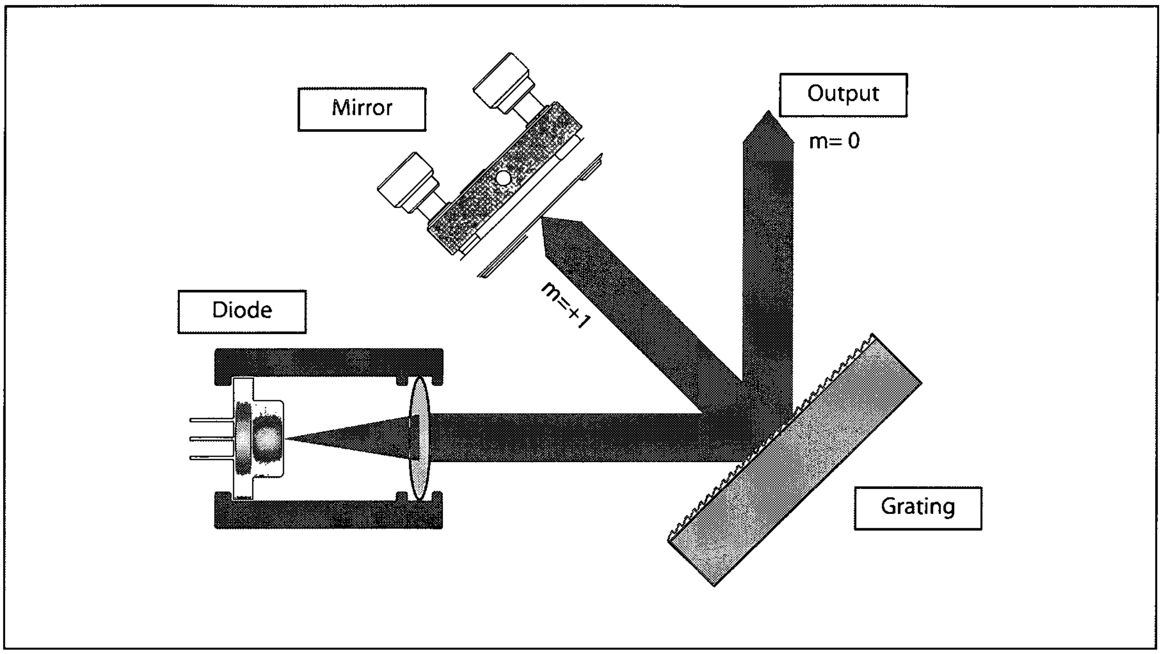

FIG. 12: Littman-Metcalf Configuration

where λ is the wavelength of the incident light, θ is the angle of incidence, m is the diffraction order and d the spacing between adjacent grooves on the grating surface. For geometrical reasons in our design θ should be around 45 degrees. A grating purchased from Optometrics (part number:3-4182) with d = 1800 grooves/mm well fits for this job. The zeroth order is the output beam which reflects from another mirror (Thorlabs; BB05-E03) that corrects the direction of the beam as the actuator controlling the front face is adjusted during the alignment. This assembly is then mounted on to a small plate which sits on top of a larger base plate that holds the laser assembly. A thermoelectric cooler (TEC) module is installed between these two plates to temperature stabilize the plate and the laser diode. (Marlow Industries; DT12-6-01L) A 10 kΩ thermistor is put onto the small plate as a temperature sensor. The temperature is controlled and stabilized with a home built temperature controller to about 0.002 ^{0}C in this setup. This assembly is also mounted on a 1 inch thick heavy base to provide better thermal and vibrational stability to the laser. The laser is then put into an aluminum casing with 3 small holes in the back for tuning and one in the front to allow beam to exit. The inside walls of this cover is covered with Nexus DampTek Noise Absorption Material that is usually used in PCs to absorb noise and to have a quiet computer. This material is sold by www.endpcnoise.com.

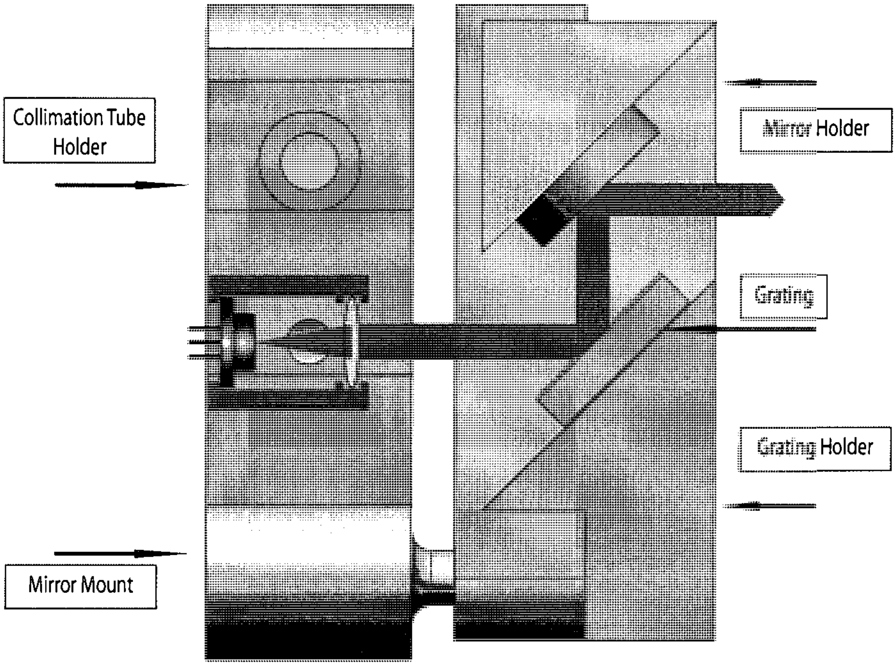

FIG. 13: Final laser design used in this dissertation research.

The frequency tuning of the laser is done by a home built current controller, a home built temperature controller and with the horizontal actuator of the mirror mount. The temperature of the diode is kept around 15 ^{0}C below room temperature and above the dew point to minimize condensation. The current of the diode is always kept below 1.15 Amps to avoid having too much feedback into the diode and to keep the diode in single mode running condition for a long period of time. When the current is set at 1.15 Amps, the laser has a usable output of about 45 mW. To fine tune the laser and also to be able to lock to a reference point generated by a saturated absorption and a lock-in amplifier a piezo-electric actuator (Thorlabs;AE0203D04) is installed between the tip of the horizontal actuator and the front faceplate of the mirror mount.

The alignment of the laser is done by using the horizontal and vertical actuators of the mirror mount. During the alignment process the grating holder is first removed and the laser output is collimated by focusing the beam at far field. After carefully collimating the beam, the grating holder is replaced and a small card is placed in the front of the aspheric lens blocking half of the beam. By using the horizontal and

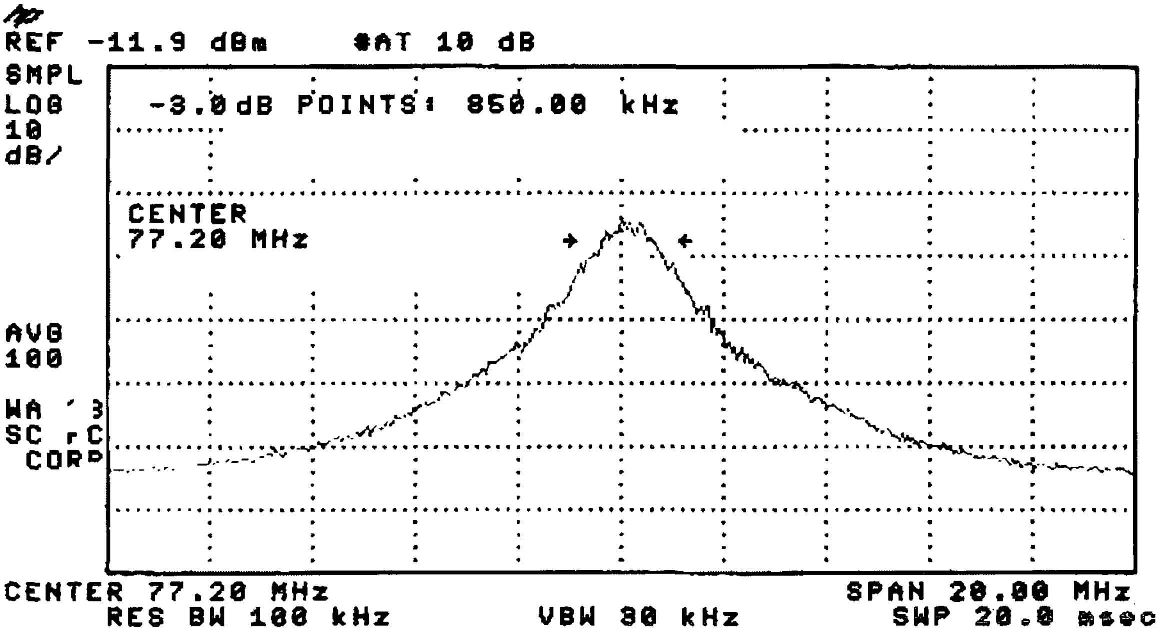

FIG. 14: Laser linewidth measurement is done by using two Littrow design ECDL. The figure shows combined FWHM linewidth of these two lasers to be 850 kHz.

vertical actuators the movement of the first order beam on the card is observed and brought closer to the output as much as possible horizontally and vertically. Then the small card is removed and another card is put in the output of the laser and the current of the laser is adjusted to a value a little less than the free running lasing threshold current which is around 30 mA. While adjusting the vertical actuator a flash of the laser output should be observed when the first order beam is perfectly injected back into the diode. Further fine tuning is done by decreasing current below threshold again and aligning the vertical. Once satisfactory vertical alignment is attained, it is not touched during the rest of the process. The output of the beam is coupled into a Burleigh wavemeter for bringing the laser to the vicinity of the desired spectral range. Only the horizantal actuator is moved or current and temperature values are changed at this point. A Rb cell is also installed in the beam path and fluorescence of the beam is observed as the laser is tuned around resonances. Vertical alignment is also checked again at this point in order to make sure the vertical alignment did not change during horizontal alignment because of small imperfections in the grating holder and the front plate.

The diode lasers as described here are a modified version of the Sussex/Melbourne

Design [58–60]. The lasers built in our lab are usually very stable and they can stay locked for days. Since these are short cavity lasers we had doubts about the linewidth of the lasers. By using two of the same type of lasers in an optical heterodyne setup we measured full width at half maximum (FWHM) linewidth of each laser to be about 600 kHz as shown in Fig 14. The figure shows the combined linewidth of two lasers.

III.3.2 CO_2 Laser

As it was mentioned before the main goal for building a CO_2 based dipole trap is to achieve high density atomic sample. At the time when this experiment was proposed CO_2 dipole traps were promising and successful in achieving such densities. [61, 62] Even though heating due to optical scattering is minimal in far-off resonant traps heating due to position or intensity fluctuations can be a major source for heating and subsequent loss of atoms from the trap [63, 64]. This will be explained in more detail in the parametric heating measurement section of this thesis. In a parametric resonance experiment, a known frequency and amplitude of intensity modulation is added to the laser. Power stability is the main issue with these lasers and when this research started Coherent had developed ultra-stable CO_2 lasers. We did not measure the power stability of our laser because the power meter used in this experiment doesn't have fast enough response to measure these fluctuations but from our loading efficiency and trap lifetime measurements we inferred that the intensity noise of our laser should be within the specifications.

The wavelength of the CO_2 laser is 10.6 μW which is far off resonance for ^{87}Rb and offers very low scattering rates. It is also important to note that trap depth decreases with the detuning but CO_2 lasers offer high power outputs that allows us to have deep enough traps. We bought Coherent-Deos GEM Select 100 with rf power supply. We asked Coherent to remove the DC power supply that they sell with this machine to run the rf power supply. Instead we use Agilent 6573A 35V 60A DC power supply because of their very low 40mA ripple noise to minimize the noise associated with the rf power supply. The laser optical output is about 100 W. The laser requires cooling as it generates about 2 kW of heat. The laser was cooled initially by a Neslab HX 150 chiller with 25% Dowfrost additive in the water but later we switched to a building-level chiller that the university provides when we realized the Neslab chiller could not provide enough cooling for the laser. Dowfrost is a product that is sold by

DOW Chemical Company. It is a low-toxicity inhibited propylene glycol-based heat transfer fluid. The temperature of the fluid is kept around 18 ^{0}C. We did not cool it further because of the condensation problems.

Alignment of the CO_2 laser is a very difficult and also a dangerous task as the beam cannot be seen without special equipment and 100 W is powerful enough to cause skin damage if accidentally touched. It is also very easy to ignite clothing during the alignment process. Extreme care should be taken for the eye protection as scattered beam off the surfaces during alignment could cause serious eye damage. For this purpose we used CO_2 laser safety goggles whenever the laser switched on. Another factor that makes the alignment harder is there is no way of knowing if the alignment is good without actually loading atoms into the trap. But trap loading depends on other factors that will be explained in the upcoming sections. For this reason initial alignment took us about a month. Fig. 15 depicts the general optical layout of the CO_2 laser beam.

The shutter that came with the laser does not switch on and off fast enough and the output power of the CO_2 laser is not controllable. For this purposes an acousto optical modulator (AOM) is placed right after the CO_2 laser. The AOM allows us to shut off the CO_2 laser in 1 μs and modulate the beam to do parametric resonance measurements and also control the beam intensity to be able to do evaporative cooling and other experiments. The AOM diffracts the beam into many orders and by adjusting the angle of incidence it is possible to maximize the output on any order. In this experimental setup 1st order is used with a $\sim$ 60% efficiency. Zeroth order is the non diffracted beam and it is dumped into the beam dump. The AOM (Intraaction Corp; AGM-406BIM) used in this setup is a special AOM that is built for CO_2 laser application. The rf amplifier and driver of this AOM is also from Intraaction. (GE-4030) This driver runs at 40 MHz at 30W max power. The power is controlled by a 0-1V 50Ω input terminated analog channel. The AOM is water cooled to remove the heat from the crystal that is generated by the rf and by the absorption of $\sim$ 10% of the CO_2 laser beam. The cooling water is supplied by the same chiller that cools the CO_2 laser. This AOM is mounted on a rotating mount that allows us to fine tune the angular alignment and maximize the diffraction efficiency. The alignment is done by placing a power meter in front of the first order diffracted beam and dumping the zeroth order. After the installation of the AOM and the beam dump, during the alignment the rf power of the AOM is decreased to a minimum level. Once the

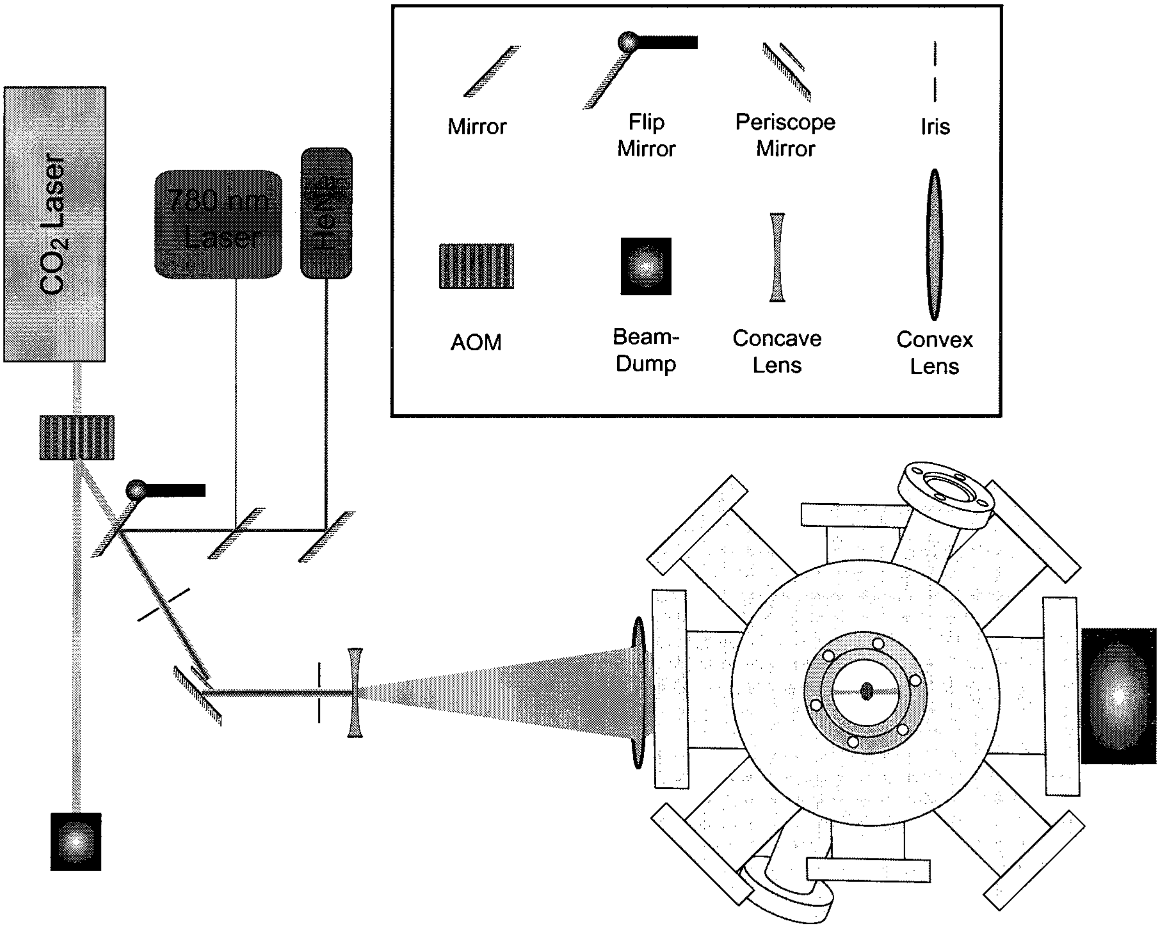

FIG. 15: CO_2 optical setup: The figure shows the major elements that are used during the CO_2 alignment. 780 nm laser is tuned on resonance and overlapped with the MOT. Then CO_2 is overlapped with the 780 nm laser. Once the alignment is finished a flip mirror and 780 nm laser are removed. A beam dump is placed near the back window.

alignment is finished it is checked at full power and the alignment is corrected for possible movement of the beam. At full power the crystal of the AOM is warmer and the lenses absorb some of the beam and warm up which causes changes in the transmission properties of these optics. This leads to shift in the beams direction and a change in the focus spot location. This puts a limit on the hold time of the trap and prevents to make accurate hold time measurements. For this experiment the CO_2 laser was on for 1.2 seconds out of a 4.5 seconds duty cycle which is not too long to cause significant heating.

Our laser has a mechanical shutter that allows us to temporarily block the beam without turning off the laser. Later we realized that cooling for the beam dump inside the laser that the beam is directed when the shutter is activated is not sufficient. The coolant fittings gets hot and causes leak if the shutter is used for long period of time. We avoided using this shutter after we had a leak inside the laser. But before the leak the alignment was done by using this shutter and by turning the shutter off for an instant and letting the beam out for short period of time. During the alignment we used the burnmarks on wood and paper formed after these snapshots of the laser. Because of the difficulty of this process and having smoke near near the optics is not desirable and also to assist in the whole alignment process a HeNe laser is overlapped with the CO_2 laser. A flip mirror is installed into the system to allow the alignment of the optics to be done by using this beam.

The optics used for the CO_2 laser is acquired from II-V, an infrared optics company. The mirrors are made of copper and the lenses are made of ZnSe. They are coated at 10.6 μm for maximum reflectivity or transmission. The Gaussian beam that emerges from the laser has 3.8mm $1/e^2$ diameter. After it passes through the AOM first order, the beam is elevated to the chamber center height by using a periscope assembly formed by using two copper mirrors. The beam is focused to the trap center by using two ZnSe lenses. The configuration is shown in Fig. 15 and Fig. 16. The combination has an effective focal length of $\sim$ 5.5". The lens combination is designed for an incident 6 mm beam to be focused to a diffraction limited spot size of 71 μm diameter. The experimental spot size is 110 μm. Part of this difference can be attributed to thermal lensing effect due to the heating of the AOMs crystal. The spot size, $2\omega_0$, of a Gaussian beam with wavelength, λ, focal length, f, and beam diameter, D, is given by

$$2\omega_0 = 2.44\frac{f\lambda}{D} \tag{146}$$

To achieve a tighter focus the beam size should be bigger. Because of the thermal lensing effect the size of the beam is smaller than estimated which, as a result, causes a bigger spot size.

The alignment of the CO_2 laser to the trap center is done as follows: After installing and aligning the AOM and the beam dump, the radio frequency (rf) power of the AOM is reduced until the CO_2 laser power on the first order is a few watts. Then it is easier to align the beam by looking at the burn marks on pieces of paper. Irises are placed at various locations along the beam path. Then the CO_2 laser is switched off and HeNe Laser is turned on by flipping the flip mirror. By using two mirrors and the irises, the CO_2 laser beam and HeNe laser beam are overlapped. After they are overlapped by only using the copper mirrors, the HeNe beam is adjusted to go through the both ZnSe window centers. Then the flip mirror is removed from the CO_2 laser beam path and CO_2 laser is turned on. The alignment up to this point is only good for low powers but at least it is going roughly through the center of the chamber and going into a beam dump or power meter. As it was mentioned before, because of the high power beam and it is dangerous, during the alignment process it is important to know where the beam is at any time. Then the irises are opened and transparent adhesive tapes are used to cover the holes on every iris. The CO_2 laser laser power is increased to its maximum power, ~ 60 W, and with a quick snapshot of the laser the holes on the tapes are examined. Then the HeNe is switched on and it is also corrected for the new holes and then the irises are readjusted. This process is repeated until no change is observed. At this point we tested the effective focus of our lens setup for a fixed distance between the two lenses. The lenses are installed on a rail and a paper is placed at the approximate focal spot of the laser. Amazingly the laser didn't ignite the paper but made a small hole. As the paper is moved away from the focus the paper started burning in flames. With this method we found the effective focal point of the lens system within 1 mm.

To do the fine adjustment of the CO_2 laser with the MOT, the HeNe laser is replaced with another laser that runs at 780 nm on resonance with the ^{87}Rb $F=2 \rightarrow F'=3$ transition. First this laser is overlapped with the CO_2 laser with a procedure similar to that explained for the HeNe laser. Then the lenses are carefully placed in the setup with a fixed distance between them which was found by a previous measurement. The convex lens is placed such that the focus is the center of the chamber. The concave lens is mounted on a z translater that allows the focal spot

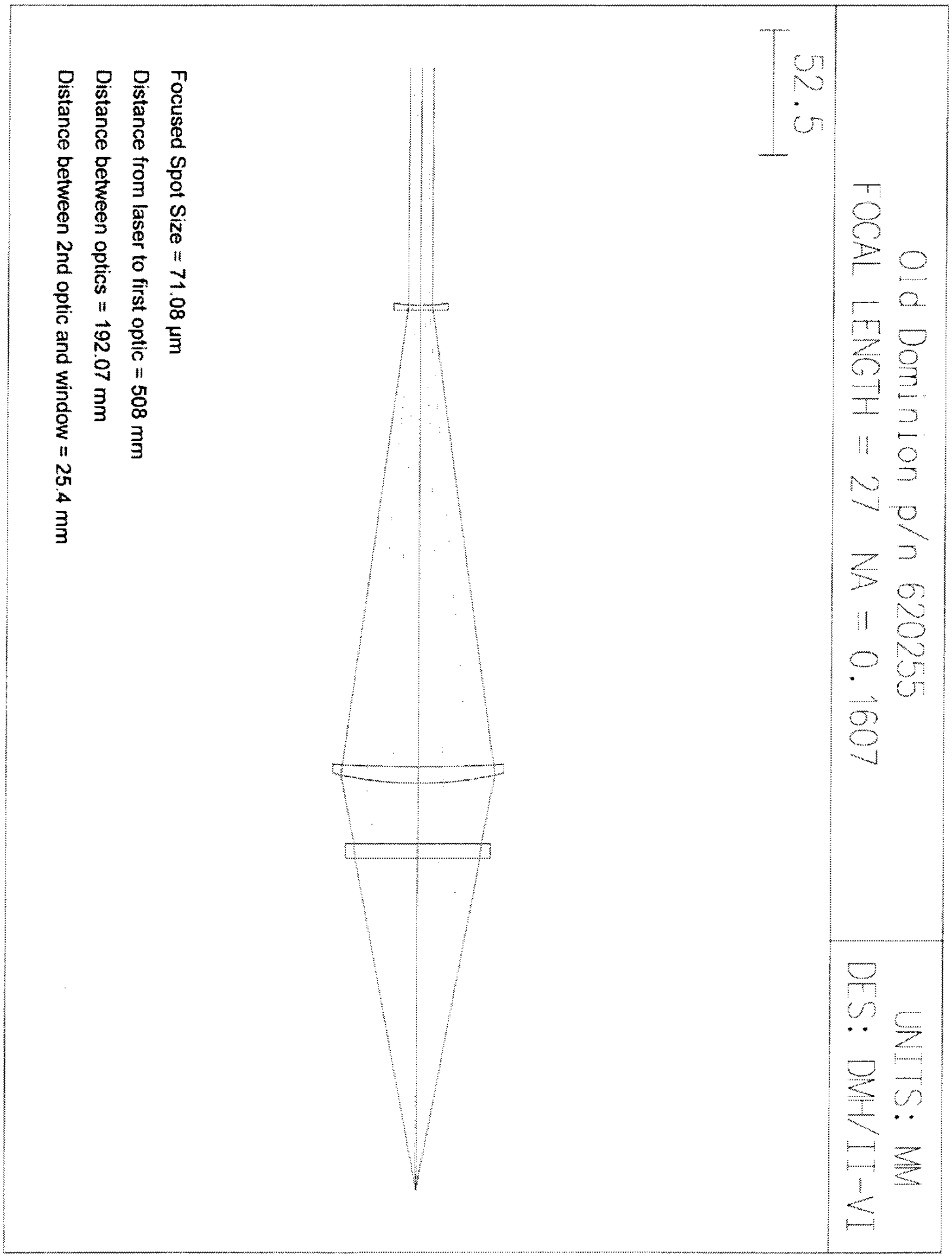

FIG. 16: The design is provided by ii-v infrared based on our experimental setup

to move vertically. The convex lens is mounted on a xy translater to be able to move the beam horizontally. First the 780 nm beam is overlapped with the MOT by looking at the pushing of the MOT at higher laser powers. In fact since the beam focus is much smaller than the MOT the pushing effect is less when the beam is going exactly through the center. Then the CO_2 laser is turned on and by using the xyz controls on the lenses and by looking at the loading images on the camera any signature of loading is looked for. To be able to see any loading first the repumper laser intensity and MOT laser detuning is adjusted. First MOT images are examined while keeping the CO_2 laser on and changing these parameters. As the repumper intensity is reduced and MOT laser is detuned, the MOT becomes compressed and get cooler and the effect of the CO_2 laser starts to appear on the MOT. Once that starts these loading parameters and xyz adjustments are optimized to maximize the collection of atoms around the CO_2 laser focus. Several iterations of this procedure are sufficient to maximize atom collection in the QUEST.

III.3.3 Probe Laser

In this section different probing schemes for the MOT and the QUEST, how the beam is generated and the characteristics of the probe beam important for the experiment are described. First of all, the probe beam is not a separate ECDL in the experiments done so far with this apparatus. Only two lasers are built and locked to a specific frequency. These are called the MOT laser and the repumper laser. Different probe lasers are generated by different choices of AOM configurations and the same output of the MOT or the repumper laser. The different probing schemes are depicted in Fig. 17.

The $F = 2 \rightarrow F' = 3$ probe laser setup is shown in Fig. 18. Three different AOMs are used in this setup. AOM2 (MOT AOM) and AOM3 (Probe AOM) are set at fixed frequencies while AOM1 varies for different probing schemes and MOT loading. During the initial MOT loading phase of the experiment AOM1 is set at +104.6 MHz which corresponds to a MOT laser frequency of 2.9 γ below the $F = 2 \rightarrow F' = 3$ cooling transition. This is experimentally found to be the best value for maximum loading. During the MOT loading phase AOM2 is on and set at -93 MHz and AOM3 is off and the setup generates the MOT laser. AOM1 is responsible for changing the detuning of the probe and the MOT lasers. When AOM2 is on and set at -93 MHz and AOM3 is also on and set at +67 MHz the setup produces the probe

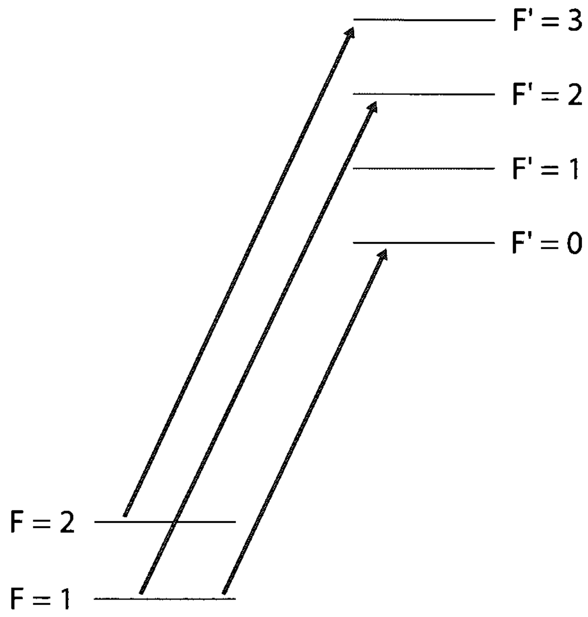

FIG. 17: Figure shows the three different probing schemes for different purposes (F = 1 → F′ = 0, F = 1 → F′ = 2 and F = 2 → F′ = 3).

laser. The frequency of the probe laser is changed by changing the AOM1 frequency. When AOM1 is set at 79.80 MHz the probe is on resonance with the F = 2 → F′ = 3 transition. The general equation to determine the MOT or probe laser frequency is

$$\delta = 2(|AOM1|) - (|AOM2|) + (|AOM3|) - 133.6 \tag{147}$$

where δ is the detuning in MHz from F = 2 → F′ = 3 transition. When both AOMs are off both lasers are turned off. When both AOMs are turned on MOT laser is also turned on along with the probe laser. To solve this problem mechanical shutters are installed to block MOT lasers during probing. To achieve these frequency settings the master laser is locked to the 2-3 crossover peak as shown in Fig. 19 in the saturation absorption signal, which will be explained later in this thesis.

The F = 2 → F′ = 3 probe laser setup is shown in Fig. 20. In this setup two AOMs are used. AOM1 is set at 78.6 MHz and also acts as a switch for the repumper laser. When this AOM is turned on the repumper is on resonance with the F = 1 → F′ = 2 repumping transition. This laser is responsible for pumping back the atoms that decay to the lower F = 1 hyperfine ground state level back to F = 2 ground state. Turning this AOM off and turning AOM2 on at -150.9 MHz produces the F =

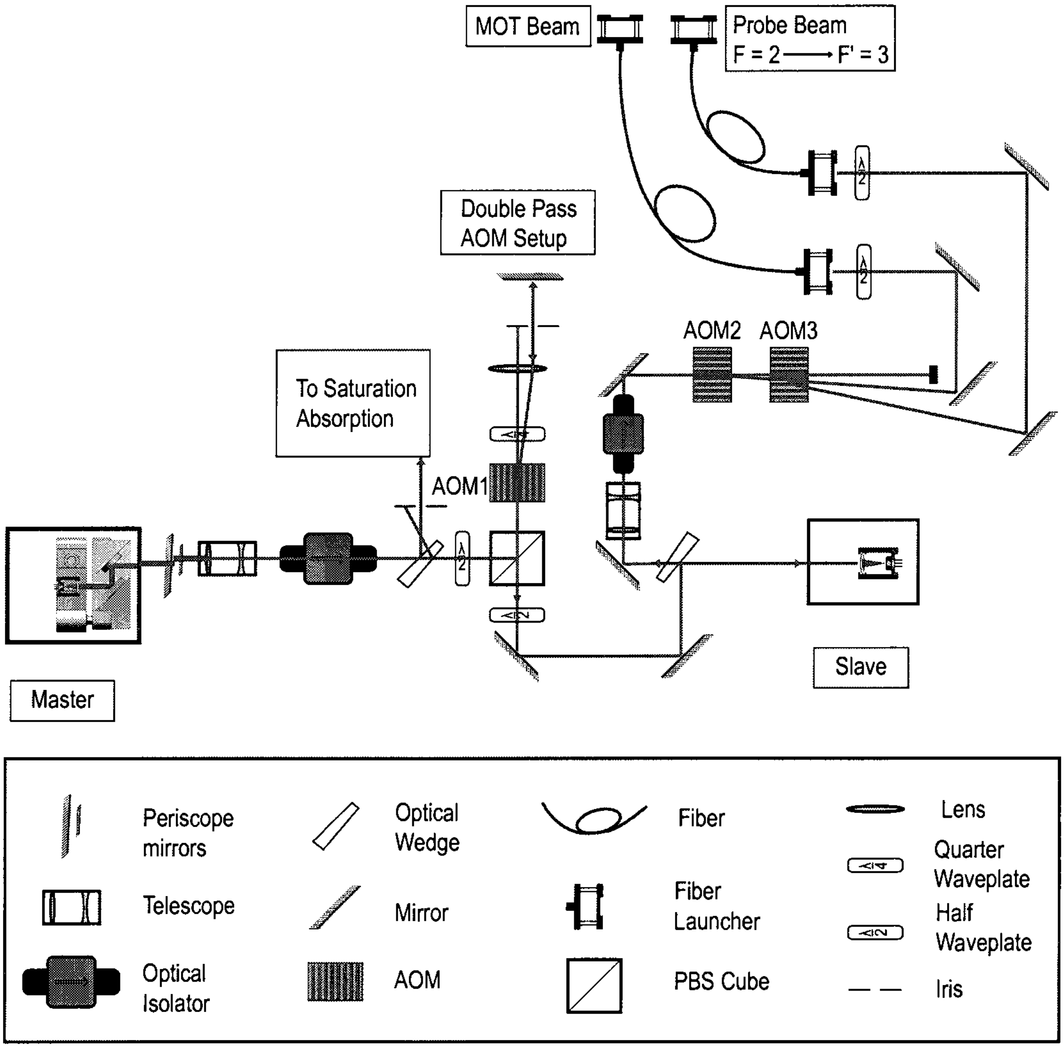

FIG. 18: Setup of the MOT and the F = 2 → F′ = 3 probe laser

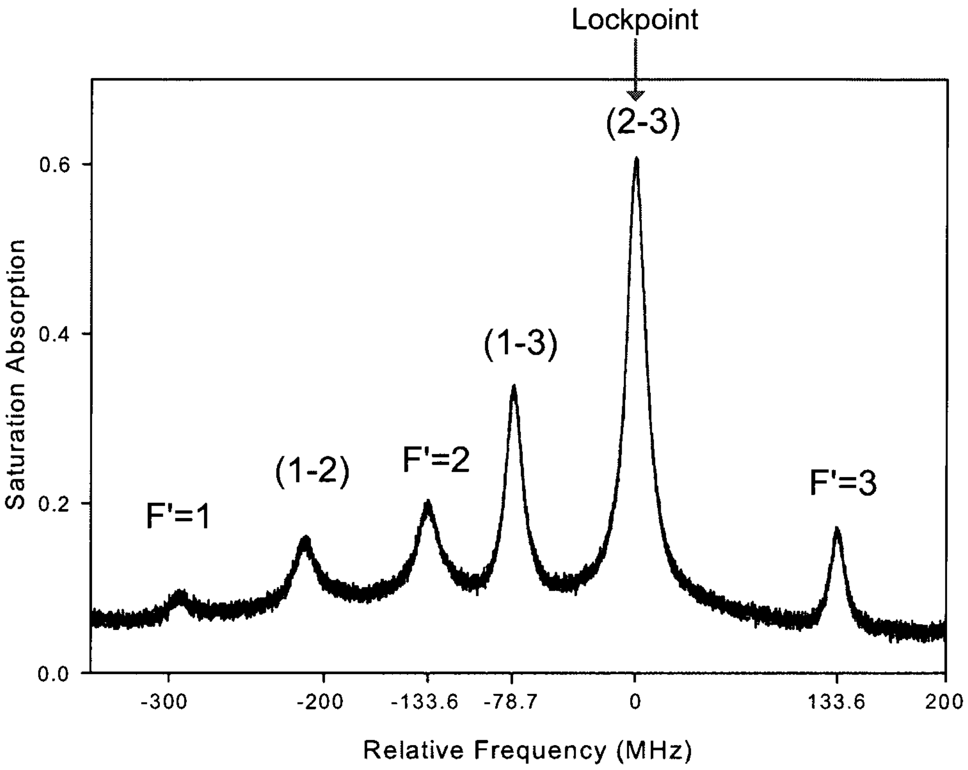

FIG. 19: Saturation absorption signal from F = 2 → F′ = 1,2,3

1 → F′ = 0 probe laser on resonance. This AOM is aligned by using two lenses with a focal length large enough to separate the deflected orders. The AOM is placed at the focus of the lens setup. This kind of setup allows changing the probe frequency without losing coupling into the fiber and also a remarkable turn on/off times for the laser (~ 25 ns). The detuning (δ) from optical resonance on the F = 1 → F′ = 0 transition is given by,

$$\delta = 150.9 - (|AOM2|) \tag{148}$$

The probe lasers are coupled into polarization preserving fibers and brought to the experiment table where the CO_2 dipole trap is produced. The polarization of the probe beam is linearly polarized after the fiber with an extinction ratio of ~ 24 dB. The beam is then expanded to a 3 mm $1/e^2$ radius and the collimation and wavefront distortion is checked by a shear plate interferometer. The beam is also imaged onto the CCD camera to make sure that the beam is free of diffraction fringes. Then the probe beam is sent to the off axis viewport on the vacuum chamber

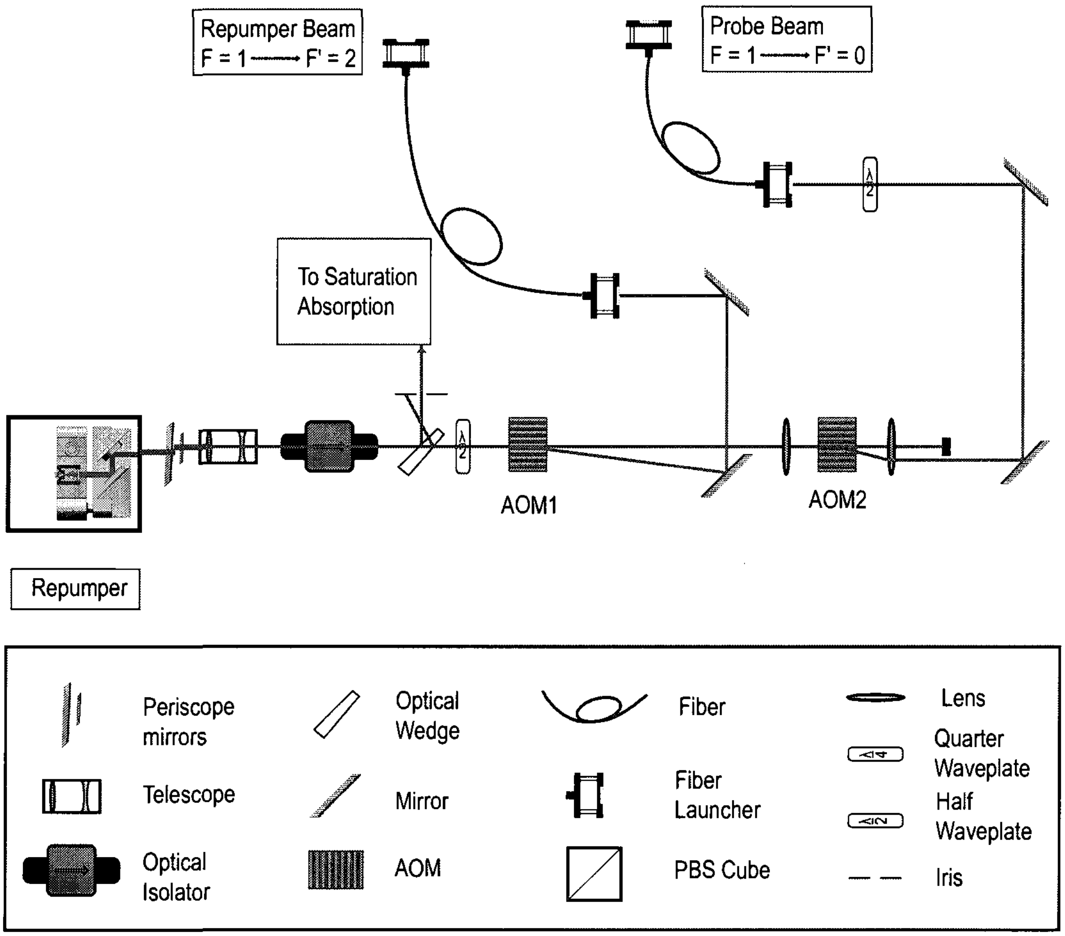

FIG. 20: Setup of the repumper and the F = 1 → F′ = 0 probe laser

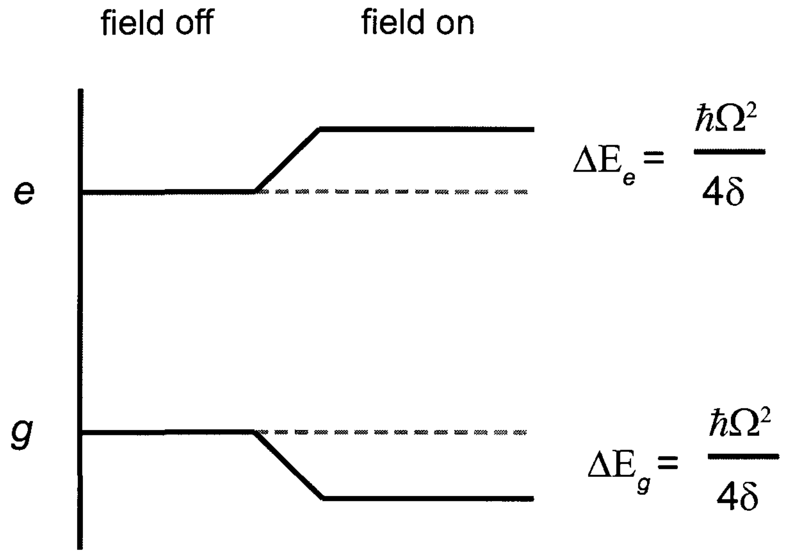

FIG. 21: Energy levels of a two level atom are shifted in the presence of an electric field.

for fluorescence measurements or from windows orthogonal to the ZnSe windows for absorption measurements. The switch between these two is done by a flip mirror. The linewidth of the probe is estimated to be ~ 600 kHz from heterodyne measurements done by beating the MOT and the repumper lasers against each other by locking them to different peaks (1-3 and 2-3 crossover peaks) separated by 78.6 MHz on the $F = 2 \rightarrow F' = 1,2,3$ saturated absorption signal, see Fig. 14.

III.3.4 Light Shift Laser

Another laser that is used in this experiment is what we call the "light shift laser". It is designed in a Littman-Metcalf configuration. A short cavity Littrow design laser would have been a better choice because of its higher power output and stability. This laser is not locked to a specific frequency during the measurements as it is set at -10 GHz off resonance and allowed to drift ~ ± 1 GHz. It is monitored during the data taking and whenever it drifted more than allowed the data taking is stopped and the laser frequency is tuned back.

With our experimental setup an optical depth of 160 or greater near the localization regime is achieved. At this high optical depth it is extremely difficult for light to penetrate to the middle of the sample where the density is the highest and localization of light is expected to happen. We use the Stark Shift effect to reduce the optical depth temporarily in which the energy levels are shifted by the external electric field, see Fig. 21. The electric field comes from the light shift laser. At first we used the CO_2 laser for this purpose but the turn on/off time of this laser is $\sim$ 1 μs which is too slow. The natural decay lifetime of ^{87}Rb D_2 ($5^2S_1/2 \rightarrow 5^2P_{3/2}$) transition is $\sim$ 27 ns. The optical excitation escape from the sample the while optical depth is increasing during the turn off of the CO_2 laser. Instead we use a separate diode laser which can be switched on/off in $\sim$ 25 ns with a similar setup used for the $F = 1 \rightarrow F' = 0$ probe laser described in the previous section. The total energy shift caused by an electric field for a two level atom is given by

$$\Delta E = \frac{\hbar\Omega^2}{2\delta} \tag{149}$$

where Ω is called the Rabi oscillation frequency [53] [1].

$$\Omega^2 = \frac{E_0^2}{\hbar^2}|\langle e|er|g\rangle|^2 \tag{150}$$

E_0 is the amplitude of the laser field and $|\langle e|er|g\rangle|$ is the dipole moment that depends on the wavefunctions of the ground and the excited states. The effective far detuned dipole moment for ^{87}Rb D_2 line with linearly (π) polarized light is $2.069\,36(43) \cdot 10^{-29}$ C.m [43]. The relation between the amplitude of the light field and the cycle averaged intensity is

$$I = \frac{1}{2}\varepsilon_0 c E_0^2 \tag{151}$$

To give some representative numbers, the light shift laser is detuned 10 GHz to the red of the D_2 line and is focused to a spot size of 50 μm radius. With a laser power of 11 mW the energy levels are shifted by $\sim$ 20 MHz which reduces the optical depth of the trap from 160 to 3.5. Even though this laser is 10 GHz away from resonance we still detect a few photons scattered by this laser during data taking but they are easily subtracted from the total signal.

This laser aligned so that it is overlapped with the probe beam. The alignment is done by coupling the two beams into the same optical fiber. This way the probe and the light shift laser is focused to a same spot on the sample. This allows us to probe the highest density region in the trap but also limits us using a collimated beam as in no light shift measurements.

III.4 SAMPLE FORMATION

III.4.1 Saturated Absorption

Since the data acquisition process normally takes many hours it is crucial to have stable and locked lasers. The lasers are locked to a reference signal that controls the piezo which in turn compensates drifts in laser frequency by tilting the feedback mirror. This external reference signal is generated via saturated absorption spectroscopy. The laser is scanned around saturation absorption peaks by applying 0-15V ramp to the piezo. In this section the saturated absorption and laser locking procedure is explained. First, the laser wavelength is brought close to the Rb resonances around 780 nm by using the mechanical horizontal actuator and also checking the wavelength with a wavemeter. After the lasers are mechanically tuned onto an absorption line fluorescence is observed in the Rb cell when observed with an IR viewer. The beam is then sent to the saturated absorption setup as shown in Fig. 22. The two beams going in the forward direction towards the photodiode detector are called probe beams and the strong beam overlapping one of the probe beams going in the reverse direction is called the pump beam. Since the cell is at room temperature, the Rb atoms have a Maxwell-Boltzmann velocity distribution and the Doppler broadening full width at half maximum is $\sim$ 500 MHz. Fig. 23 shows a theoretical Doppler broadened absorption spectrum of Rb for the D_2 ($5^2S_{1/2} \rightarrow 5^2P_{3/2}$) transition. The Doppler broadened saturation absorption spectrum does not show hyperfine levels of $5^2S_{1/2} \rightarrow 5^2P_{3/2}$ transition for ^{87}Rb which form a band about 400 MHz wide.

As it is shown in Fig. 22, the beam splitter reflects 2% of the incoming laser beam from each surface. The pump beam is aligned so that it overlaps one of the reflected probe beams. Since the two beams are counter propagating and they have the same frequency, only the atoms with $v_x = 0$ (x is the same direction with the laser beams) will be at resonance with both beams. Other atoms moving with different velocities in the same direction will interact with the probe or the pump beam depending on the laser detuning from the atom's resonance frequency and the velocity of the atom. For example if the laser is detuned below resonance by $\Delta f = f - f_L$, only the atoms with velocity $v_x = c(\frac{f}{f_L} - 1)$ going towards the laser beam will be in resonance with the laser and absorb the light. The strong pump beam saturates the $v_x = 0$ distribution of atoms causing the probe beam going through the cell to have less absorption and

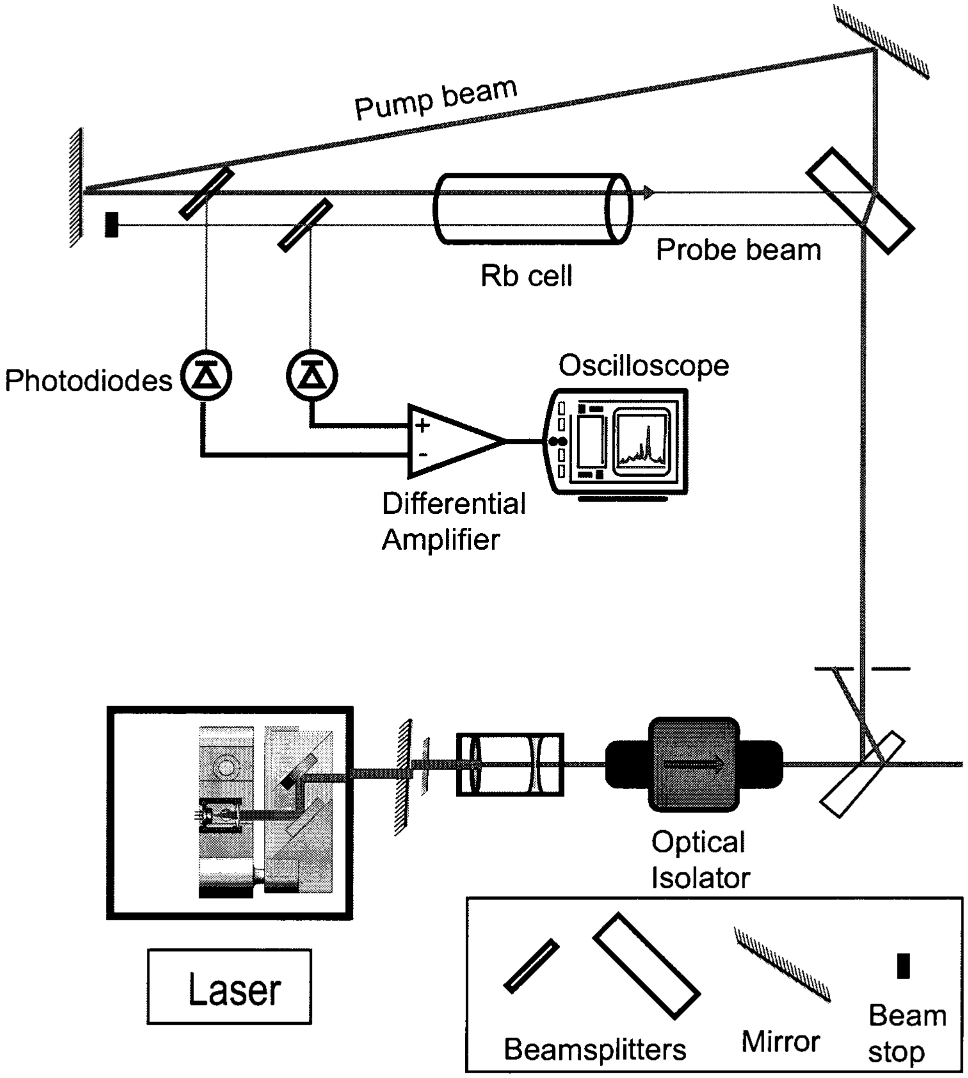

FIG. 22: A schematic of saturation absorption spectrometer.

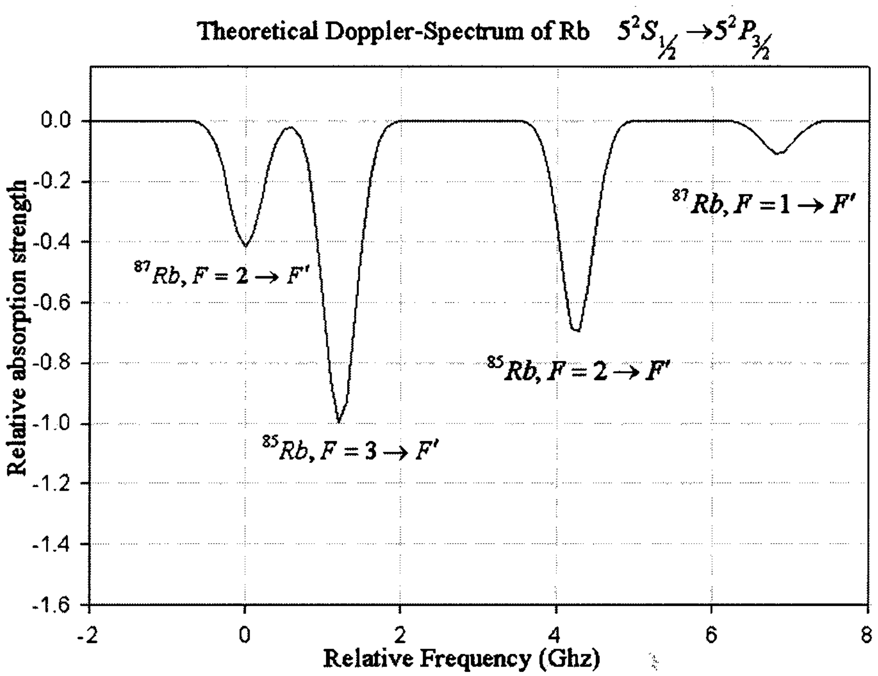

FIG. 23: Doppler broadened absorption spectrum of Rb for the D_2 ($5^2S_{1/2} \rightarrow 5^2P_{3/2}$) transition at room temperature.

generating greater intensity reading at the photodiode. The other probe beam goes to the photodiode with more absorption given by the Doppler broadened profile as shown in Fig. 22. If this Doppler broadened absorption signal is subtracted from the signal obtained from the saturated probe beam by using a differential amplifier we obtain a Doppler-free saturation absorption profile as shown in Fig. 24. This figure shows resonance transitions from ^{87}Rb for F = 1 → F′ = 0,1,2 transitions and there are more absorption peaks than expected. Three of them are the expected F′ = 0,1,2 transitions and the other three are so-called crossover peaks. Crossover peaks occur when a velocity distribution of atoms other than $v_x = 0$ are in resonance with both pump and probe beams. This can happen when the laser frequency is halfway between two transitions. As it is shown in Fig. 25 with a laser frequency f_L tuned 133.3 MHz below the F = 2 → F′ = 3 transition, f_3, and 133.3 MHz above the F = 2 → F′ = 2 transition, f_2, atoms going towards the pump beam with $v_x = c(\frac{f_2}{f_L} - 1)$ are in resonance with the F = 2 → F′ = 3 transition with the pump beam and since the same velocity distribution of atoms are going away from the probe beam, they

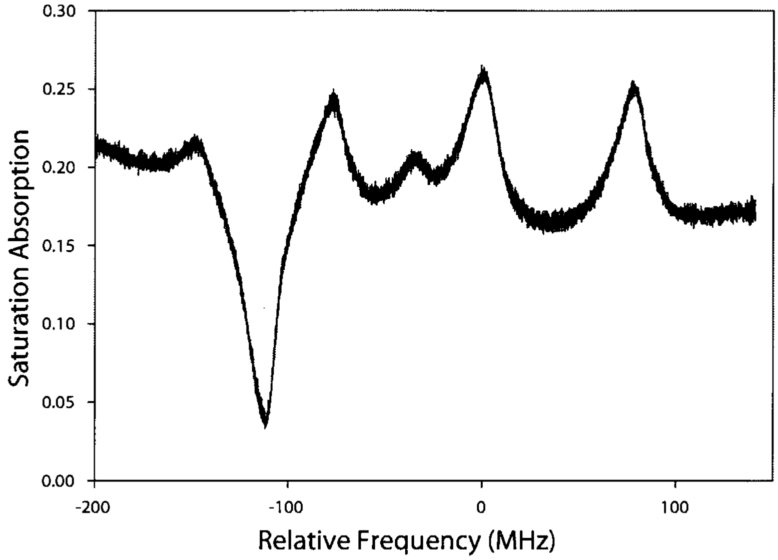

FIG. 24: Saturation absorption signal from the F = 1 → F′ = 0,1,2 transitions.

are in resonance with the F = 2 → F′ = 2 transition with the probe beam. In other words, for laser frequency f_L, the atoms with velocity v_x (towards the pump beam) see the pump beam Doppler shifted to the red of f_3 and they see the probe beam Doppler shifted to the blue of f_2.

$$f_3 = f_L(1 + \frac{v_x}{c}) \tag{152}$$

$$f_2 = f_L(1 - \frac{v_x}{c}) \tag{153}$$

Adding both equations gives the crossover resonance condition:

$$f_L = \left(\frac{f_3 + f_2}{2}\right) \tag{154}$$

The requirements to see crossover peaks are that both transitions should share the same ground state and the separation between two transition frequencies should not be greater than the Doppler width (500 MHz).

To lock the laser, the necessary error signal is obtained by modulating the laser current at 15 kHz. The modulated saturation absorption signal is then sent to a lock-in amplifier which generates the derivative of the absorption peaks. This dispersive signal is integrated and applied to the piezo attached to the horizontal control of the ECDL.

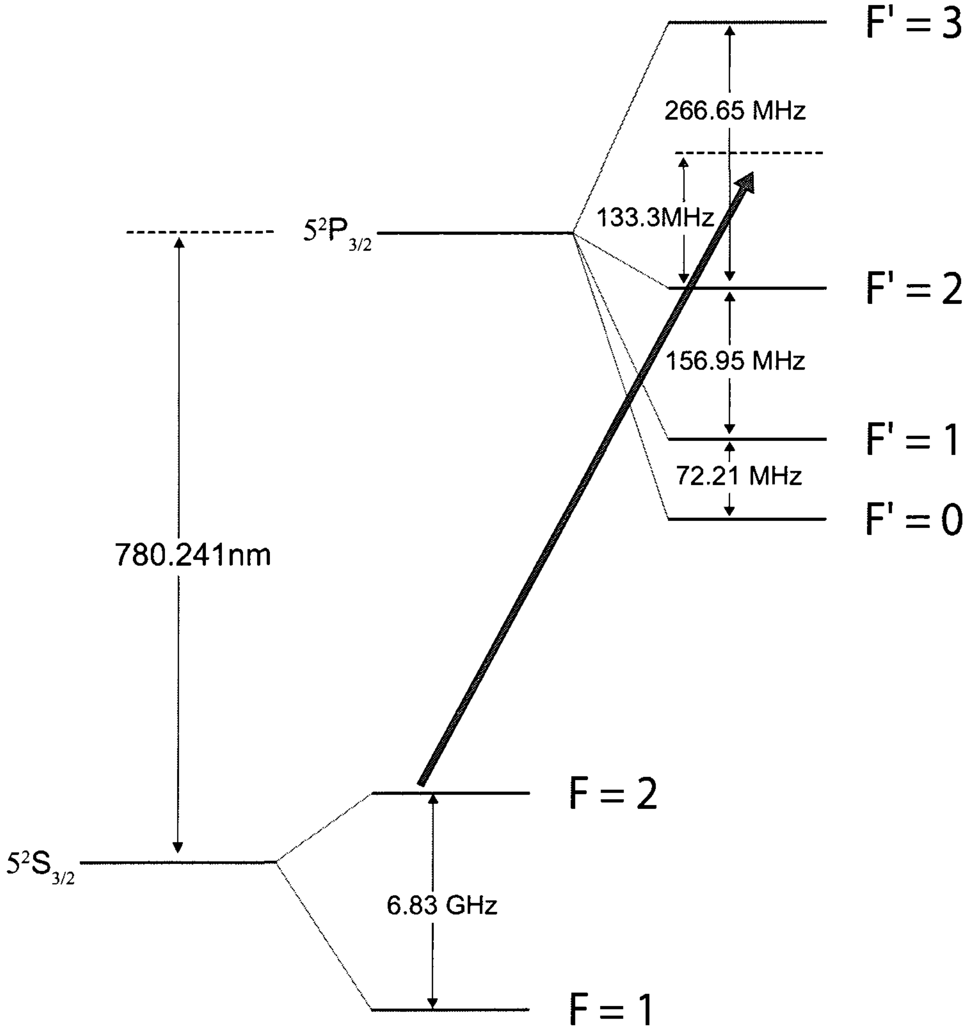

FIG. 25: Energy spectrum of ^{87}Rb for the D_2 ($5^2S_{1/2} \rightarrow 5^2P_{3/2}$) transition.

III.4.2 Control System

During the initial phases of the experiment, hardware based electronics was used to control the experiment. The AOMs that switch and tune the lasers, the CCD camera and shutters were controlled by TTL pulses generated by 2 four-channel pulse generators from Quantum Composers. This setup was capable of producing 8 channels output without using any multiplexing which is needed for controlling the lasers. As the experiment grew, more channels with multiplexing features and complex timing sequences that includes digital signals switching between different voltage levels were needed. We acquired a PCI-DIO-32-HS digital card from National Instruments which is capable of 32 digital high speed outputs; only 16 of these channels are used for this experiment. The internal clock of the card is 2 MHz which allows us up to timing 500 ns resolution in timing the experiment which is sufficient for most of the experiments. When a finer resolution is needed a Quantum Composers pulse generator triggered by the PCI-DIO-32-HS is used. This digital card is controlled by a Labview program, see Appendix D.

Every different experiment requires a different timing protocol which is generated by simply changing 1 and 0 for a specific time. (1: channel on, 0: channel off) In Fig. 80 the control interface of the program for QUEST imaging is shown for reference. Column 1 is the timing and Column 2 is the status of the channels at any specific time in the sequence.

The frequency tuning of the AOMs are done by voltage controlled oscillators (VCO). The output of the VCOs are fed into 800 mW rf amplifiers for most of the AOMs. The 200 MHz AOM that is used in light shift laser requires a 1.6 W amplifier. During the trap loading, switching the VCOs on/off with a fixed input voltage or fixed attenuation on the output of the rf amplifiers is not sufficient as these parameters are needed to be changed during the course of a duty cycle a few times. To achieve this digital voltage level boxes are built, see Fig. 27 [56]. These circuits uses a chip (Maxim REF01) that provides + 10 V voltage reference with 10μV ripple noise. By using these chips multiple times in a circuit produces 10 V, 20V, 30V reference voltages. With a proper choice of potentiometers and resistors it is possible to make any voltage level needed for the experiment. Adding a digital switch (Maxim DG419) to the circuit allows formation of more complex digital outputs. These boxes are used to switch the frequency of the double pass AOM that changes the frequency of the main MOT beams, to attenuate the MOT and the repumper laser during the

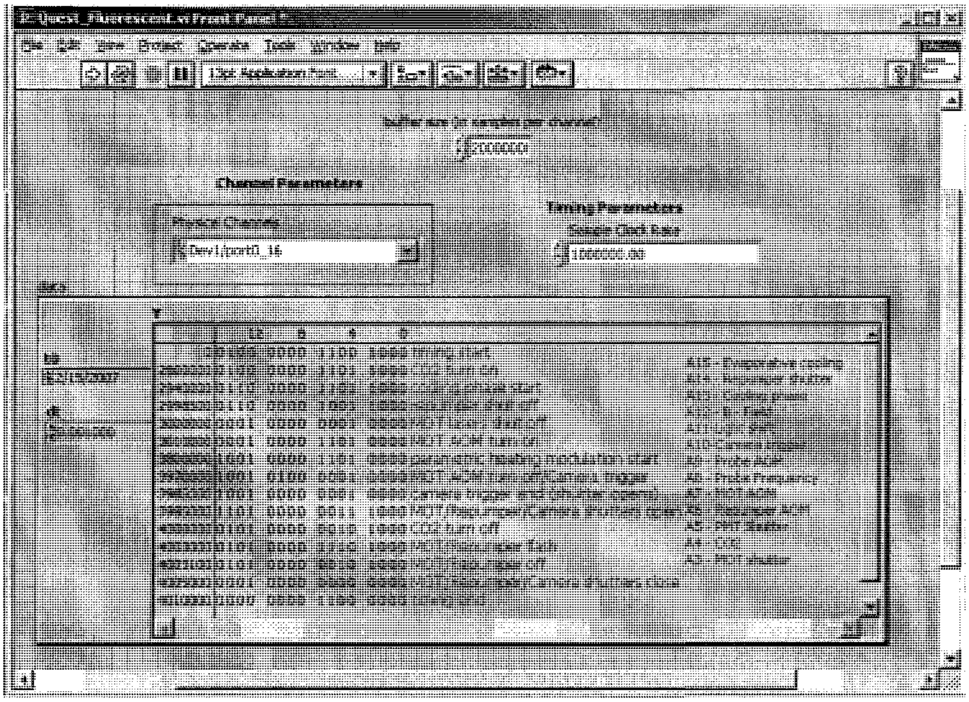

FIG. 26: Labview program controlling the Quest imaging.

cooling phase of the trap loading process.

To do the parametric heating measurement which will be explained in the next chapter, an op-amp voltage adder is combined with the digital voltage level circuit. The control for the CO_2 laser AOM is a 0-1 V analog input which is provided by one of these modified boxes. It allows us to add a known frequency and amplitude sinusoidal noise to the 1V output to modulate the CO_2 laser intensity.

Frequency tuning is done by a double pass AOM setup before injecting the master laser beam into the slave that allows switching to different frequencies of the probe and the MOT beams without losing coupling into the fiber. The frequency of the double pass is switched to different frequencies ranging from 72 MHz to 104.6 MHz. This AOM has the most efficiency around 85 MHz. The AOM efficiency drops significantly after 70 MHz and the slave can not follow after that. The AOM is tilted so that the injected power to the slave laser is still sufficient at 72 MHz and 104.6 MHz.

During the course of an experimental cycle the temperature stability of the AOMs is also very important. We realized that turning off an AOM even for 1 s cools the AOM crystal, resulting in a change in the direction of the beam which decreases

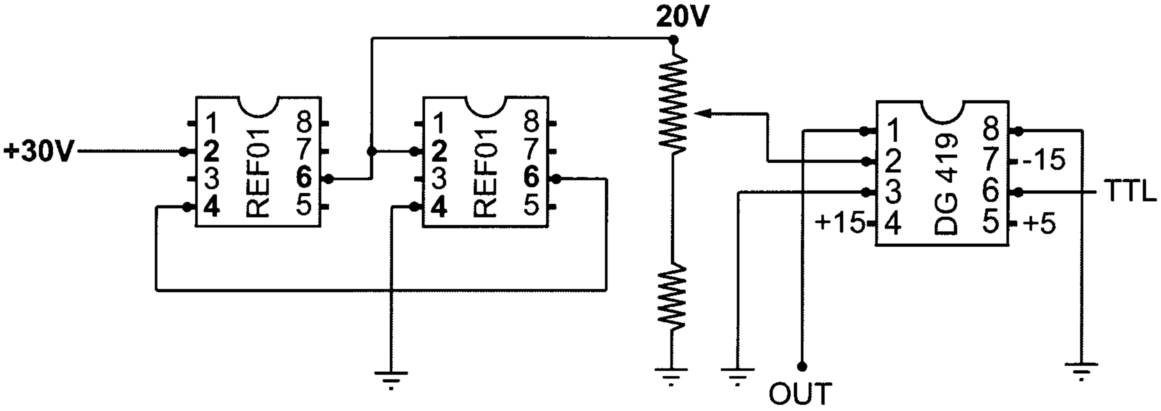

FIG. 27: Circuit of a sample digital voltage level box. This circuit output is switching between voltages on pin 2 and 8 of DG419.

the coupling efficiency to the fibers. A similar effect is also observed in the CO_2 laser AOM which was described in the previous section. This problem was solved by leaving the AOMs on all the time and turn them off for short periods of time where needed. To prevent the MOT beams to enter into the chamber during trap hold time we installed mechanical shutters from Uniblitz. These shutters have a few ms open/close time. Another solution would be switching AOMs with a different frequency that has minimal efficiency. This way the AOM would stay at a fixed temperature and also would be switched off. We did not try this as the shutter solution were sufficient. Also having shutters guarantees that that there is absolutely no MOT laser leak into the trap during the hold time that would heat up the sample.

The MOT is continuously monitored with a Sanyo CCD camera and a TV monitor. The B field balancing is done by using this monitor and turning off the current to the B field and leaving the MOT lasers on. When the field is balanced this generates a uniform diffusion of fluorescence in every direction as seen on the monitor. Three shim coils are used to balance the B field. The current supplied to the anti-Helmholtz coils is switched on/off in about 1 m.

III.4.3 MOT Loading

The last two sections of this chapter are about how to put together all the pieces that have been described in the previous sections, to enable formation of the Magneto Optical Trap and the QUEST. As was explained in the previous chapter, a MOT requires 6 laser beams at the correct frequency and polarization centered in a good vacuum that has enough flow of atoms to be cooled and trapped and a pair of anti-Helmholtz coils with correct current direction.

The layout of the required laser setup for the MOT formation was shown in section III.3.3 in Fig. 18 and in Fig. 20. The MOT laser is tuned $\sim 2.9\,\gamma$ below resonance to $\mathrm{F}=2 \rightarrow \mathrm{F}'=3$ transition of ^{87}Rb where $\gamma \sim 6$ MHz is the natural linewidth of the transition. To generate this frequency the master laser saturation absorption signal is locked to the 2-3 crossover resonance which is 133.6 MHz below the $\mathrm{F}=2 \rightarrow \mathrm{F}'=3$ transition. The master laser is then sent through a double pass setup where it picks up a 2×104.6 MHz frequency shift before being injected into the slave laser. The output of the slave laser is ~ 80 mW. The slave laser is directed through a telescope that reduces the beam size by one third to decrease the switching times and also to minimize the losses when the beam goes through the optical isolator. The first of the two AOMs seen in Fig. 18 is the MOT AOM which is set at 93 MHz to bring the MOT laser to -2.9γ below resonance, a level which is determined experimentally to optimize MOT performance. Selection of this value depends on the MOT laser intensity. For example, before adding the slave laser into the setup, power available for MOT was less and the detuning was set at -2.5γ. The second AOM is off during the MOT loading. The beam is then injected into a polarization preserving optical fiber. To ensure a maximum extinction ratio a half wave plate is placed before the fiber launcher. If the polarization of the beam is not matched with the slow axis of the fiber the polarization of the beam at the output oscillates which causes intensity oscillations after the polarizing beamsplitter cube (PBS Cube). A schematic of the setup is shown in Fig. 28.

The laser beam is then carried by the fiber to a different optical table where the MOT and the QUEST experiments are executed. The total laser power at this end is 24 mW. The beam is expanded to a size of $\sim$10 mm $1/e^2$ radius with a 5X telescope. The polarization of the expanded beam is then rotated by a half wave plate such that 2/3 of the beam is reflected and 1/3 is transmitted as seen in Fig. 28. This setup forms three bidirectional and equal intensity beams. The polarization of each of these linearly polarized beams then is transformed to circular polarization via quarter wave plates. The beams are then retroreflected and passed through another quarter wave plate twice to generate the required setup needed for trapping the atoms. Together with the correct current direction in the anti-Helmholtz coils, a

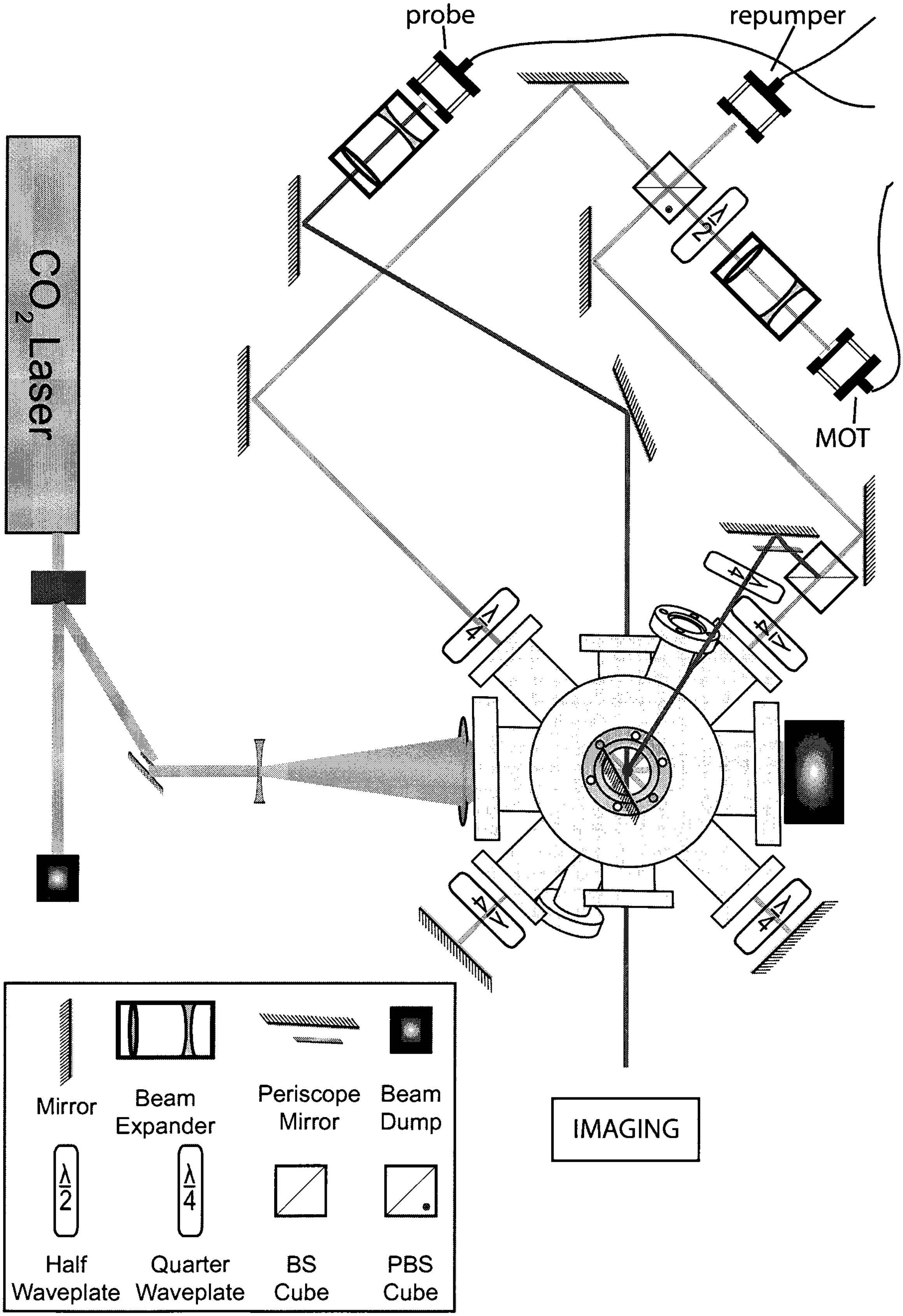

FIG. 28: Experimental setup of MOT and Quest

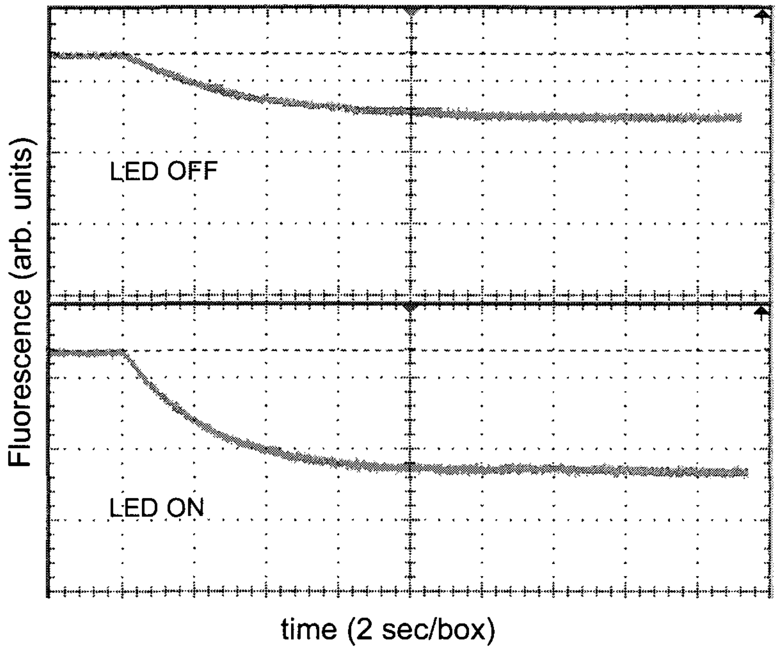

FIG. 29: LIAD assisted MOT loading

bright spot on the TV monitor with a smile on the graduate students' face appears. If it doesn't, the current direction is changed or the quarter wave plates are rotated by 90^0. The retroreflected beam alignment is first done by observing coupling back into the fiber. A more stable MOT is attained when the retroreflected beams are misaligned a little. This is partly because the MOT scatters most of the incident beam causing an imbalance at perfect alignment and partly because the beam that is coupled back into the fiber disturbs the frequency lock of the laser.

The Rb required by the experiment is provided by the getters as explained in the first part of this chapter. Getter current is usually kept around 3.5 A. Getters are run along with the UV LEDs to improve the rate and quantity of atom loading the MOT. Fig. 29 shows the difference between MOT loading with and without LIAD. As it can be seen from the measurement almost twice the number of atoms are loaded into the MOT with the use of UV LEDs. This LIAD technique also helps in better QUEST loading as the background gas pressure, when the LEDs are off, is lower thus increasing the lifetime of the trap.

During the cooling and trapping of the atoms in the MOT an atom, after about 2000 excitations, decays to the lower hyperfine ground state F = 1. Without pumping these atoms back to F = 2 it isn't possible to trap the atoms because eventually all

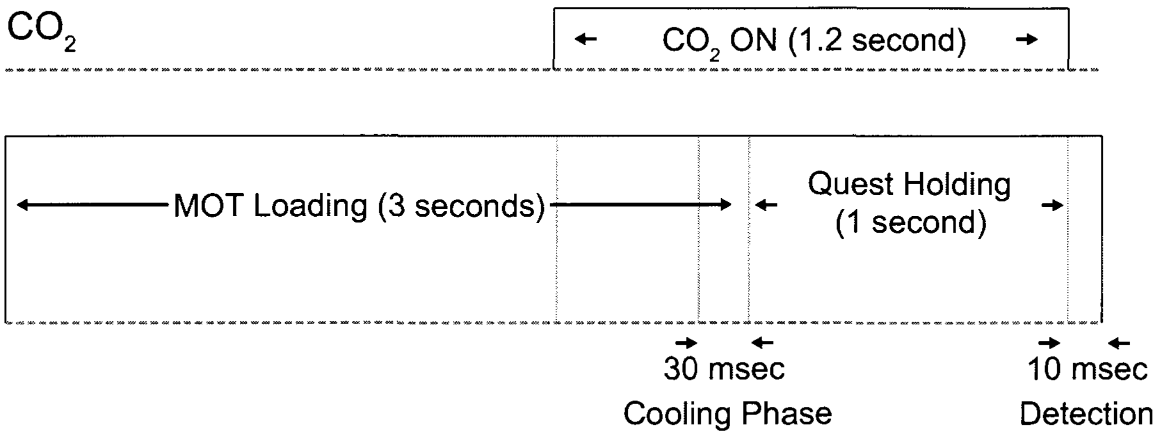

FIG. 30: Quest loading timing

the atoms decay to F = 1 and leave the trap. To solve this problem a separate laser called a repumper laser is built as shown in Fig. 20. The setup is similar to the MOT laser but simpler. The laser is locked to a 1-2 crossover peak in saturation absorption which is 78.55 MHz to the red of $F = 1 \rightarrow F' = 2$ transition. An AOM tuned at 78.55 MHz shifts the beams frequency to on-resonance, and also acts as a switch for the repumper laser. This repumper beam is combined with the beam at the PBS cube. The polarization of the beam is not important so no adjustments are needed.

III.4.4 Quest Loading

Once the MOT is loaded, the QUEST is loaded by focusing the CO_2 laser to the middle of the MOT. A brief timing sequence is shown in Fig. 30. After the MOT is loaded for 3 seconds, the atom sample has a temperature of about 100 μK. The CO_2 laser is turned on 200 ms before MOT and repumper lasers are extinguished. We studied the CO_2 laser overlap time with the laser by itself and we concluded that this has little or no effect in QUEST loading. In fact the CO_2 laser by itself overlapped onto the MOT doesn't seem to load any atoms into the trap. The MOT acts as a reservoir for the trap and increasing overlap of the CO_2 laser and the MOT greatly improves loading. One can achieve this by increasing the spot size which reduces the well depth and the density of the trap. Another way is compressing and cooling the MOT to increase the flux of atoms through the CO_2 laser and also decrease the temperature of the atoms for better loading. To achieve this, at 30 ms before the

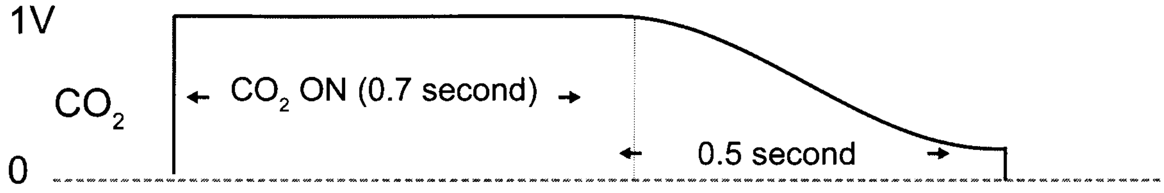

FIG. 31: Modified CO_2 laser power control for evaporative cooling

end of the MOT loading phase the MOT laser is detuned $\sim -14\gamma$ (84 MHz) below resonance and also the laser power is reduced to 2 mW from 24 mW. At the same time the repumper laser power is also decreased to $\sim$6 μW . This compresses and cools the MOT and with the CO_2 laser overlapped the trap enters into a temporal dark spot phase. We call this stage of trap loading a cooling phase. At the end of this cooling phase, the repumper laser is turned off 1.5 ms before the MOT laser to ensure pumping of all the atoms from the F = 2 to F =1 ground state. Then the loaded atoms are held by the CO_2 laser for 1 second. During this trap hold time the atom sample undergoes natural evaporation and rethermalization. Once the atoms sample reaches equilibrium the CO_2 laser is turned off and the experiments are done.

The natural evaporation takes place mostly in the first 0.5 second of trap hold time. After this for some of the experiments we ramped the CO_2 laser power down slowly during the last 0.5 second of the trap hold time for forced evaporative cooling. This process decreases the well depth slowly, letting the more energetic atoms in the Maxwell-Boltzmann distribution escape and rethermalizing to achieve a colder sample. One disadvantage of this process is obviously losing atoms from the trap. But since the trap gets colder after evaporative cooling the atoms sit on the average deep in the potential well, this reducing the size of the sample. So the density of the trap is not effected much from this process. The ramp signal seen in Fig. 31 is generated by adding half of a low frequency function generator output to the voltage controlling the CO_2 laser intensity with an op-amp voltage adder.

Once the QUEST is loaded it is optimized by changing the trap loading parameters. The parameters are from the most effective to the least: Repumper laser intensity during cooling phase, MOT laser detuning during cooling phase, MOT laser intensity during cooling phase, CO_2 laser alignment, cooling phase time, MOT laser detuning during MOT loading, repumper laser turn off time with respect to the MOT laser and CO_2 laser turn on time. The optimization is done by maximizing the total number of atoms transferred to the QUEST. This cycle is iterated until no improvement is achieved. The average number of atoms transferred is $\sim 10\%$ of the number in the MOT.

CHAPTER IV

SAMPLE CHARACTERISTICS

IV.1 SAMPLE CHARACTERIZATION

Once the QUEST is formed and optimized it is necessary to characterize the sample before starting the data taking. These characteristics are the sample temperature, the number of atoms and the Gaussian radii of the cloud. It is important to know the density of the QUEST in order to calculate the Ioffe-Regel parameter ($k\ell$). Here ℓ is the mean free path and is given by

$$\ell = \frac{1}{n\sigma} \tag{155}$$

where n is the average density and σ the resonance cross-section for light scattering. Because the sample is inhomogeneous the mean free path varies spatially throughout the sample, with the smallest $k\ell$ attained at the trap center where the density is the highest. For a Gaussian distribution of atoms in a QUEST given by

$$n(r,z) = n_0 \mathrm{exp}(-\frac{r^2}{2r_0^2} - \frac{z^2}{2z_0^2}), \tag{156}$$

the peak density at the trap center is

$$n_0 = \frac{N}{(2\pi)^{3/2} r_0^2 z_0}. \tag{157}$$

From Eq. 157 it is clearly essential to find the total number of atoms loaded into the quest N and also the radial r_0 and axial, z_0 Gaussian radii of the QUEST. These numbers can be obtained by doing an absorption measurement on the QUEST. When a laser beam tuned near resonance is overlapped with the QUEST the atoms will cast a shadow in the beam due to scattering of light from the QUEST. The intensity of the transmitted beam decreases as light travels through the medium, varying according to the Beer-Lambert Law,

$$\frac{I_T(x,y)}{I_0} = exp[-b(x,y)], \tag{158}$$

where I_0 is the incident intensity and b is the optical depth. The peak optical depth through the trap center is

$$b_0 = \sqrt{2\pi} n_0 \sigma_0 r_0. \tag{159}$$

Here n_0 is the peak density at the trap center, σ_0 is the on resonance light scattering cross section. When the shadow of the QUEST is imaged on a CCD camera it is possible to measure the $I_T(x,y)/I_0$ and the peak density, n_0 and total number of atoms, N can easily be calculated from this measurement. But our experimental setup with image resolution of $\sim$ 1 or 2 pixels with pixel size of 24 μm makes it almost impossible to make accurate measurements of optical depth of the QUEST, which has typical dimensions of $\sim$ 20 μm by 400 μm. Also diffraction, optical pumping and lensing effects produce systematic effects that are not always trivial to correct. Even though it is possible to do this measurement by expanding the QUEST to a size much bigger than the image resolution, then signal to noise issues appear. But these measurements can easily be done on a MOT, which has dimensions of $\sim$ 700 μm by 800 μm, without any signal to noise and resolution issues. Once the total number of atoms in the MOT is known, a comparison of total integrated signal of the MOT and the QUEST obtained from CCD images gives the transfer efficiency from the MOT to the QUEST. From this number the total number of atoms in the QUEST is calculated.

To find the the radial (r_0) and axial (z_0) Gaussian radii of the QUEST, we need to know the spatial shape of the trapping potential formed by focusing the CO_2 laser. In cylindrical coordinates the dipole potential formed by focusing a Gaussian beam with intensity

$$I(r,z,\phi) = I_0 \frac{1}{1+(z/z_R)^2} \exp(-2r^2/w_0^2) \tag{160}$$

equals

$$U(r,z,\phi) = -U_0 \frac{1}{1+(z/z_R)^2} \exp(-2r^2/w_0^2). \tag{161}$$

I_0 is the CO_2 laser beam peak intensity and it is given by $I_0 = 2P_0/\pi w_0^2$ where P_0 is the total CO_2 laser power. w_0 is called the beam waist which is defined as $1/e^2$ beam radius at the focus of the laser and z_R is called the Rayleigh range with $z_R = \pi w_0^2/\lambda$. λ is the wavelength of the CO_2 laser, 10.6 μm. U_0 is defined as the well depth of the potential.

The cold atoms that are held in the dipole trap potential sit near the bottom of the trap according to their thermal energy, $k_B T$. For a typical dipole trap this energy is much smaller than the potential well depth, U_0. So the radial and axial size of the sample is much smaller than the beam waist and the Rayleigh range. Then the potential can be well approximated by a harmonic oscillator form,

$$U(r, z, \phi) \approx -U_0 \left[1 - \left(\frac{z}{z_R^2} \right)^2 - 2 \left(\frac{r}{w_0^2} \right)^2 \right]. \tag{162}$$

If we define the radial and axial oscillation frequencies of a trapped atom as ω_r and ω_z respectively, the harmonic potential can be written as

$$U(r, z, \phi) = -U_0 + \frac{1}{2} m \omega_r^2 r^2 + \frac{1}{2} m \omega_z^2 z^2. \tag{163}$$

From Eq. 162 and 163, the harmonic oscillation frequencies of a trapped atom at the focus of the CO_2 laser are

$$w_r = \sqrt{\frac{4U_0}{m w_0^2}} \qquad and \qquad w_z = \sqrt{\frac{2U_0}{m z_R^2}}. \tag{164}$$

These oscillation frequencies are measured through parametric resonance measurements which will be explained in Section IV.1.2.

IV.1.1 Imaging

A very important step in sample characterization is imaging of the sample. Two different types of imaging are used in characterizing the sample. One is absorption imaging and the other is the fluorescence imaging. The latter is used during QUEST optimization and to find the transfer efficiency from MOT to the QUEST. Absorption imaging is, on the other hand, used to calculate the optical depth, density and the total number of atoms in the MOT.

Fig. 32 shows a schematic diagram of the imaging system for fluorescence imaging. The focal length of the first lens that collects the fluorescence from the sample is f = 75 mm and it is located at a distance of 2f from the sample. This lens is a high quality 2 inch diameter AR coated achromatic doublet. The shutter located at the focus of this lens acts as a spatial filter and prevents unwanted background signals from entering the charged couple device (CCD) Camera. Two lenses also of focal length f are located after the shutter setup and transfer the image to the CCD camera. The CCD camera used here is a Princeton Instruments (Roper Scientific) LN/CCD,with a Tektronix 512x512 pixel array. Each pixel is 24x24 μm in size. The camera is cooled with liquid Nitrogen to -90 ^{0}C to achieve very low thermal noise. The timing of the florescence imaging of the MOT and the QUEST are shown in Fig. 34 and in Fig. 35. The fluorescence signal is obtained by reflashing the MOT

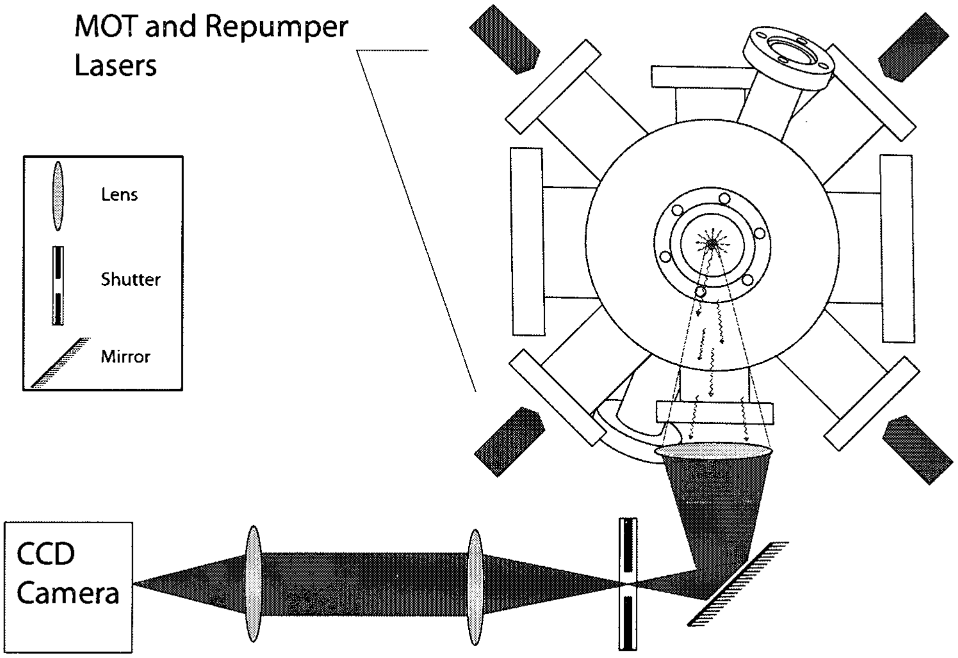

FIG. 32: Schematic of the fluorescence imaging system. Drawing is not to scale.

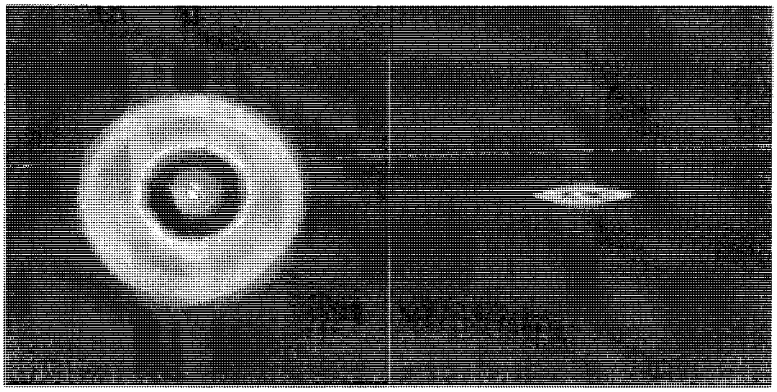

FIG. 33: Sample images of MOT and the QUEST obtained from fluorescence imaging.

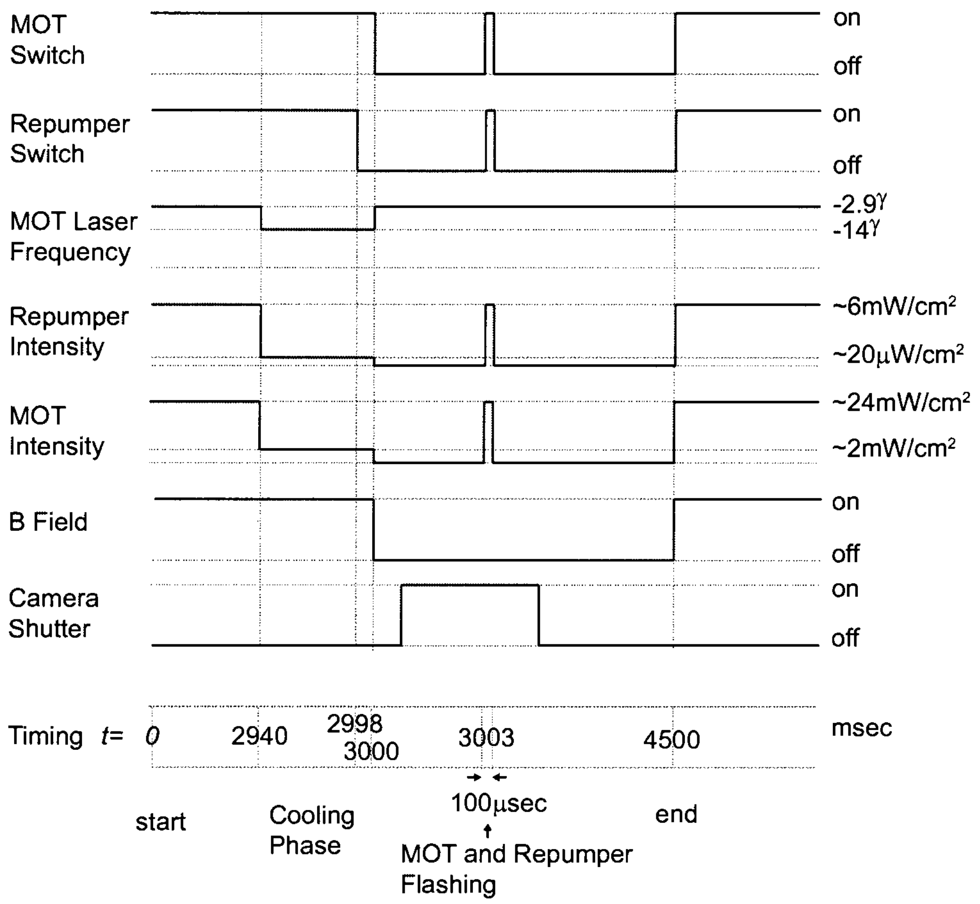

FIG. 34: Schematic of the timing for the fluorescent imaging of the MOT. Drawing is not to scale.

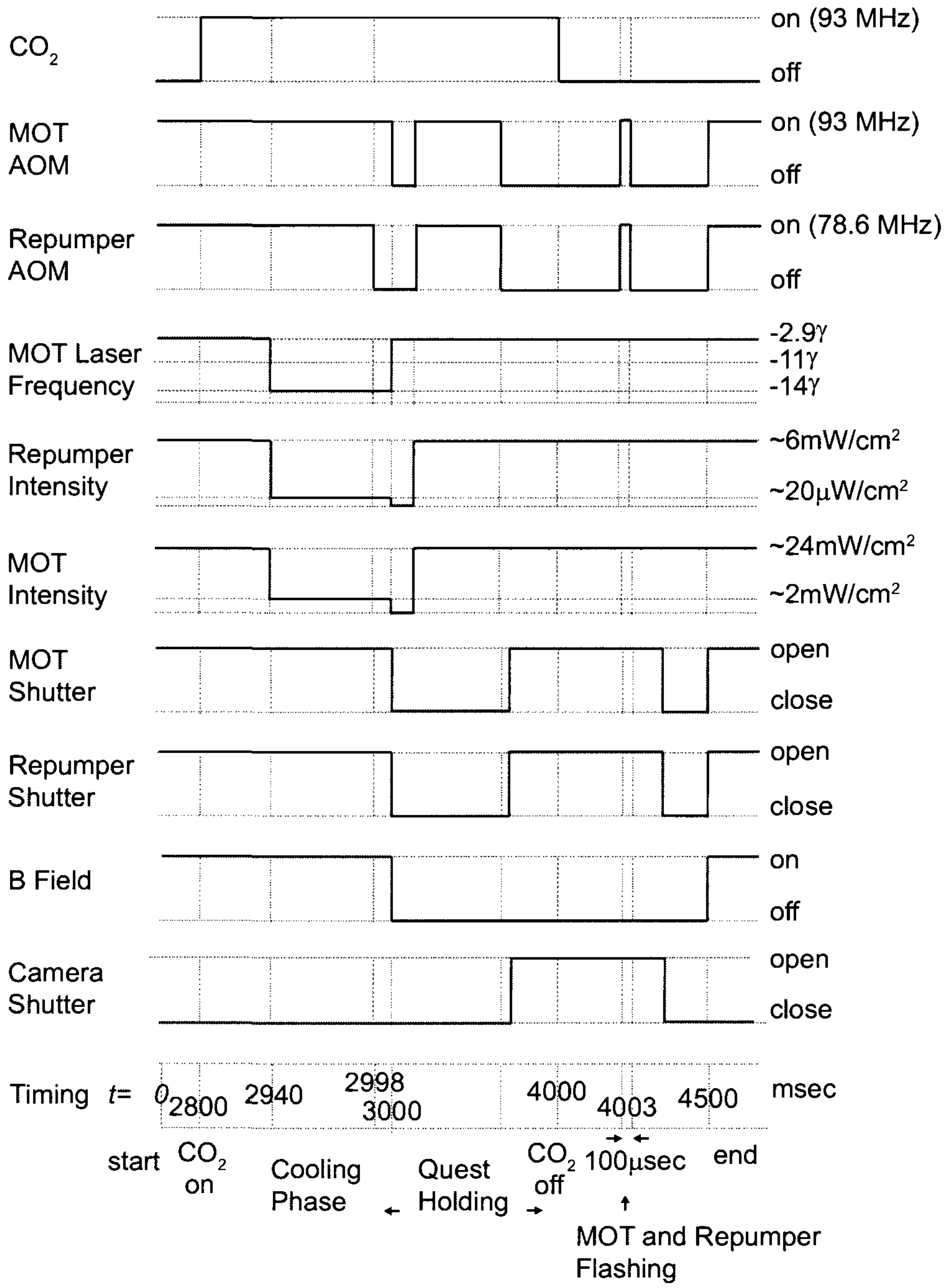

FIG. 35: Schematic of the timing for the fluorescent imaging of the QUEST. Drawing is not to scale.

and the repumper lasers for a short period of time (~ 100 to 400 μs) after some expansion time. For the MOT the minimum expansion time is 3 ms which is the time needed for the camera shutter to open. The camera shutter mentioned here is the shutter located at the focus of the collecting lens (Fig. 32). The CCD camera itself is equipped with a shutter that is opened 20 ms before the camera shutter and stays open for 50 ms overlapping the data acquisition period. The detuning of the MOT laser is fixed at -17.4 MHz (~ -2.9 γ) for the MOT and the QUEST fluorescence imaging. Fig. 33 shows two sample images of the MOT and the QUEST obtained via fluorescence imaging under similar conditions. A comparison of these two images gives a transfer efficiency of ~ 10 %.

Fig. 36 shows the absorption imaging setup. A probe laser that is tuned near resonance is incident on the MOT and the transmitted beam is imaged with the same imaging setup as in fluorescence imaging. The only difference is an iris is placed at the focus of the 75 mm lens to block the diffuse fluorescence photons going into the CCD; this light otherwise forms a background signal that is difficult to quantify. The atoms in the F = 2 ground state are illuminated with a linearly polarized 10 μs probe laser which is tuned off resonance enough such that the absorption signal is nearly a Gaussian and the peak is not flat and broadened due to the high optical depth. The intensity of the probe beam is adjusted to be much smaller than the saturation intensity, I_s, so as not to cause any power broadening and saturation. The signal to noise ratio is not an issue for these measurements as the absorption is quite large even after the 3 ms expansion of the MOT and the probe intensity is plenty for the camera even at $0.01 I_s$ and 10 μs pulse duration. A generalized form of Eq. 159 at the trap center is

$$b = \sqrt{2}\pi n_0 \sigma r_0 \tag{165}$$

where

$$\sigma = \frac{\sigma_0}{1 + (2\delta/\gamma)^2} \tag{166}$$

and the laser detuning δ from resonance, ω_0

$$\delta = \omega - \omega_0. \tag{167}$$

Similarly,

$$b = \frac{b_0}{1 + (2\delta/\gamma)^2}. \tag{168}$$

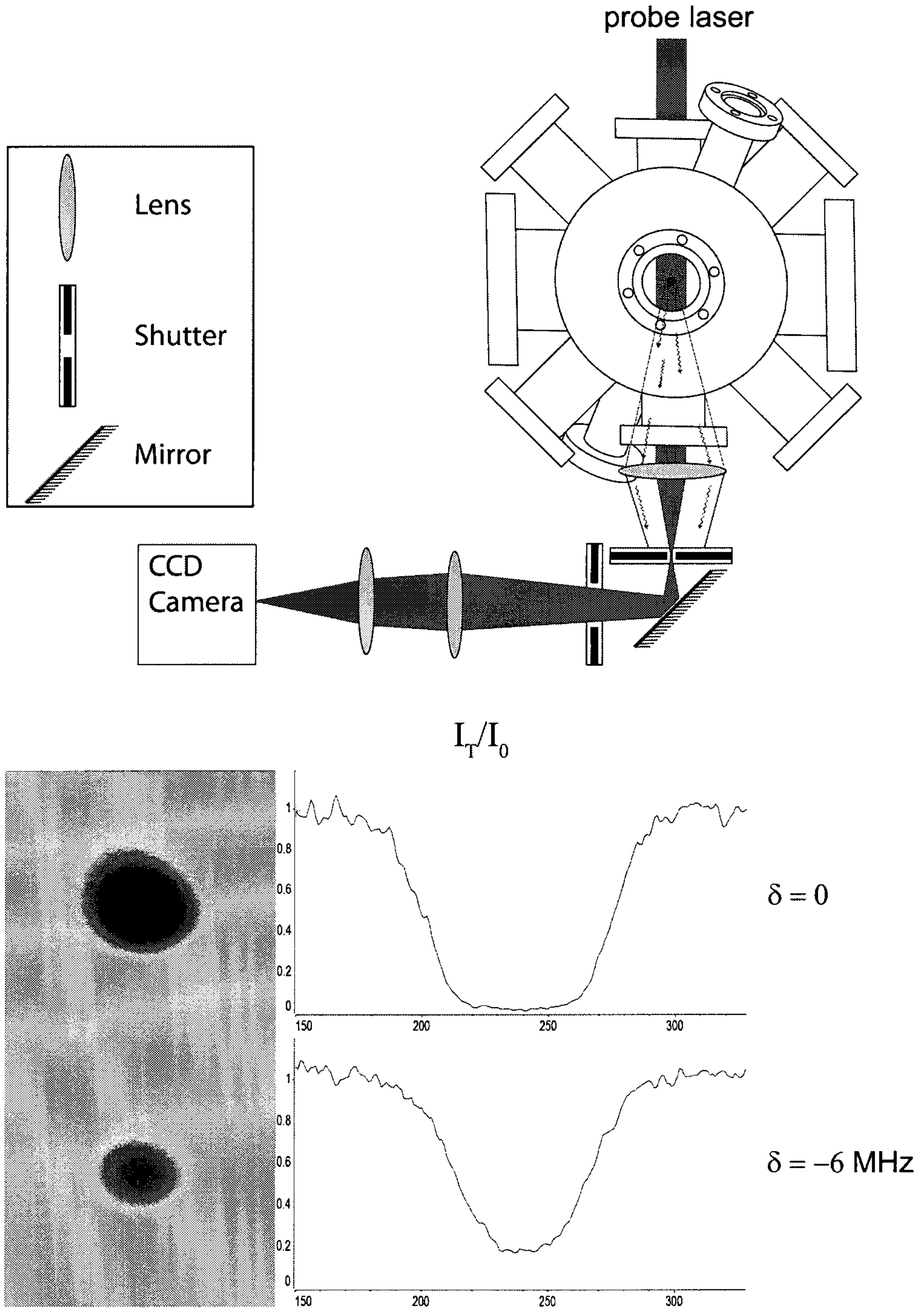

FIG. 36: Schematic of the absorption imaging setup. Drawing is not to scale.

From the absorption images as shown in Fig. 36, I_T/I_0 is obtained. From Eq. 168 and Eq. 158, the on resonance optical depth b_0 for the MOT is

$$b_0 = -(1 + (2\delta/\gamma)^2) \ln \frac{I_T}{I_0}. \tag{169}$$

So for a MOT with a Gaussian atom distribution of

$$n(r) = n_0 \mathrm{exp}(-\frac{r^2}{2r_0^2}) \tag{170}$$

a Gaussian fit of the line scan across the natural logarithm of the absorption image gives the radius r_0 of the MOT,

$$\ln \frac{I_T}{I_0} = b_0 \mathrm{exp}(-\frac{r^2}{2r_0^2}) \tag{171}$$

Once the Gaussian radius r_0 and the peak density n_0 (from Eq. 165) is calculated, the total number of atoms in the MOT is

$$N_{MOT} = n_0 (2\pi)^{3/2} r_0^3. \tag{172}$$

The total number of atoms in a typical MOT obtained in our lab is $\sim 10^8$ atoms with a Gaussian radius of ~ 400 μm after 3 ms expansion. The corresponding peak optical depth at 3 ms is ~ 10 and the peak density is 1.4×10^{11} atoms/cm^3. The corresponding total number of atoms in the QUEST is found to be $\sim 10^7$ with a 10% transfer efficiency.

IV.1.2 Parametric Resonance Measurement

Another important parameter to be determined before calculating the peak density of the QUEST is the shape of the trapping potential formed by the CO_2 laser. Measuring the spot size directly is not trivial as the intensity at the focus of the CO_2 laser is $\sim 10^6$ W/cm^2. An indirect measurement of the spot size comes from so called parametric resonance measurements.

The main heating mechanism in CO_2 laser dipole traps comes from the collisions with warm background gas, as the spontaneous scattering of photons due to CO_2 laser is minimal [63, 65, 66]. In addition to these heating mechanisms, heating due to intensity fluctuations and pointing stabilities can be significant in some systems [63]. Adams *et al.* [64] observed trap lifetimes of 0.8 s. in their Sodium atom trap, much lower than they expected. Previous research by the Thomas's group,

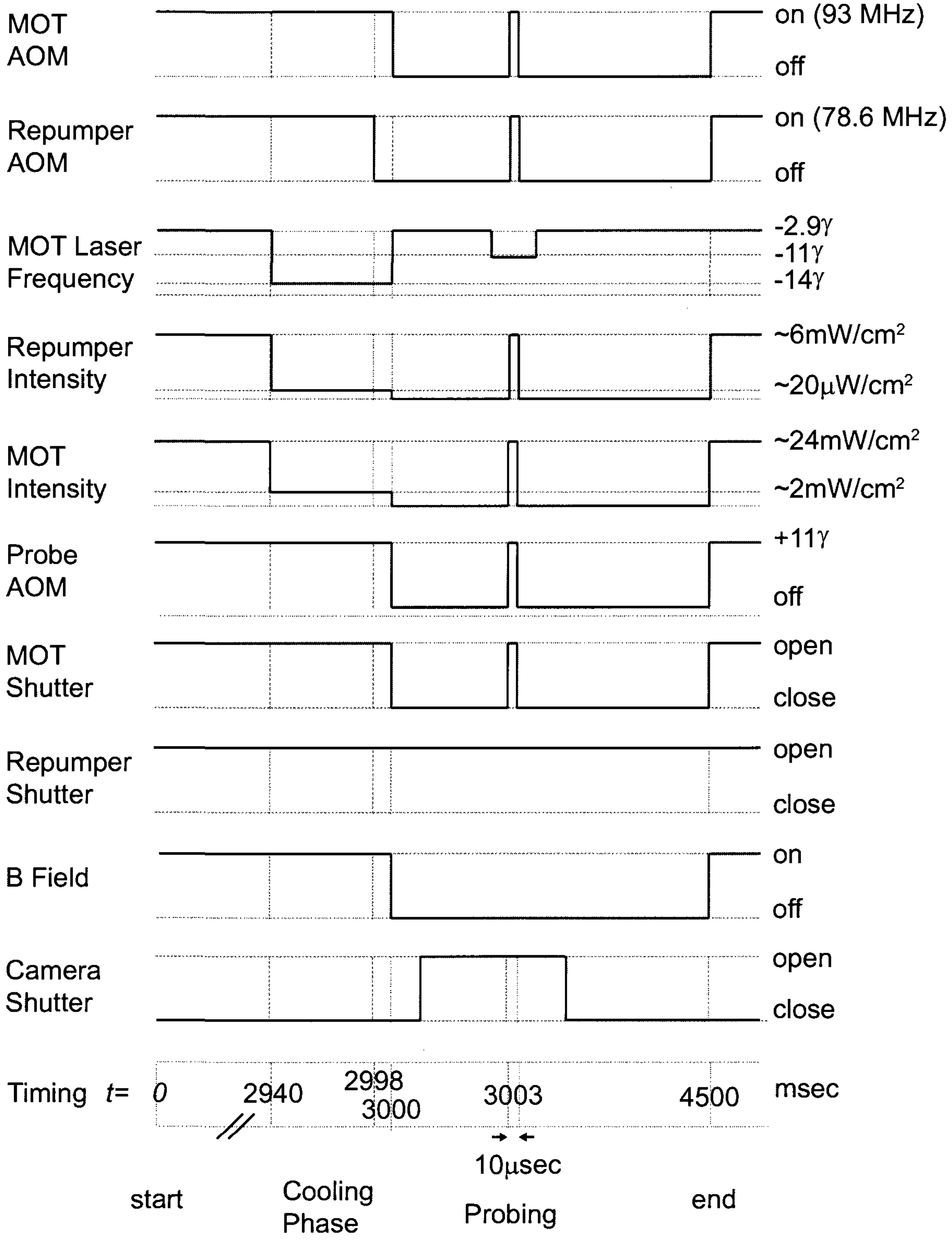

FIG. 37: Schematic of the timing for the absorption imaging of the MOT. Drawing is not to scale.

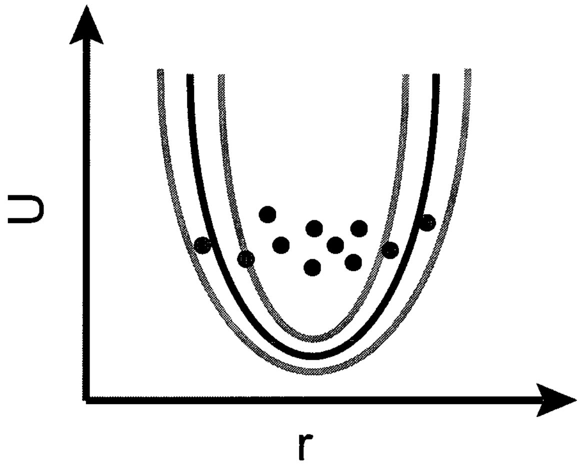

FIG. 38: Illustration shows the intensity fluctuations in the trap potential which leads to parametric heating of the sample.

at Duke University has shown that Coherent GEM Select laser has very low noise characteristics [67–69]. Our experiments confirm that result, as we did not observe any unusual heating or trap loss due to laser noise or pointing stabilities in our hold time measurements.

In addition to this unwanted feature, the heating due to intensity fluctuations can be employed as a useful tool in finding the harmonic oscillation frequencies of the trap. As it can be seen from Eq. 164, fluctuations in the laser potential will cause harmonic frequencies to change. Let us consider the case where the laser intensity is changed periodically with a modulation frequency of f_m as schematically illustrated in Fig. 38. Parametric heating occurs because the atoms are confined to a time varying potential well. As the atoms are heated, their mean energy increases. Further, since the trap has a finite depth they move higher in the potential well and eventually boil out of the trap. These instability regions where the sample interaction with the potential is larger are called parametric heating resonances. The strongest interaction happens when the trap oscillation frequency ω, is half the intensity modulation frequency, w_m where $w_m = 2\pi f_m$. Parametric resonances generally occur when $w_m = 2\,\omega/n$ where n = 1, 2, 3, ... [70].

Another way of to think about this process is by considering that the spring constant, k, of an harmonic oscillator depends on the potential. As the potential is periodically modulated with a modulation depth of h, the atoms in the trap will

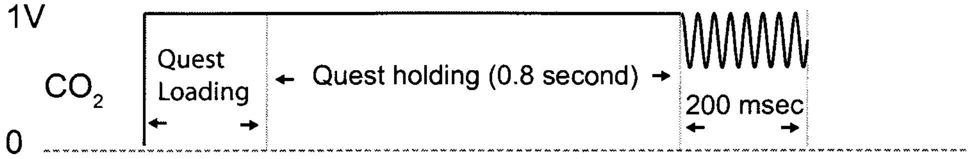

FIG. 39: Modified CO_2 laser control signal for parametric heating measurements.

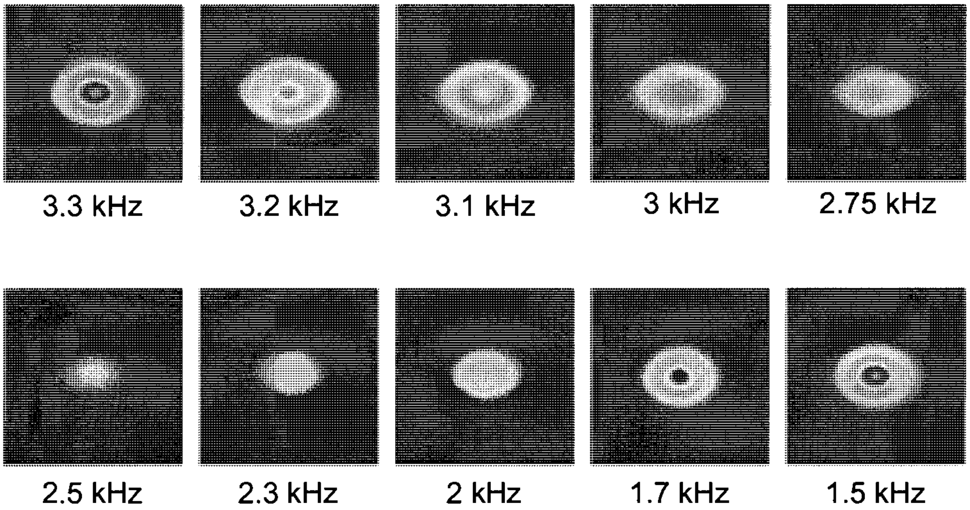
3.3 kHz
3.2 kHz
3.1 kHz
3 kHz
2.75 kHz
2.5 kHz
2.3 kHz
2 kHz
1.7 kHz
1.5 kHz

FIG. 40: Typical images of parametric heating measurement. The cloud is permitted to expand for 3 ms before imaging. The images clearly show the trap loss as the modulation frequency is swept across $\sim$ 2.5 kHz, twice the radial harmonic frequency of the trap.

experience a periodic force equal to hkx, where x is the atom's distance from the trap center. The modulation depth is defined in terms of intensity as

$$h(t) = h(t+D) = \frac{I(t) - I_0}{I_0} \tag{173}$$

where $I(t)$ is the peak intensity at time t, I_0 is the peak intensity and D is the period of the modulation. As the atoms heats up x will increase leading to exponential heating of the sample [63]. The parametric heating has been extensively studied by many groups [63, 65, 71–76].

The experimental setup and timing for the parametric resonance measurements is similar to the fluorescence imaging of the QUEST as shown in Fig. 32 and Fig. 35. The CO_2 laser is modulated for 200 ms at the end of the 1 second hold time of the QUEST. This modulation heats the sample as the modulation frequency is tuned through parametric resonances. Modulation is generated by modifying the CO_2 control signal as shown in Fig. 39 through changes in the rf power that drives the AOM. This modification makes the first order diffraction efficiency of the AOM oscillate, which causes in turn the intensity modulation at the focus of the CO_2 laser. At the end of the modulation time the CO_2 laser is turned off and the fluorescence images of the quest are taken after 3 ms of free expansion to allow for the trap to become optically thin. The fluorescence signal obtained were proportional to the total number of atoms in the QUEST. Typical images of the perimetrically heated and expanded cloud of atoms are shown in Fig. 40. The traditional method of analyzing these data is to measure the total intensity of light scattered from the sample. This measures the trap loss which is determined as the frequency of the modulation is tuned across the parametric resonances. In this method the modulation depth, h is chosen to be 0.15 to cause a loss of atoms that can easily be detected. Modulation depths of less than 0.10 do not heat up the sample enough in a 200 ms modulation time to cause measurable trap loss. In the second method, the peak intensity of the images are recorded. This is an indirect measurement of the cloud temperature change after parametric heating and also gives the loss of atoms localized spatially in the harmonic region of the trap. This is a more sensitive measurement than the one mentioned above. A comparison of both methods is shown in Fig. 42. In these graphs two different results from the same measurement are shown. In the first one, the total number of atoms remaining in the trap after parametric excitation is shown. In the other one, depletion of the atoms from the central part of the trap is shown. The difference between the two method is very obvious as the depletion method reveals the resonances clearly. In Fig. 42 (b) the axial parametric resonance measurement is shown. In this graph the total signal loss graph doesn't even show a resonance even for modulation depth of $h = 0.20$ (2) but the peak intensity signal clearly shows the resonance. This axial frequency result of $f_z = 105$ (5) Hz agrees with the radial frequency of $f_r = 2.6$ (1) kHz within the experimental uncertainty.

Once the harmonic oscillation frequencies of the trap are known, from

$$w_r = \sqrt{\frac{4U_0}{m\omega_0^2}} \qquad and \qquad w_z = \sqrt{\frac{2U_0}{mz_R^2}}. \tag{174}$$

the beam width ω_0 and the Rayleigh range z_R of the CO_2 laser can be calculated. In our experimental setup with 40 W total CO_2 power and measured value of radial oscillation frequency of $f_r = 2.6\ (1)$ kHz, the beam waist of $\omega_0 = 55\ (3)\ \mu$m and the Rayleigh range of $z_R = 0.96\ (0.05)$ mm is calculated.

IV.1.3 Temperature Measurement

In our experiments we are interested in achieving the highest possible density of atoms in the QUEST. According to Eq. 157, r_0, z_0 and the total number of atoms N is required to calculate the density of the QUEST. Knowing the exact shape of the Gaussian potential of the trap is not sufficient to calculate the Gaussian radii r_0 and z_0 of the QUEST. In a dipole trap with a potential $U(r,z)$, the thermal density distribution $n(r,z)$ is given by,

$$n(r,z) = n_0\, exp\left(-\frac{U(r,z)}{k_B T}\right) \tag{175}$$

where k_B is the Boltzmann's constant and T is the temperature of the atoms [55]. When combined with Eq. 163, and Eq. 156 the temperature of the trapped atom cloud is

$$T = \frac{m r_0^2 \omega_r^2}{k_B} \quad and \quad T = \frac{m z_0^2 \omega_z^2}{k_B} \tag{176}$$

from which r_0 and z_0 of the QUEST can easily be calculated.

The temperature of the atoms confined in the QUEST are measured via time of flight experiments. The experimental configuration is similar to the fluorescence imaging setup as described in section IV.1.1. The temperature of the QUEST is inferred from the velocity distribution of atoms in the QUEST. To measure the velocity distribution, the cloud of atoms is allowed to expand for different periods of time. The Gaussian radii, $r_0(t)$ and $z_0(t)$ of the cloud vary in time as

$$r_0(t) = \sqrt{r_0^2 + (vt)^2} \tag{177}$$

and

$$z_0(t) = \sqrt{z_0^2 + (vt)^2}. \tag{178}$$

Here $v^2 = k_B T/m$. Fig. 176 shows the images for up to 4 ms ballistic expansion of the QUEST. The measurements done on these images yield $r_0(t)$ and $z_0(t)$ of the cloud for different times. The results are plotted and fitted to Eq. 177 and 178 as shown in Fig. 43. The result of the temperature measurements depends on the experimental parameters especially the well depth, U_0 of the trap. As pointed out in [67] the expected thermal energy of the cloud, $k_B T$ to well depth ratio is $\sim 1/10$.

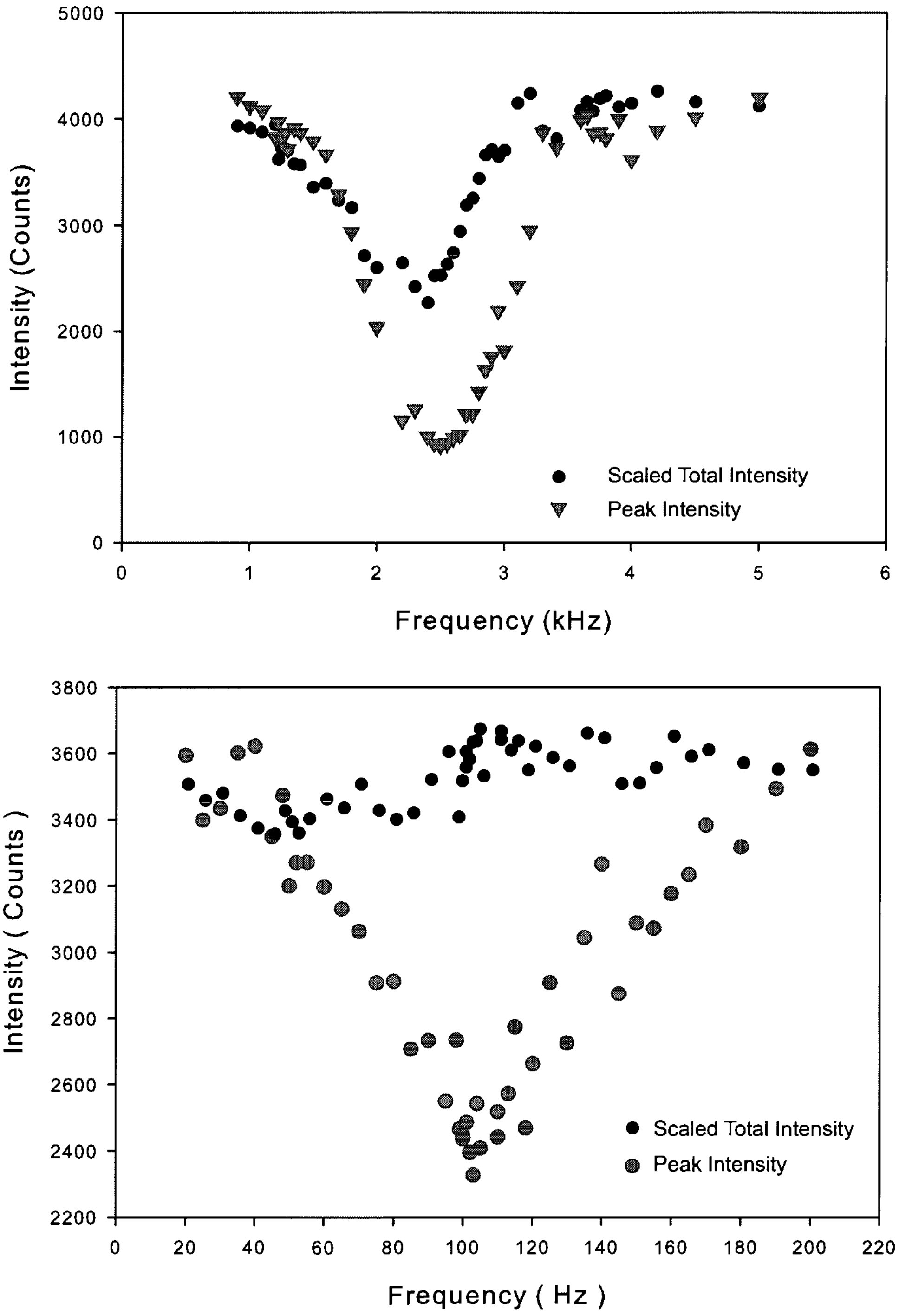

FIG. 41: (a) Fundamental radial parametric resonance for a modulation depth $h = 0.15$. (b) Fundamental axial parametric resonance for a modulation depth of $h = 0.20$.

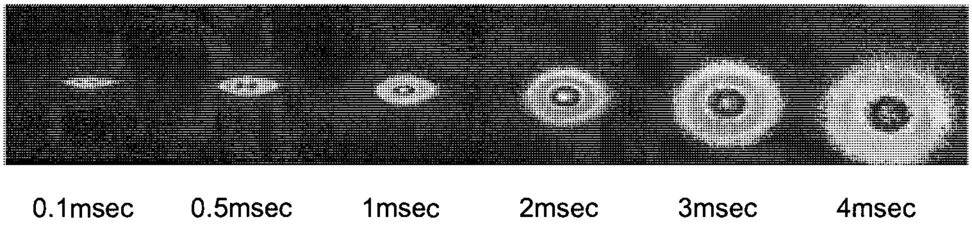

FIG. 42: Images of a ballistic expansion and free falling of the atomic cloud in time.

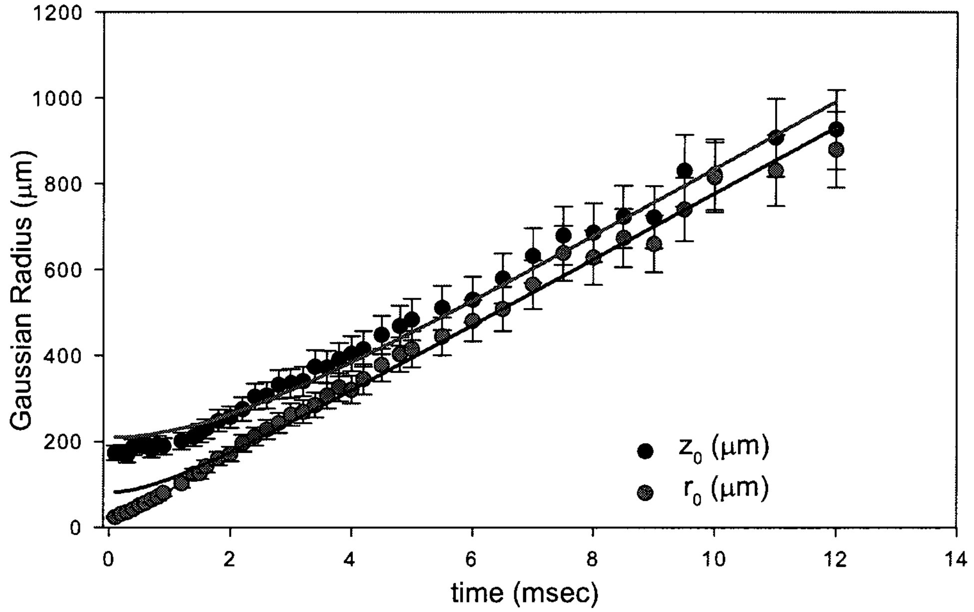

FIG. 43: Fitting the $r_0(t)$ and $z_0(t)$ to $r_0(t) = \sqrt{r_0^2 + (vt)^2}$ and $z_0(t) = \sqrt{z_0^2 + (vt)^2}$ gives velocity of the cloud $v = 77$ μm/ms and temperature of ~ 65 μK. CO_2 power used in this measurement is 50 W.

The smallest temperature measurement made is ~ 21 μK after forced evaporative cooling of 0.5 s. The temperature shown in Fig. 43 of ~ 65 μK is obtained with 50 W CO_2 power which corresponds to ~ 0.61 mK well depth.

CHAPTER V

RESULTS

As was mentioned before, the main goal of this research is to investigate light scattering near the localization regime. Light localization is expected to happen when the dimensionless quantity $k\ell \sim 1$. This dimensionless quantity is called Ioffe-Regel parameter. Here the mean free path is given by $\ell = 1/n\sigma$, where n is the atomic density and σ is the light scattering cross section. Thus the density n is the main parameter that determines, in our experiments, whether or not we are in the localization regime. Measurement of the density is critically important in order to accurately interpret the experimental results. In this chapter the MOT and the QUEST characteristics will be summarized. Derivation of the atomic density from experimental measurements will be described. The last section will cover experimental results of time dependent light scattering from the ^{87}Rb F = 2 → F′ = 3 transition.

V.1 MOT AND QUEST OVERVIEW

In calculating the atomic density distribution of the QUEST the MOT characteristics play an important role. The number of atoms in the QUEST is calculated from the efficiency of transfer from the MOT as obtained via fluorescent measurements. Table 1 and Table 2 lists typical characteristics of the MOT and the QUEST, respectively. Note that these numbers change within 10% from day to day due to variations of laser intensities, vacuum, temperature and other effects over which we have limited control. Some of these numbers are purposefully changed from time to time. For example after evaporative cooling, colder temperatures are achieved for different final CO_2 laser powers.

The values shown in Table 2 are for a maximum density QUEST right after the CO_2 laser is turned off. The MOT numbers in Table 1 are obtained after letting the MOT expand for 3 ms. This is the minimum time required before the MOT can be accurately imaged. The MOT characteristics before expansion can be calculated by using Eq. 177. The calculated values at $t = 0$ are: $r_0 \sim 400$ μm, $n_0 \sim 1.7\times10^{11}$ atoms/cm^3 and $b_0 \sim 12$.

Gaussian Radius, r_0	440 (40) μm
Peak Optical Depth, b_0	10 (1)
Peak Density, n_0	1.3 (0.2)$\times 10^{11}$ atoms/cm^3
Number of Atoms, N	1.7 (0.2)$\times 10^8$ atoms
Temperature, T	38 (4) μK

TABLE 1: These values are typical MOT characteristics after 3 ms of expansion.

CO_2 Laser Total Power	P	40 (2) W
CO_2 Laser Beam Waist	ω_0	55 (5) μm
CO_2 Laser Rayleigh Range	z_R	960 (50 μm
Potential Well Depth	U_0	11.8 (1) MHz 0.56 (0.05) mK 7.8 (0.8)$\times 10^{-27}$ Joules
Radial Parametric frequency	f_r ω_r	1.3 (0.1) kHz 8.2 (0.8) kHz
Axial Parametric frequency	f_z ω_z	54 (5) Hz 340 (30) Hz
Gaussian Radius	r_0 z_0	9.6 (0.5) μm 230 (20) μm
Transfer Efficiency		10 (1) %
Number of Atoms	N	1.7 (0.2)$\times 10^7$ atoms
Temperature	T	65 (8) μK
Peak Density	n_0	3.3 (0.3)$\times 10^{13}$ atoms/cm^3
Peak Optical Depth	b_{0r} b_{0z}	165 (20) 3900 (500)
Ioffe-Regel Parameter	$k\ell$	1.2 (0.1)
mean free path	ℓ	0.15 (0.02) μm
$n(\lambda/2\pi)^3$		0.1 (0.01)

TABLE 2: Typical QUEST characteristics.

V.2 ATOMIC DENSITY

This section of the thesis is dedicated to calculation of the density of the atomic sample by using various experimental parameters that are obtained via fluorescence and absorption images, parametric resonance measurements and temperature measurements. As described in the previous chapters, temperature T, parametric resonance frequencies ω_r and ω_z, CO_2 laser power P, and number of atoms in the QUEST N, from Table. 2 are known through such measurements. The peak density of the QUEST, n_0 is given by

$$n_0 = \frac{N}{(2\pi)^{3/2} r_0^2 z_0} \tag{179}$$

The first step in the calculation of density is to find the well depth of the potential formed by the CO_2 laser beam. The potential well depth is given by

$$U_0 = \frac{1}{2\epsilon_0 c} \alpha_{stat} I_0, \tag{180}$$

where α_{stat} is the static polarizibility of the ground state of Rb, c is the speed of light, and I_0 is the peak intensity of the laser beam at the focus and is given by,

$$I_0 = \frac{2P}{\pi \omega_0^2}, \tag{181}$$

where ω_0 is the beam waist of the CO_2 laser at the focus. Combining Eqs. 180 and 181 yields

$$U_0 = \frac{\alpha_{stat} P}{\pi \epsilon_0 c \omega_0^2}. \tag{182}$$

This equation is not enough by itself to find the well depth as ω_0 is not known. But we know the parametric resonance frequencies, and by using Eqs. 164 and 182 we obtain

$$\omega_0 = \sqrt[4]{\frac{4\alpha_{stat} P}{\pi \epsilon_0 c m \omega_r^2}}, \tag{183}$$

where m is the atomic mass. Once ω_0 is calculated, the potential well depth can easily be calculated from Eq. 182. A simplified version of Eq. 182 obtained by substituting fundamental constants and α_{stat} is

$$U_0 = \frac{960}{\omega_0^2} P. \tag{184}$$

The result is in units of MHz when ω_0 is in units of μm. By using 21 MHz = 1 mK the well depth in units of mK is obtained.

The last piece in calculation of the density is finding the Gaussian radii, r_0 and z_0 of the QUEST which can easily be calculated from Eq. 176. During the ballistic expansion of the QUEST the r_0 and z_0 changes according to Eqs. 177 and 178. As a result peak density of the QUEST varies during the expansion according to

$$n_0(t) = \frac{N}{(2\pi)^{3/2}(r_0^2 + (vt)^2)\sqrt{z_0^2 + (vt)^2}} \tag{185}$$

where v, the speed of the atoms is given by,

$$v = \sqrt{\frac{k_B T}{m}} \tag{186}$$

At this point the QUEST is fully characterized: The relevant quantities related to the light scattering experiments are given in Table 2. Some fundamental constants and some characteristic data of ^{87}Rb used in these calculations are given in Ref. [43].

V.3 F = 2 → F′ = 3 RESULTS

V.3.1 Introduction

The main goal of this dissertation research is to investigate light scattering from high density and ultracold atomic ^{87}Rb gas and look for experimental signatures of Anderson localization of light. The measurements discussed in this chapter include transient hyperfine optical pumping processes, and light scattering of near resonance probe radiation on the F = 2 → F′ = 3 transition. The physics is explored in time domain experiments. Atomic density, probe detuning and intensity dependence of the signals are also explored in detail in the coming sections.

Different possible probing schemes were explained in Section III.3.3 and illustrated in Fig. 17. Among those probing schemes the smallest Ioffe-Regel parameter, $k\ell = 1/n_0\sigma_0$ and highest peak optical depth b_0 is obtained in probing with a laser tuned on resonance with the F = 2 → F′ = 3 transition. Here σ_0 is the on resonant light scattering cross section that defines both parameters along with the density. Since the density is optimized, the biggest chance to see localization effects is on the F = 2 → F′ = 3 transition. The light scattering cross section σ_0 is given by

$$\sigma_0 = \frac{(2F'+1)}{(2F+1)}\frac{\lambda^2}{2\pi}, \tag{187}$$

which equals

$$\sigma_0 = \frac{7}{5}\left(\frac{\lambda^2}{2\pi}\right) \tag{188}$$

for the F = 2 → F′ = 3 transition. Moreover previous light scattering experimental results in a dilute medium (MOT) from F = 1 → F′ = 0 transition indicates that the optical pumping of atoms to m = ±1 Zeeman levels of the F = 1 ground state greatly decreases the possibility of seeing localization on that transition [77].

V.3.2 Experimental Setup

General experimental instrumentation and sample formation has been mainly described in the previous chapters. This section of the results will explain the specific protocol for the light scattering experiments. A schematic drawing for the experimental setup related this chapter is shown in Fig. 44.

After the QUEST is prepared and characterized, the experiments are carried out in different timing and probing configurations depending on the purpose of the experiment. A sample timing used in these experiments is shown in Fig. 45. The durations or delays with respect to CO_2 laser turn off time of the probe and the repumper laser is varied for different data taking protocols as explained in the coming sections. All the results covered in this chapter deal with time dependent fluorescence data obtained from the QUEST and analysis. The fluorescence collection setup is shown in Fig. 44. The fluorescence emerging from the sample is collected by a f = 150 mm focal length, achromatic lens placed at 1 f away from the sample. A second lens, with 75 mm focal length, focuses the fluorescence into a 600 μm diameter multimode fiber. The net magnification of the setup is 1/2 which makes the image of the QUEST approximately 20 μm × 230 μm in size at the fiber tip. The fiber tip is much bigger than the sample size, preventing signal loss during the expansion of the QUEST. This is experimentally tested by moving the fiber around a few hundred μm, from which no significant fiber response change is observed. The fiber is mounted on a xyz translater to maximize coupling into the fiber. The other end of the fiber is attached to a Photomultiplier Tube (PMT) made by Product for Research Incorporated (Part number C311034/0076/0588, 16437-89). The tube is installed inside a refrigerated housing (Refrigerated Chamber, part number TE210RF) to minimize dark counts. The voltage supplied to the tube is kept at -1500 V for all the experiments. To condition the photon pulses for counting, the output of the PMT is amplified 125 times by a fast preamplifier (Stanford Research Systems, part number SR445A). The amplifier has a 350 MHz bandwith with a 1 ns fall/rise time. The output of of the amplifier is connected to a multichannel scaler (Stanford Research Systems,

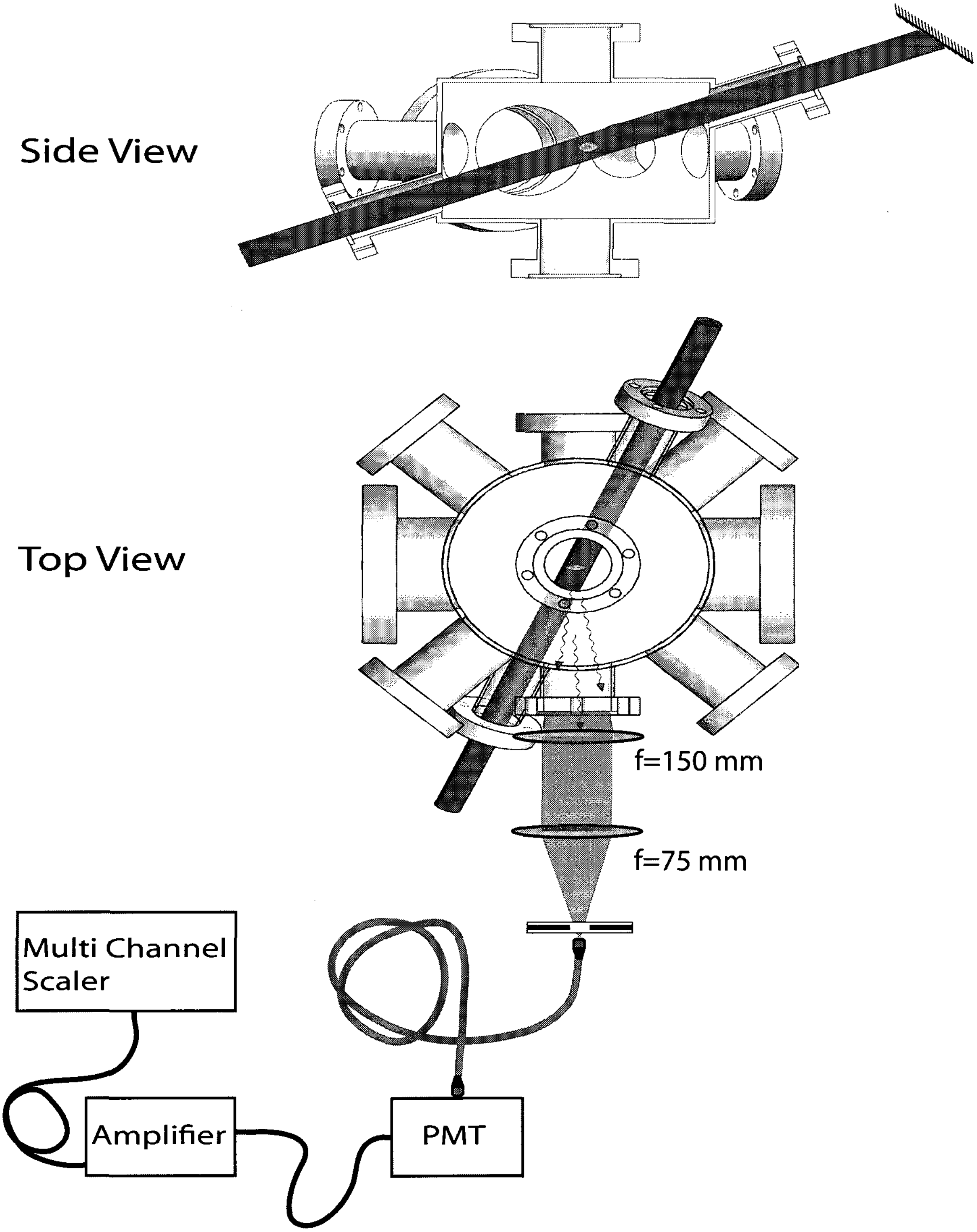

FIG. 44: Schematic of experimental setup for light scattering experiments.

part number SR430). The Multichannel Scaler (MCS) can be thought of as a photon counter that counts the incoming current from the PMT as a function of time. The MCS is capable of sorting the data in bins with a width from 5 ns to 10 ms. The MCS has up to 32000 sequential bins per record allowing a 160 μs window for data accumulation for the smallest bin width of 5 ns. The multichannel scaler has a built in discriminating feature that allows us to keep the background at very low levels. The data explained in this chapter is accumulated in 5 ns bins unless otherwise noted. The multichannel scaler is also triggered and kept synchronized with the experiment by the master clock as explained in the previous chapters, see Fig. 45.

V.3.3 Hyperfine Optical Pumping

Even though MOT cooling occurs at the $\mathrm{F} = 2 \rightarrow \mathrm{F}' = 3$ transition and atoms leaking to the $\mathrm{F} = 1$ ground state are pumped back to the $\mathrm{F} = 2$ transition by a repumper laser, we have to minimize hyperfine collision losses by transferring the atoms by optically pumping to the $\mathrm{F} = 1$ ground state during QUEST loading [78]. This is accomplished by turning off the repumper laser 1.5 ms before the MOT lasers turned off. In order to probe the $\mathrm{F} = 2 \rightarrow \mathrm{F}' = 3$ transition the atoms must be optically pumped back to the $\mathrm{F} = 2$ hyperfine ground state. This is done by using the the repumper laser which is tuned on resonance with the $\mathrm{F} = 1 \rightarrow \mathrm{F}' = 2$ transition as shown in Fig. 46.

As it was described in the previous section, the density of the QUEST is varied by letting the QUEST expand. The final peak density of the cloud is estimated from Eq. 185. Table 3 shows the estimated peak density n_0, radial and axial Gaussian radii of the QUEST r_0 and z_0, the on resonance transverse optical depth b_t of the QUEST after different expansion times. The value of b_t given is calculated for a laser beam tuned on resonance with the $\mathrm{F} = 2 \rightarrow \mathrm{F}' = 3$ transition. The hyperfine optical pumping data in Fig. 47 shows the data taken at these points.

Data taking time for each density point is about 2 hours. It is important to note that for this kind of long data taking, background signal due to dark current is around a few counts per bin. The signal that is seen especially in the fast decaying lower density data after optical pumping process completed is due to the hot atom fluorescence from the repumper laser that is incident on the sample from all six directions. The repumper laser beam has about 2 cm^2 area with 8 mW total power at the trap center.

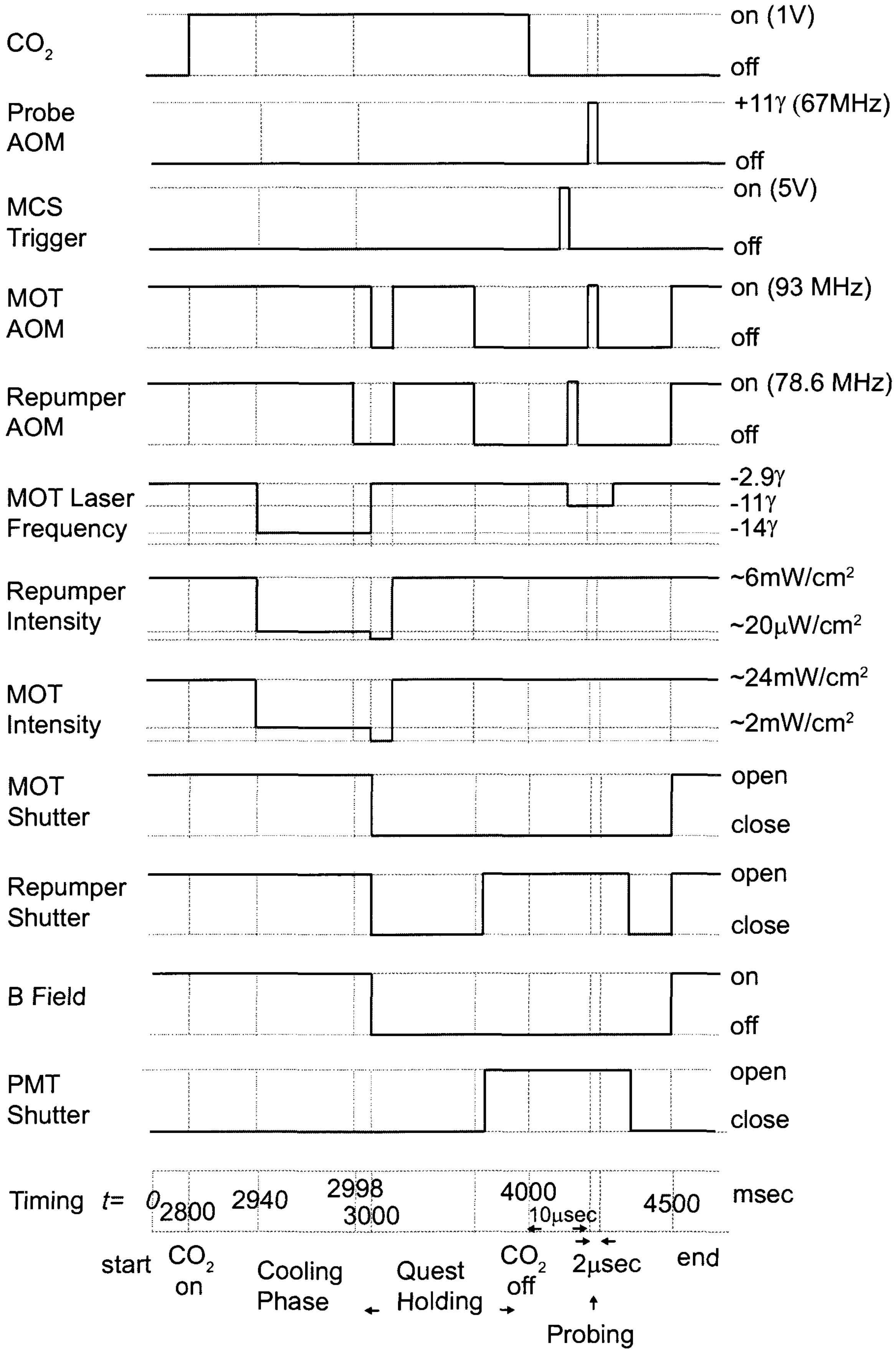

FIG. 45: Figure is showing a sample timing used in the light scattering experiments.

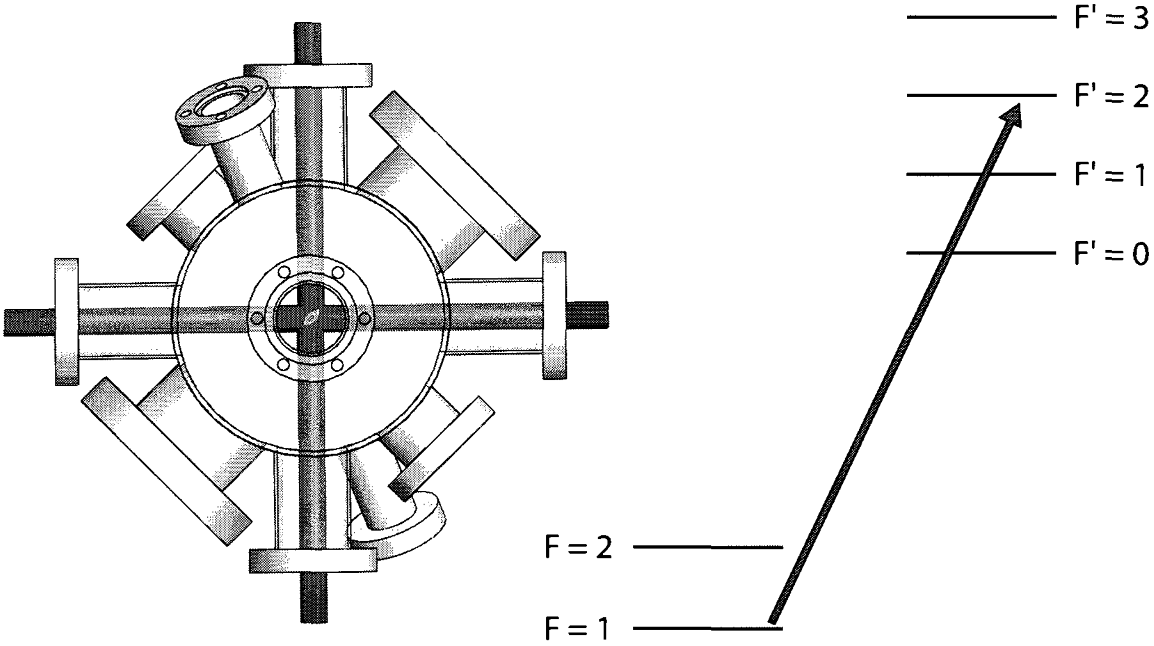

FIG. 46: Diagram of hyperfine optical pumping process: The repumper laser incident on the sample from all 6 directions (vertical directions not shown) is tuned on resonance with the F = 1 → F′ = 2 transition. The resulting optical pumping process transfers atoms from the F = 1 to the F = 2 ground state hyperfine component.

Peak b_t	n_o (atoms/cm^3)	r_o (μm)	z_o (μm)
165	5.0×10^{13}	9.8	248
117	2.5×10^{13}	13.8	248
82	1.2×10^{13}	19.5	248
53	5.1×10^{12}	30.4	249
16	5.2×10^{11}	92.3	264
5	5.9×10^{10}	240	345

TABLE 3: QUEST parameters relating the peak transverse optical depth on the F = 2 → F′ = 3 transition to the peak sample density and the Gaussian radii of the atomic cloud.

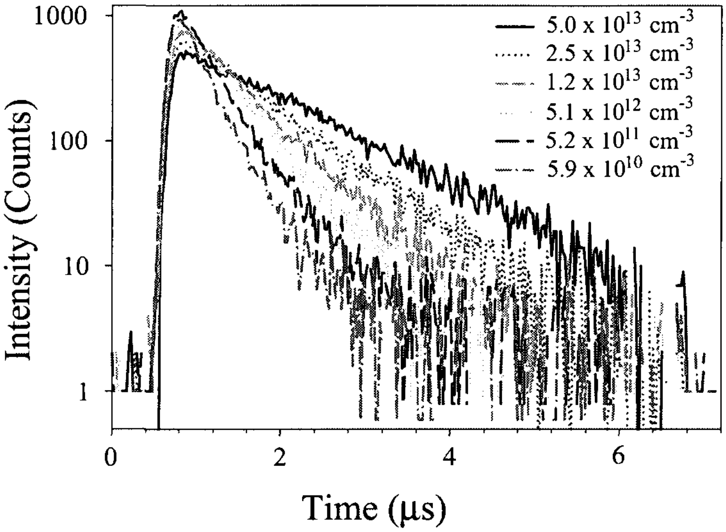

FIG. 47: Time evolution of the F = 1 → F′ = 2 optical pumping signal. The values shown represents the peak density of the sample for the corresponding data.

Another point that is immediately realized from the data is that the optical pumping signal decays nearly exponentially. The higher density data decays much more slowly as expected. The decay rate is well approximated by a single exponential. This decay rate can be estimated by considering that the repumper laser saturates the F = 1 → F′ = 2 transition. The time associated with pumping an atom from the F = 1 ground state to the F = 2 ground state is approximately $2\tau_0$, where $\tau_0 =$ 26 ns is the radiative lifetime of the excited state. When considered the probability that an atom ends up in F = 2 in this process is 5/8, we estimate that the repumper laser penetrates a distance of one mean free path ℓ into the sample in ~ 80 ns. From Table 2 for the highest density data, for $\ell \sim 0.15\ \mu$m and $r_0 \sim 10\ \mu$m, it takes about 60 scattering events for repumper laser to reach the middle of the QUEST. So this estimation gives complete optical pumping decay time of ~ 5 μs which is in good qualitative agreement with the data shown in Fig. 47. The decay rate analysis of this data is shown in Fig. 48b where we see that the exponential decay rate of the optical pumping signal depends approximately exponentially on the transverse optical depth b_t (peak optical depth in radial direction of the QUEST).

Fig. 48a shows the peak repumper intensity signal dependence as a function of b_t. The peak intensity is the maximum intensity that the signal reaches right after the

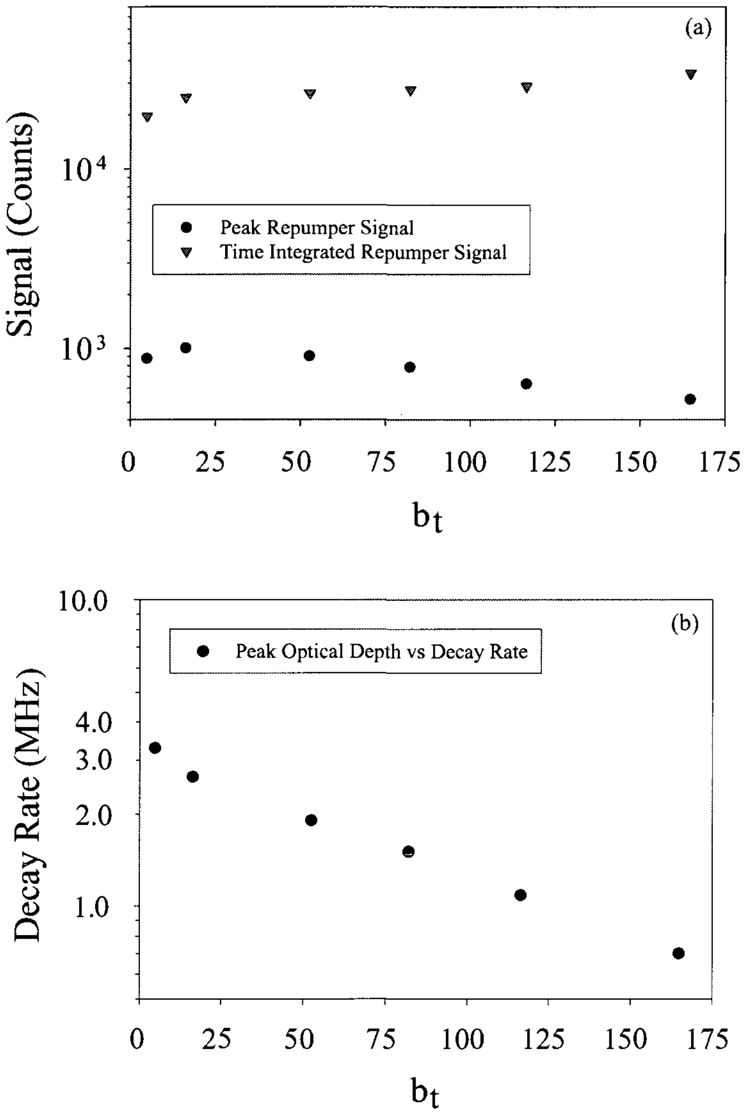

FIG. 48: Analysis of the data shown in Fig. 47. The values extracted are plotted as a function of transverse optical depth, b_t. Variations in the (a) integrated and peak scattering signals, and (b) decay rate of the repumper transients.

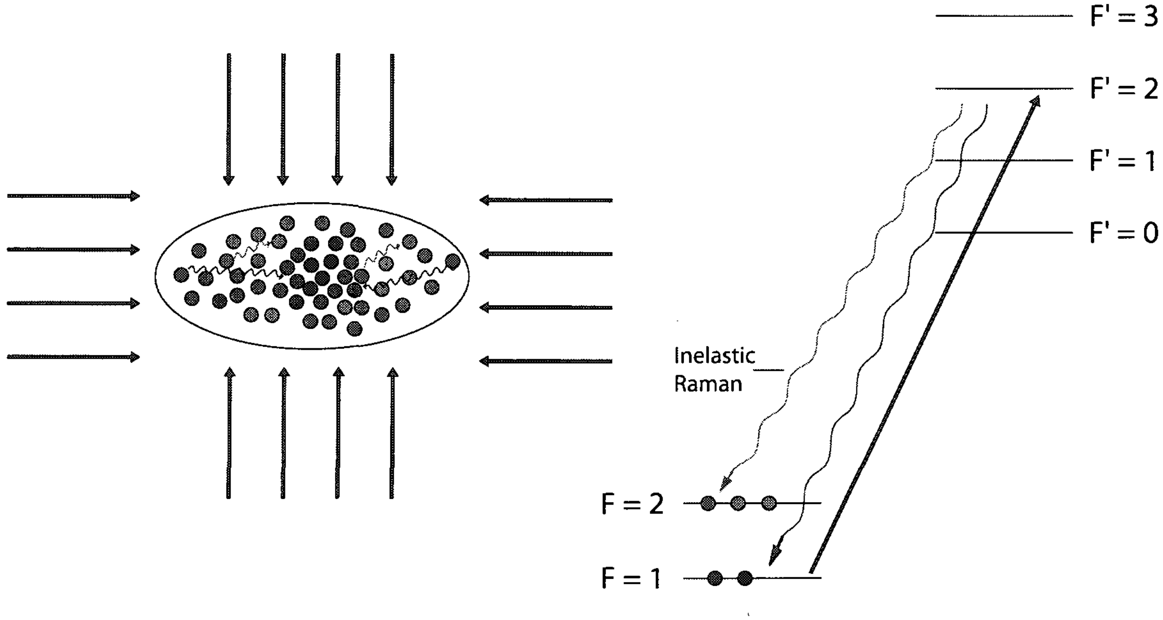

FIG. 49: Schematic of hyperfine optical pumping process. Figure shows possible Rayleigh and inelastic Raman scatterings during the hyperfine repumping process and the mixture of the atoms from the F =1 to the F=2 ground state hyperfine component.

repumper laser is turned on. This figure also shows the integrated signal versus peak optical depth b_t. In both cases the signal doesn't seem to strongly depend on the density and the variations are within the experimental uncertainty. The relatively small increase of the peak signal as the density is decreased can be attributed to the sample becoming optically thin and the repumper laser penetrating deeper into the sample initially and reaching more atoms. The drop in the total signal as the peak transverse optical depth b_t gets smaller is due to the decrease in the coupling of the repumper fluorescence into the fiber. For the very optically thin sample the size of the expanded cloud becomes comparable to the fiber tip diameter.

In all of these analysis, the effect of the inelastic Raman scattering (the diffuse photons from $F' = 2 \rightarrow F = 2$ decay) and the effect of multiple scattering are ignored. The actual processes that take place are more complicated than it is described here. Fig. 49 shows a schematic of the optical pumping process before it is completed and depicts the complexity of the system.

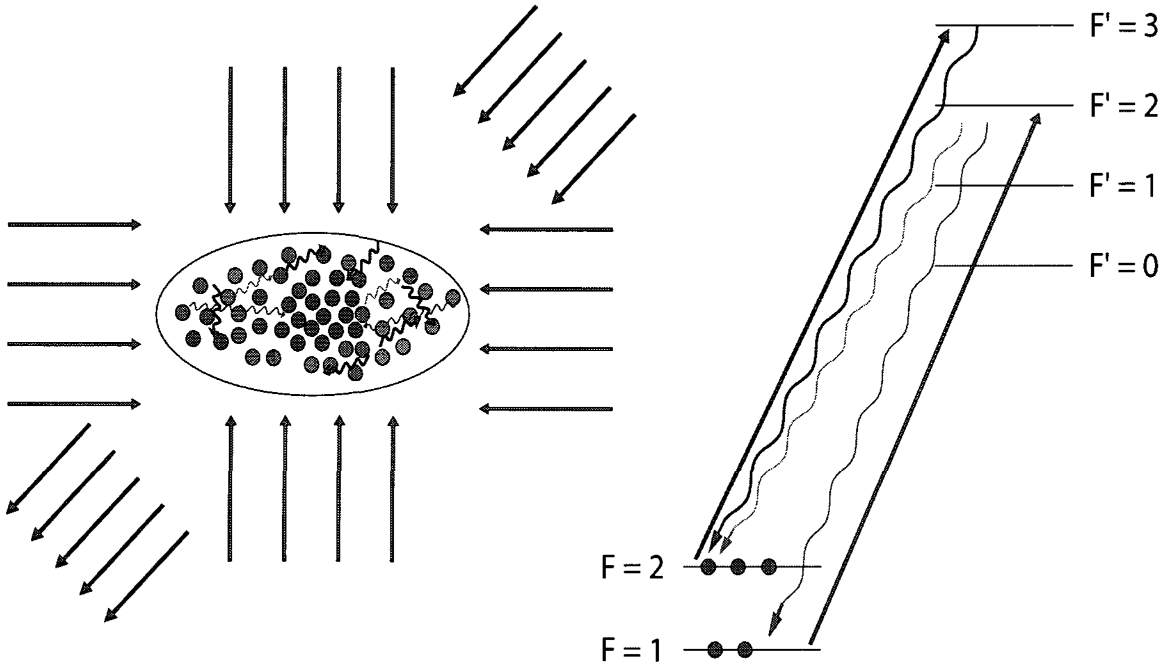

FIG. 50: Schematic of probe and repumper laser incident on the QUEST at the same time. Mixture of F = 1 and F = 2 ground state atoms and scattering of photons near resonance with the F = 2 → F′ = 3, F = 1 → F′ = 2, F′ = 2 → F = 2 transitions are depicted.

V.3.4 Combined Hyperfine Optical Pumping and Light Scattering on the F = 2 → F′ = 3 Transition

One big issue in light scattering from high optical depth samples is the difficulty of penetrating deep into the sample where the density is the highest and there is a better chance of generating localized modes. To overcome this problem different techniques have been applied. One is these is overlapping the probe laser that is tuned near resonance with the F = 2 → F′ = 3 transition with the repumper laser tuned on resonance with the F = 1 → F′ = 2 transition as shown in Fig. 50. The repumper laser configuration is as described as in the previous section. The probe laser is incident on the sample as shown in Fig. 44.

In these measurements the probe laser is tuned on resonance with the F = 2 → F′ = 3 transition and the probe intensity is varied while keeping the repumper intensity fixed. Results are shown in Fig. 51. The maximum density of the sample is 5×10^{13} atoms/cm^3. As it was shown in the previous section, the optical pumping process is completed in $\sim$ 5 μs, where the highest density region of the sample is

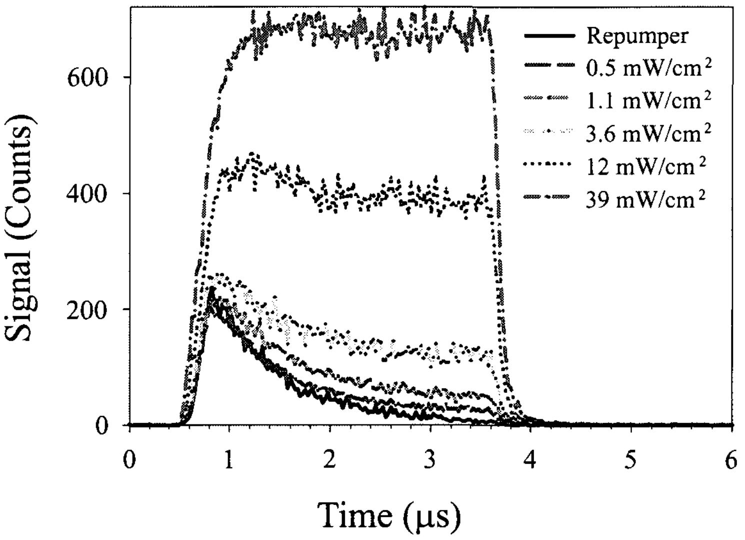

FIG. 51: Probe intensity dependence of the combined hyperfine repumper laser and the probe laser tuned on resonance with the F = 2 → F′ = 3 transition.

optically pumped last. We see from Fig. 51 that the results strongly depend on the probe intensity. For the lower intensity data, the results look similar to the repumper laser only data that was discussed in the previous section. As the probe intensity is increased the signals reach a steady state value. The sample is initially optically thin for the probe laser and optically thick for the repumper laser. These roles are switched as the time dependent signal evolves.

The analysis of the steady state part of the data is presented in Fig. 52. Even though the saturation intensity for the F = 2 → F′ = 3 transition is ~ 1.7 mW/cm^2, the data shows a linear increase in the signal up to 12 mW/cm^2 probe laser intensity. This could be because of the decrease in the probe laser intensity as the probe penetrates into the optically thick sample. Most of the atoms are deep inside the sample and when probe radiation reaches those atoms, the coherent beam intensity becomes significantly less than the saturation value.

When we measure the intensity of fluorescence light after the probe and the repumper lasers are turned off simultaneously we do not see any signature of effective loading of photons into the highest density region of the QUEST. The reason for this would be that the optical pumping is a slow process and starts from the outer edges of the sample. By the time the repumper reaches the sample center, the probe is

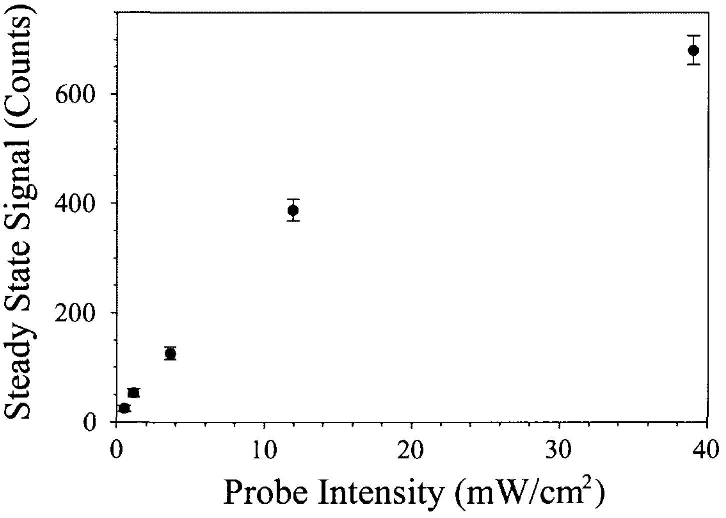

FIG. 52: Steady state signals extracted from the data of Fig. 51 are plotted as a function of F = 2 → F′ = 3 probe laser intensity. The saturation intensity for the F = 2 → F′ = 3 probe laser is $\sim$ 1.7 mW/cm^2.

already optically blocked by the outer shell of the QUEST. A better way of loading excitations into the middle of the sample is needed.

As it was mentioned at the end of the previous section, an already complex systems became even more complex by the optical dynamics in this type of experiment. This complexity can be seen in Fig. 50. As the repumper laser optically pumps the atoms to the F = 2 ground state the outer region of the sample is becoming optically thick not only for the F = 2 → F′ = 3 probe but also for the diffuse photons coming from the F′ = 2 → F = 2 Raman decay. Quantitative models are needed to describe these systems.

V.3.5 Probe Light Scattering on the F = 2 → F′ = 3 Transition

Density Dependence

To understand light scattering dynamics at high atomic density, we need to look at the case where the optical pumping process is finished before the F = 2 → F′ = 3 probe laser is incident on the sample. In this case the probe laser is turned on 1 μs after all the atoms are optically pumped to the F = 2 ground state. The density of the sample is varied as described in section V.3.3. Here, the probe intensity of 630

μW/cm^2 is weak compared to the saturation intensity. The probe laser has a 20 dB turn on/off time of ~ 100 ns. Fig. 53 shows the density dependence of such data. In this figure we can see that the fluorescence reaches a steady state level quickly and there is a temporal decay of the signal that lasts several hundred nanoseconds after the probe laser is turned off.

The total integrated signal data is analyzed as a function of atomic density in Fig. 55. Instead of the density we parametrize the dependence in terms of the transverse optical depth b_t. Recall that the sample has ellipsoidal Gaussian density distribution. So naturally the sample has two optical depths associated with the axial and radial dimensions. We call the radial optical depth the transverse optical depth b_t, and the axial optical depth as the longitudinal optical depth b_l. The relation between the density and the optical depth is given by

$$b_t = \sqrt{2\pi} n_0 \sigma_0 r_0 \tag{189}$$

and

$$b_l = \sqrt{2\pi} n_0 \sigma_0 z_0, \tag{190}$$

where n_0 is the peak density, r_0 and z_0 are the Gaussian radii of the ellipsoidal sample and σ_0 is the weak field resonant light scattering cross section. σ_0 is given by

$$\sigma_0 = \frac{(2F'+1)}{(2F+1)} \frac{\lambda^2}{2\pi}. \tag{191}$$

As we can see from Fig. 55 the total integrated signal increases as the transverse optical depth b_t is decreasing. This data can be understood when we consider that the sample is very optically thick and the probe beam intensity is greatly reduced by absorption at the surface and hardly any of the coherent beam reaches the central region of the sample for the highest density data. As the density is reduced the probe reaches more atoms deep inside the sample and the signal increases. This also explains the almost constant decay rate of the signal after the probe is turned off for the higher density data shown in Fig. 53. This could be due to the fact that as the optical depth decreases, the penetration ratio increases keeping the total number of multiple scattering rate constant.

To more quantitatively understand these results we consider a simple model of light scattering from a sample with a Gaussian atom distribution that is illuminated by a uniform intensity probe beam, see Fig. 54. For on resonant incident probe beam

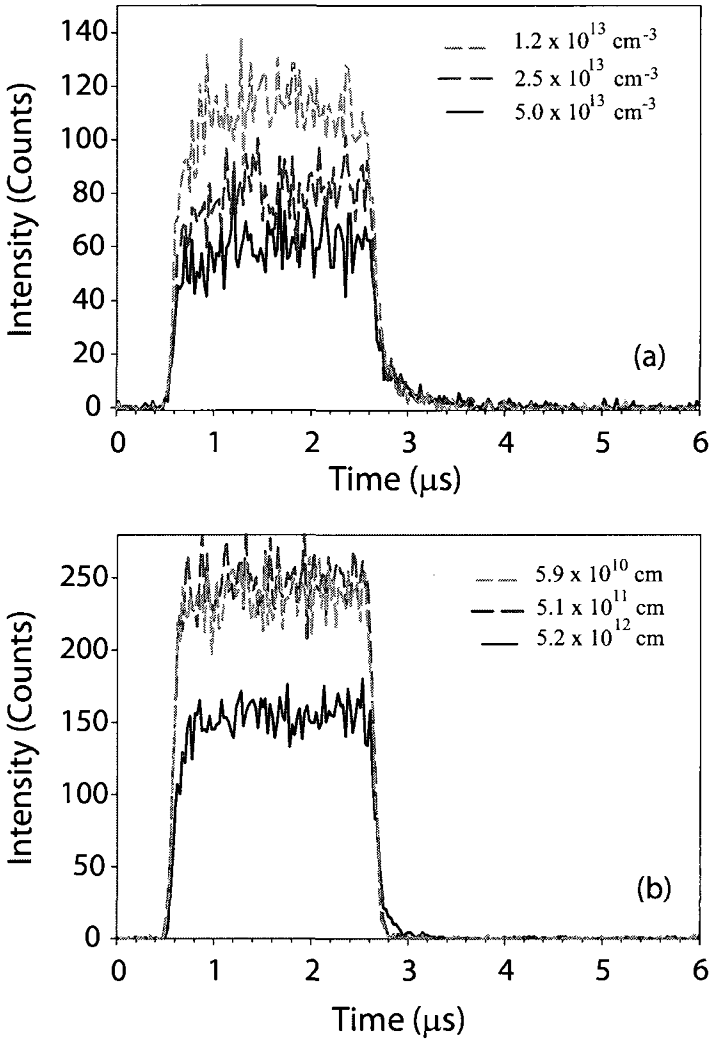

FIG. 53: Variations of the F = 2 → F′ = 3 resonant probe response with density and time. The steady state intensity of the fluorescence decreases with increasing density. (a) Fluorescence from higher densities. (b) Fluorescence from lower intensities.

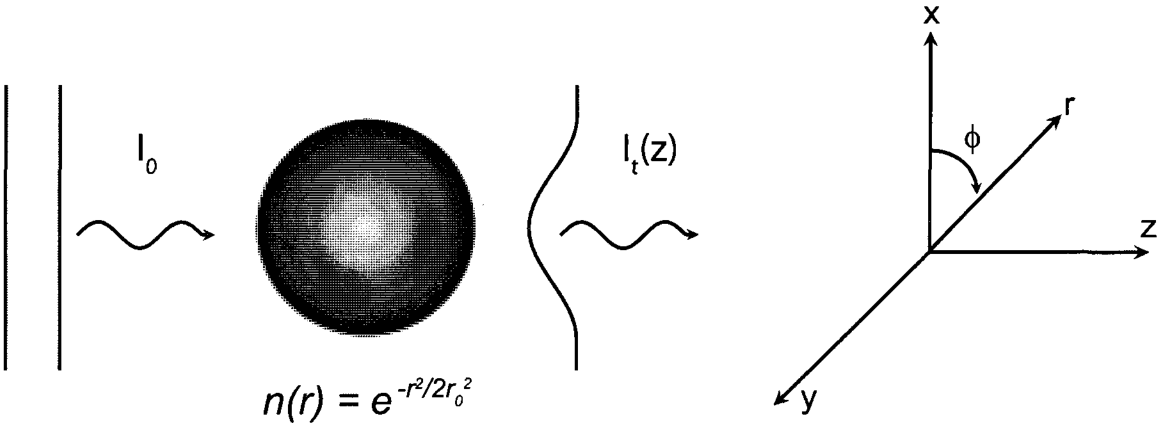

FIG. 54: A simple heuristic model of light scattering from a sample with Gaussian atom distribution that is illuminated by a uniform intensity plane wave.

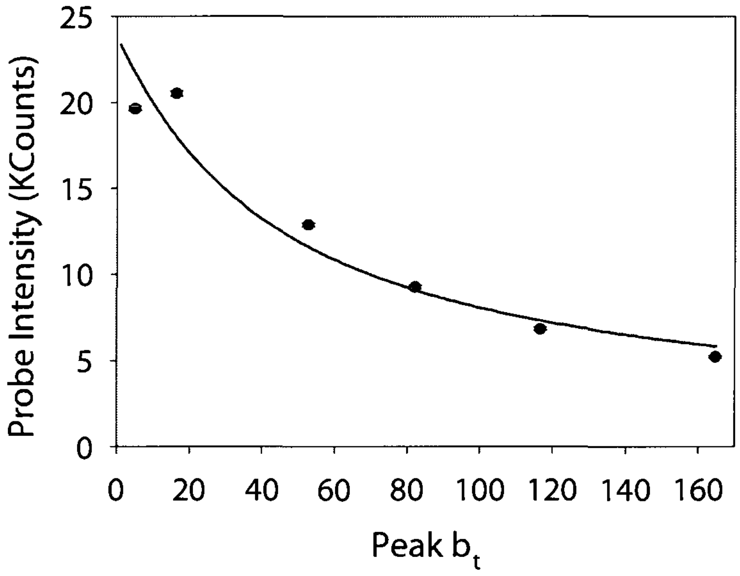

FIG. 55: Variations of the integrated signal with peak transverse optical depth as extracted from Fig. 53. The signal drops with increasing optical depth.

with initial intensity I_0, the transmitted intensity I(r)is given by

$$I(r) = I_0 e^{\left(-b_0\, e^{\left(-r^2/2r_0^2\right)}\right)}, \tag{192}$$

as shown in section IV.1.1. Here b_0 is the peak optical depth of the Gaussian sample and b_0 is given by

$$b_0 = \sqrt{2\pi} n_0 \sigma_0 r_0, \tag{193}$$

where n_0 is the peak density, σ_0 is the on resonant light scattering cross section and r_0 is the Gaussian radius of the atomic cloud. The total scattered light intensity, total scattered power P_s, is given by

$$P_s = \int\int (I_0 - I(r)) r dr d\phi. \tag{194}$$

Substituting Eq. 192 in Eq. 194 yields

$$P_s = \int\int I_0 \left[1 - e^{\left(-b_0\, e^{\left(-r^2/2r_0^2\right)}\right)}\right] r dr d\phi. \tag{195}$$

If we define $x = r^2/2r_0^2$, P_s becomes

$$P_s = \int 2\pi I_0 r_0^2 \left[1 - e^{\left(-b_0\, e^{-x}\right)}\right] dx d\phi. \tag{196}$$

To solve this integral if we expand the exponential around 0 we get

$$\begin{aligned} 1 - e^{\left(-b_0\, e^{-x}\right)} &= 1 - \sum_{n=0}^{\infty} \frac{(-b_0 e^{-x})^n}{n!} \\ &= 1 - \sum_{n=0}^{\infty} \frac{(-1)^n b_0^n e^{-nx}}{n!} \\ &= \sum_{n=1}^{\infty} \frac{(-1)^{n+1} b_0^n e^{-nx}}{n!}. \end{aligned} \tag{197}$$

By using

$$\int_0^{\infty} e^{-nx} dx = \frac{1}{n} \tag{198}$$

we reach a general form for the scattered power $P_s(b)$

$$P_s(b) = A \sum_{n=1}^{\infty} (-1)^{n+1} \frac{(\eta b)^n}{n n!}. \tag{199}$$

Here A is number proportional to $2\pi I_0 r_0^2$ and b_0 is replaced by b to include spectral variations of the incident beam. Here we also make the assumption that η

is an empirical scaling parameter for the optical depth that describes the effective nonuniform spatial density distribution of the QUEST and the limited penetration of the probe laser into the atomic sample. This heuristic model describes the density dependent data shown in Fig. 55 well with η = 0.08 (2) and A = 25 (2) Kcounts. The small value of η agrees with our previous explanations of the data as the probe beam does not significantly penetrate the sample. The solid curve shown in Fig. 55 is the fit of the Eq. 199 of $P_s(b)$ to the data. Here also note that lower density data points needs correction because of the decrease in the coupling of the fluorescence into the fiber as it was mentioned before.

Note that even though this model predicts the effective conditions very well, this model is for a Gaussian atom distribution. It does not take into account the ellipsoidal Gaussian nature of the QUEST. This model also does not take the angular distribution of the scattered intensity into account.

Detuning Dependence

Fig. 56 shows the data taken under similar conditions as the density dependent data. The repumper and the probe timing is same but now the detuning δ of the probe laser from the F = 2 → F′ = 3 transition is varied in the range ±24 MHz, while keeping the density at the highest value. As it can be seen in the figure a temporal behavior similar to the density dependent data is seen, as the signal rapidly reaches a steady state level. After the probe laser is turned off the signal decays for almost 1 μs. In the analysis of this data, and similar to density dependent analysis, we extract at the total integrated signal. Fig. 57 shows this data as a function of detuning δ. The response is approximately spectrally symmetric and has a full width at half maximum (FWHM) of ~ 24 MHz. The natural linewidth of the F = 2 → F′ = 3 transition is ~ 6 MHz. This type of broadening is expected because of the high optical depth of the sample.

Now we go back to our heuristic model developed in the density dependent section to analyze the detuning dependent data. This time the density is fixed and the optical depth varies by changing the detuning as

$$b(\delta) = \frac{b_0}{1 + (\frac{2(\delta - \Delta)}{\gamma'})} \tag{200}$$

where b_0 is the on resonance optical depth and Δ is the small shift of about 0.8 MHz

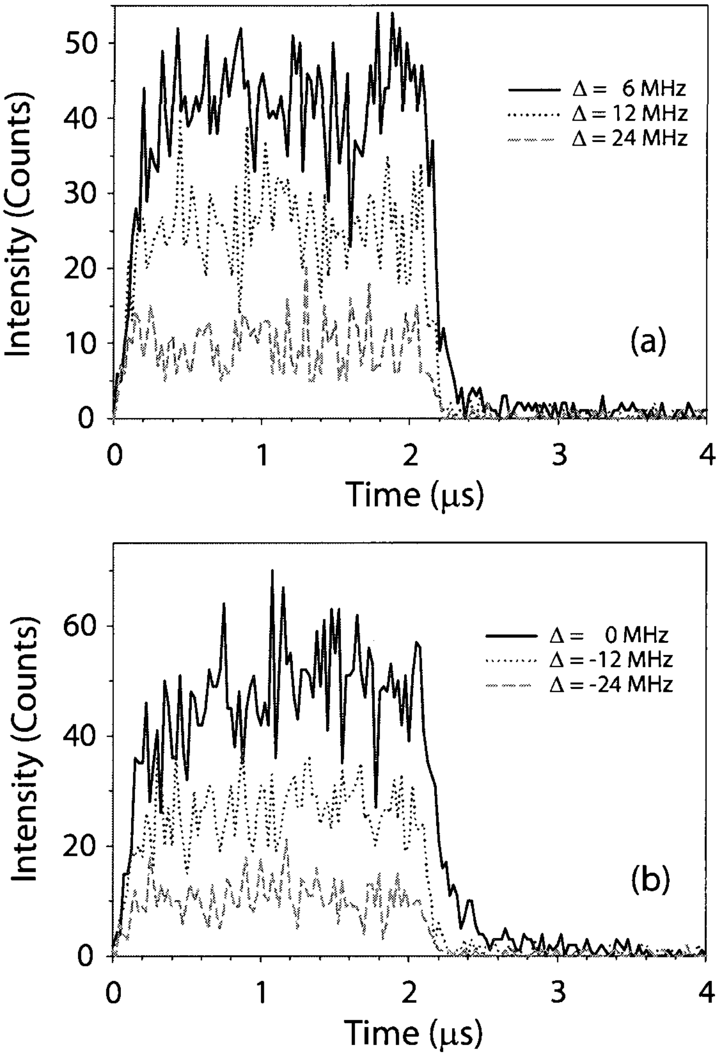

FIG. 56: Representative spectral variations of the transient light scattering response associated with the F = 2 → F′ = 3 probe transition. Positive (higher frequency) detunings are shown in (a), while negative (lower frequency) detunings are shown in (b). The peak optical depth b_t is kept at its maximum value of 165.

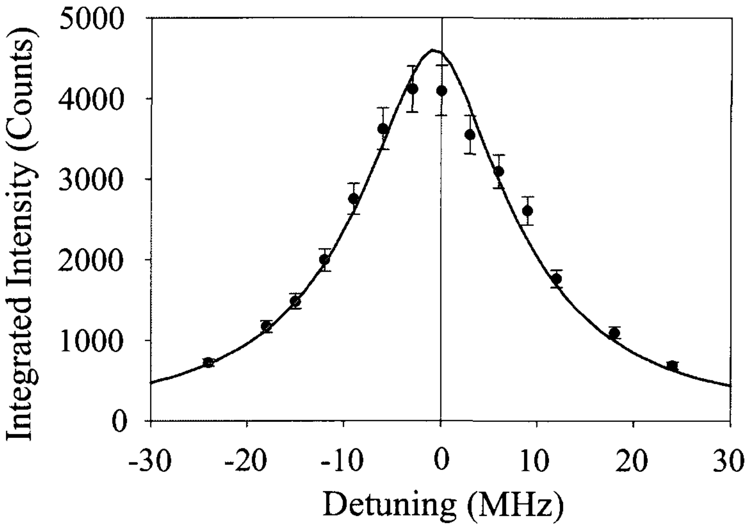

FIG. 57: Spectral variation of the temporally-integrated scattered light intensity on the F = 2 → F′ = 3 transition.

seen in the fit of the data seen in Fig. 57. This shift could be the Lorentz-Lorenz (local field) shift but this requires further measurements at higher densities and with a spectrally narrower probe laser. The probe laser used in these light scattering experiments has a spectral width of about 3 MHz. The smaller width mentioned in section III.3.3 is measured after fixing a problem with the current controllers that caused the widening of the spectral width of the lasers. Again the agreement between the data and this heuristic model with η = 0.10 (1) and Δ = 0.8 MHz is quite satisfactory.

Extended Run

We close this section by presenting in Fig. 58 data from an extended run of the experiment of about 10 hours. The probe duration in this case is 5 μs. The probe laser is on resonance with the F = 2 → F′ = 3 transition. The density is at its highest value of 5×10^{13} atoms/cm^3 and the transverse optical depth b_t is 165. The probe is directed toward the sample after the optical pumping process is completed, as explained in the previous sections. Both the repumper and the probe signal is shown in Fig. 58a. In Fig. 58b we see that there is a significant long time decay after the probe laser is extinguished. As it seen in the figure the decaying signals extends up to 2 μs. A double exponential fit (dashed line) to this decay signal gives 100 (10) ns and 500 (50) ns time constants. For a sample with a peak optical depth of 165, a diffusive model predicts a 40 μs decay time constant τ given Labeyrie *et al.*,

$$\tau = \frac{3b_0^2}{5.35\pi^2}\tau_0 \tag{201}$$

where $\tau_0 \sim 26$ ns is the natural decay time of the excited state [79]. This equation is for a spherically symmetric Gaussian atomic cloud. Again we attribute this difference to limited penetration of the sample. If we replace b in Eq. 201 with $\eta b_t = 16.5$, this equation predicts a decay time of 420 ns. The result is in reasonable agreement with the measured value of $\sim$ 500 ns in Fig. 58.

It is important to note here that heating due to probe laser or multiple scattering of photons in the medium and effects of frequency redistribution due to multiple scattering is considered negligible. But these effects also lead to a shortened decay time of the signal and these effects could be significant for high optical depth samples.

V.3.6 Enhanced Light Penetration by Light Shift Control

In the previous sections the main explanation of the observations was limited penetration of the probe into the higher density regions of the QUEST because of the high optical depth. As it was explained in Section III.3.4, by using a separate laser it is possible to transiently decrease the transverse optical depth b_t from 165 to 3.5. The experimental setup is similar to the other experiments explained in this chapter. The only difference is now the probe laser is overlapped with the light shift laser and focused to the center of the trap as shown in Fig. 59a. An advantage of this scheme, in addition to decreasing the optical depth, is that the fluorescence detected is directly coming from the highest density region of the sample. As these experiments are still continuing and more detailed studies of light localization using light shift laser is underway, we present only preliminary results here.

One difficulty in this experiment is the alignment of the probe laser and the light shift laser beams to the center of the QUEST. As it can be seen from the pictures in Fig. 59b and 59c the probe and light shift laser are aligned properly. In Fig. 59b the probe laser power is increased so that the atoms are being pushed by the laser. As it can be seen from the picture the laser only pushes the atoms in the middle not effecting the atoms in the outer regions of the sample. Fig. 59c shows the amount of

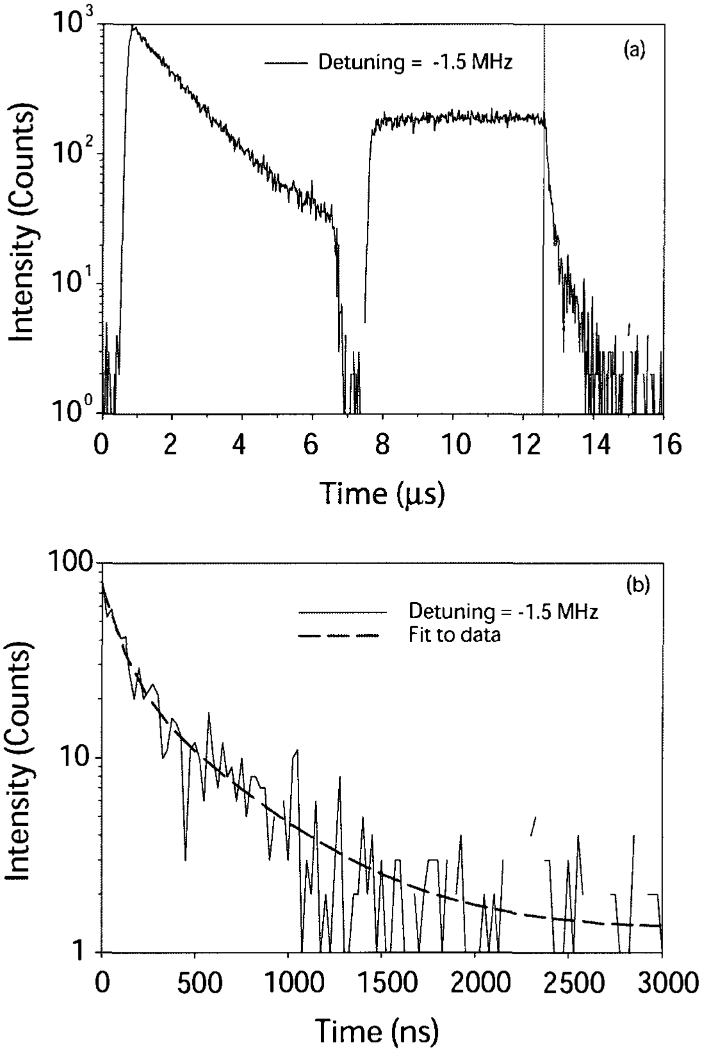

FIG. 58: Result of an extended experimental run of ~ 10 hours. The probe is tuned on resonance with the $F = 2 \to F' = 3$ transition. In this data the probe is turned on ~ 1 μs after the repumping laser is turned off. Both the repumping and the probe signals are shown in part (a). The vertical line represents when the probe beam is turned off. In part (b) we expand the scales to show the long-time transient after the probe beam is turned off. The time scale here starts from where the probe beam is turned off.

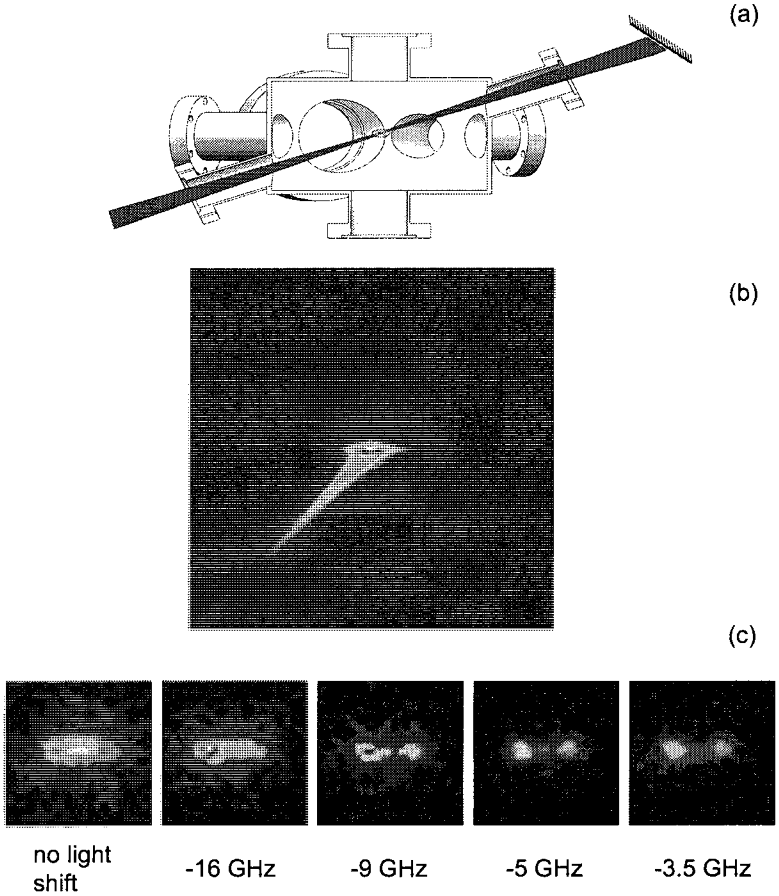

no light shift

-16 GHz

-9 GHz

-5 GHz

-3.5 GHz

FIG. 59: Schematic of light scattering experiment with light shift laser. (a) Probe and the light shift laser are overlapped and focused to the center of the QUEST. (b) The alignment of the probe beam is observed in this image. (c) The effect of the light shift with detunings of -16 GHz, -9 GHz, -5 GHz, -3.5 GHz from resonance when the probe and the light shift lasers are overlapped.

light shift for different light shift laser detuning. As expected the probe fluorescence emitted from the central part of the sample is decreasing with decreasing detuning.

The preliminary results of quantitative time resolved measurements are presented in Fig. 60. In Fig. 60a the the first signal is from the hyperfine optical repumping process. The second one is from the probe and the light shift overlap and the third one is from the light shift laser only. The third pulse is applied for two purposes. First, the size of the signal determines the amount of fluorescence in the second pulse that is from the light shift laser. Second, if there are photons loaded into the optically deep sample during the loading process (around t = 8 μs) that remain trapped at t = 14 μs, they will be simultaneously released at that time. The light shift detuning used in this experiment is -10 (1) GHz. The long tail of fluorescence decay after the probe and the light shift lasers are turned off extends almost up to 2 μs. But more importantly there is a suggestive rise in the fluorescence that starts around 2 μs after the probe is turned off and lasts up to the light shift second pulse. This is what would be expected for the time emergent intensity from the central zone of the sample. To quantify this effect more systematically, more detailed experiments need to be done and they are in progress.

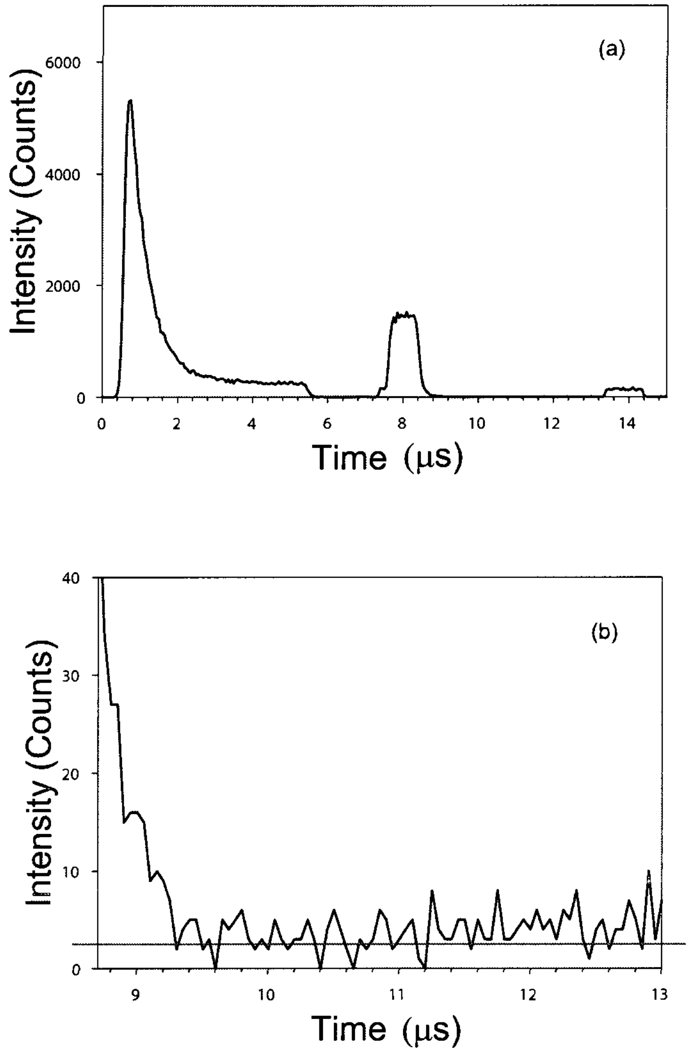

FIG. 60: Preliminary result from experiments done with enhanced light penetration by using the light shift laser. The hyperfine optical repumper signal, probe laser signal and signal from light shift laser are shown in (a). Transient after probe laser is shut off is shown in (b).

CHAPTER VI

CONCLUSIONS

The light scattering experiments described in this dissertation have shown that the results strongly depend on hyperfine optical pumping, detuning from atomic resonance, and the density of the sample. The sample that is initially prepared in the F = 1 hyperfine ground state is optically pumped to the F = 2 hyperfine ground state with a repumper laser tuned on resonance with the F = 1 → F′ = 2 hyperfine transition of the D_2 resonance line of atomic ^{87}Rb. Hyperfine optical pumping results alone reveal that the optical pumping time varies with the density of the atomic sample. Complete optical pumping in times of up to $\sim 5\ \mu$s indicates that the sample is very optically deep. The agreement between the estimates made by using the QUEST parameters and the results are satisfactory. In an effort to try trapping probe light in high density regions of the sample, combined hyperfine optical pumping and resonant F = 2 → F′ = 3 hyperfine transition probing measurements were made. These measurements did not show long time decays of the fluorescence signal after the repumper and probe lasers were turned off. We concluded that the optical pumping process is slow compared to the natural lifetime of the excited state causing the probe to escape before the density of the F = 2 ground state reaches the desired level. Also the repumper optically pumps the sample from the outside to the inside, thus blocking the probe radiation before it reaches the sample center. The probe intensity measurements support this argument as the results show no saturation effects even at 12 mW/cm^2 where the saturation intensity is $\sim$ 1.7 mW/cm^2. The intensity of the probe is continuously decreased according to Beer's law as it propagates through the sample.

The density and detuning dependent measurements made with the probe tuned near resonance with the F = 2 → F′ = 3 hyperfine transition indicate that the light has minimal penetration into the sample for the maximum density sample. The detected fluorescence mainly is coming from a shell of atoms with a thickness of a few optical mean free paths. This observation is supported by the shorter diffusive lifetime of the fluorescence decay after the probe laser is turned off. A developed heuristic model to analyze these data supports these arguments. The model predicts an effective Gaussian medium that gives similar results to the data. We conclude that the detected fluorescence is coming from the less dense part of the sample and the light propagates in the sample by diffusion. To observe the fluorescence from the longest lived mode, other experimental methods are required to excite the atoms in the optically deepest part of the sample. The light shift method as described at the end of the results chapter looks promising in this sense. This method needs to be improved by stabilizing the laser frequency and by increasing the detuning and the total power of the light shift laser to minimize the scattering rate while keeping the light shift at an acceptable level. This method can also be extended to include a region of improved QUEST loading by forming a crossed dipole trap by using the light shift laser as explained in [56].

During the course of this research a MOT and the QUEST apparatus were built. Stable diode lasers that can stay locked for hours were designed and built to supply the demand of the long hours of data taking time needed in this experiment. The LIAD method was implemented to improve the loading of MOT and the QUEST and to decrease the signal background. The LIAD results were satisfactory but since none of the chamber viewports were built for ultraviolet light the design still needs improvements. The fluorescence coming from the sample needs to accumulate for hours before reaching an acceptable signal to noise ratio. This could be improved by improving the loading efficiency of the QUEST from the MOT, loading the MOT quicker and thus improving the duty cycle of the experiment or improving the detection efficiency.

Future work on this project should focus on improving the day to day variations of the sample by better managing the CO_2 laser beam. Even though the Coherent Deos CO_2 laser beam is of exceptionally high quality, the long term maintenance of the laser is not trivial and the supporting documentation that comes with the laser does not address possible issues. The laser needs efficient cooling and the laser seems to lose power and degrade in time if not efficiently cooled. The built in shutter does not get enough cooling because of design flaws and tends to overheat and cause leaking if used for longer periods of time. Another suggested improvement is the design of the focusing lenses. The current design does not have room for compensating the thermal imaging effects caused by the acousto optic modulator (AOM). A better design would be to use two telescopes, one for the beam to clear the AOM and one for expanding the beam to a desired width before focusing into the chamber. Also better mounting schemes are needed for the AOM and the focusing lens to improve the alignment of the CO_2 laser.

We also point out that these experiments suffer from a lack of theoretical studies specific to the media discussed in this thesis. In the case of light localization in an ultracold atomic medium, the theory is significantly trailing the experiments. As more specific theory is made the results would be understood better and the experiments would be guided in more systematic directions.

Finally, the long term aim of this project is experimental demonstration of Anderson localization of light. This dissertation has focused on the multi year effort to develop and characterize the instrumentation, sample formation and to study several techniques for preparing optical excitations in this unusual medium. Subsequent projects will build on this effort and explore light localization and other collective quantum optical phenomena at high atomic density.

BIBLIOGRAPHY

[1] R. Loudon, *The Quantum Theory of Light*, 3rd ed., (Oxford University Press, Oxford, 2000).

[2] G. Labeyrie, E. Vaujour, C. A. Muller, D. Delande, C. Miniatura, D. Wilkowski and R. Kaiser, Phys. Rev. Lett. 91, 22 (2003).

[3] P. W. Anderson, Phil. Mag. B 52, 505-509 (1985).

[4] C. A. Müller, C. Miniatura, D. Wilkowski, R. Kaiser and D. Delande, Phys. Rev. A 72, 053405 (2005).

[5] Y. Kuga and J. Ishimaru, J. Opt. Soc. Am. A 1, 831 (1984).

[6] P.E. Wolf and G. Maret, Phys. Rev. Lett. 55, 2696 (1985).

[7] M. Albada and A. Lagendijk, Phys. Rev. Lett. 55, 2692 (1985).

[8] G. Labeyrie, F. De Tomasi, J-C Bernard, C. A. Muller, C.A. Miniatura, and R. Kaiser, Phys. Rev. Lett. 83, 5266-5270 (1999).

[9] G. Labeyrie, C. A. Muller, D. S. Wiersma, C. Miniatura, and R. Kaiser, J. Opt. B: Quantum Semiclass. Opt. 2, 672-685 (2000).

[10] D. V. Kupriyanov, I. M. Sokolov, C. I. Sukenik, S. Balik, and M. D. Havey, Laser Phys. Lett. 3, 223 (2006).

[11] R. Kaiser and M. D. Havey, Optics and Photonics News 16, 38-43 (1995).

[12] C. A. Müller, T. Jonckheere, C. Miniatura, and D. Delande, Phys. Rev. A 64, 053804 (2001).

[13] Y. Bidel, B. Klappauf, J. C. Bernard, D. Delande, G. Labeyrie, C. Miniatura, D. Wilkowski and R. Kaiser, Phys. Rev. Lett. 88, 203902 (2002).

[14] G. Labeyrie, D. Delande, R. Kaiser, C.A. Miniatura, Phys. Rev. Lett. 97, 013004 (2006).

[15] G. Labeyrie, C. Miniatura, C. A. Muller, O. Sigwarth, D. Delande, and R. Kaiser, Phys. Rev. Lett. 89, 163901 (2002).

[16] T. Chanelire, D. Wilkowski, Y. Bidel, R. Kaiser and C. Miniatura, Phys. Rev. E 70, 036602 (2004).

[17] D. V. Kupriyanov, I. M. Sokolov and M. D. Havey, Optics Comm. 243, 165-173 (2004).

[18] M. D. Havey, and D. V. Kupriyanov, Physica Scripta 72, C30-C32 (2005).

[19] P. Kulatunga, C. I. Sukenik, S. Balik, M. D. Havey, D. V. Kupriyanov, and I. M. Sokolov, Phys. Rev. A 68, 033816 (2003).

[20] D. V. Kupriyanov, I. M. Sokolov, N. V. Larionov, P. Kulatunga, C. I. Sukenik, S. Balik, and M. D. Havey, Phys. Rev. A 69, 033801 (2004).

[21] S. Balik, P. Kulatunga, C. I. Sukenik, M. D. Havey, I. M. Sokolov, and D. V. Kupriyanov, J. Mod. Optics 52, 2269-2278 (2005).

[22] P. W. Anderson, Phys. Rev. 109, 1492 (1958).

[23] A.F. Ioffe and A.R. Regel, Progr. Semicond. 4, 237 (1960).

[24] N. F. Mott, Rev. Mod. Phys. 40, 677 - 683 (1968).

[25] D.S. Wiersma, P. Bartolini, Ad Lagendijk, and R. Righini, Nature 390, 671 (1997).

[26] C.M. Aegerter and G. Maret, *Coherent backscattering and Anderson localization of light*, in Progress in Optics 52, 1 (2009).

[27] M. Storzer, P. Gross, C.M. Aegerter, and G. Maret, Phys. Rev. Lett. 96, 063904 (2006).

[28] C.M. Aegerter, M. Storzer, and G. Maret, Europhys. Lett. 75, 562-568 (2006).

[29] T. Schwartz, Nature 446, 5255 (2007).

[30] Y. Lahini, Phys. Rev. Lett. 100, 013906 (2008).

[31] Hefei Hu, Nature Physics 4, 945 (2008).

[32] Giacomo Roati, Chiara D'Errico, Leonardo Fallani, Marco Fattori, Chiara Fort, Matteo Zaccanti, Giovanni Modugno, Michele Modugno and Massimo Inguscio, Letter to Nature 453, 895-898 (2008).

[33] Juliette Billy, Vincent Josse, Zhanchun Zuo, Alain Bernard, Ben Hambrecht, Pierre Lugan, David Clment, Laurent Sanchez-Palencia, Philippe Bouyer and Alain Aspect, Nature 453, 891-894 (2008).

[34] M.H. Anderson, J.R. Ensher, M.R. Matthews, C.E. Wieman, and E.A. Cornell, Sci. 269, 198-201 (1995).

[35] K.B. Davis, M.O. Mewes, M.R. Andrews, N.J. van Druten, D.S. Durfee, D.M. Kurn, and W. Ketterle, Physical Review Letters 75, 22 (1995).

[36] M. Greiner, O. Mandel, T. Esslinger, T. W. Hnsch, I. Bloch, Nature 415, 6867 (2002).

[37] C. J. Pethick and H. Smith, *Bose Einstein Condensation in Dilute Gases*, (Cambridge University Press, Cambridge, 2002).

[38] K. T. Compton, Phys. Rev. 20, 283 (1922).

[39] P. Sheng, *Introduction to Wave Scattering, Localization, and Mesoscopic Phenomena*, (Academic, San Diego, 1995).

[40] B. A. van Tiggelen, *Mesoscopic Light Scattering in Atomic Physics*, Les Houches Summer School 72, 371 (2001).

[41] T. Holstein, Phys. Rev. 72, 1212 (1947).

[42] P. Barthelemy, J. Bertolotti and D. S. Wiersma, Nature (London) 453, 495 (2008).

[43] Daniel A. Steck, Rubidium 87 D Line Data, available online at http://steck.us/alkalidata (revision 2.0.1, 2 May 2008).

[44] P. Sheng, *Scattering and Localization of Classical Waves in Random Media*, (World Scientific, Singapore, 1990).

[45] Ad Lagendijk and B.A. van Tiggelen, Physics Reports 270, 143 (1996).

[46] E. Larose, L. Margerin, B. A. van Tiggelen and M. Campillo, Phys. Rev. Lett. 93, 048501 (2004).

[47] G. Bayer and T. Niederdrank, Phys. Rev. Lett. 70, 3884-3887 (1993).

[48] E. Akkermans, A. Gero, and R. Kaiser, Phys. Rev. Lett. 101, 103602 (2008).

[49] E. Abrahams, P. W. Anderson, D. Licciardello, T. V. Ramakrishnan, Phys. Rev. Lett. 42, 673-676 (1979).

[50] A. A. Chabanov, M. Stoytchev, and A. Z. Genack, Nature 404, 850 (2000).

[51] Dmitry Budker, Derek F. Kimball and David P. Demille, *Atomic Physics*, (Oxford University Press, Oxford, 2004).

[52] D. Wilkowski, Y. Bidel, T. Chanelire, R. Kaiser, B. Klappauf, G. Labeyrie, C.A. Mller and C. Miniatura, Physica B 328, 157 (2003).

[53] Harold J. Metcalf, Peter van der Straten, *Laser Cooling and Trapping*, (Springer-Verlag, New York, 1999).

[54] E. Raab, M. Pentiss, A. Cable, S. Chu, and D. Pritchard, Phys. Rev. Lett. 59, 2631 (1987).

[55] Rudolf Grimm, Mattias Weidenmuller, and Yurii Ovchinnokov, Advances Atom., Mol., and Opt. Phys. 42, 95 (2000).

[56] Paul F. Griffin, *Laser Cooling and Loading of Rb into A Large Period, Quasi-Electrostatic, Optical Lattice*, Ph.D. Thesis, Durham University, (2005).

[57] C. Klempt, T. van Zoest, T. Henninger, O. Topic, E. Rasel, W. Ertmer, and J. Arlt, Phys. Rev. A 73, 013410 (2006).

[58] C. J. Hawthorn, K. P. Weber, and R. E. Scholten Rev. Sci. Instrum. 72, 4477 (2001).

[59] A. S. Arnold, J. S. Wilson and M. G. Boshier, Rev. Sci. Instrum. 69, 1236 (1998).

[60] L. D. Turner, K. P. Weber, C. J. Hawthorn and R. E. Scholten, Opt. Communic. 201, 391 (2002).

[61] M. D. Barrett, and J. A. Sauer, and M. S. Chapman, Phys. Rev. Lett. 87, 10404 (2001).

[62] S. R. Granade, and M. E. Gehm, and K. M. O'Hara, and J. E. Thomas, Phys. Rev. Lett. 88, 120405 (2002).

[63] T. A. Savard, K. M. O'Hara, and J. E. Thomas, Phys. Rev. A 56, 1095 (1997).

[64] C. S. Adams, H. J. Lee, N. Davidson, M. Kasevich, and S. Chu, Phys. Rev. Lett. 74, 3577 (1995).

[65] M. E. Gehm, K. M. O'Hara, T. A. Savard, and and J. E. Thomas, Phys. Rev. A 58, 3914 (1998).

[66] S. Bali, K. M. O'Hara, M. E. Gehm, S. R. Granade, and J. E. Thomas, Phys. Rev. A 60, R29-R32 (1999).

[67] K. M. O'Hara, *Optical Trapping and Evaporative Cooling of Fermionic Atoms*, Ph.D. Thesis, Duke University, (2000).

[68] S. R. Granade, *Preparation of an Optically-Trapped Degenerate Fermi Gas of 6Li: Characterization of Degeneracy*, Ph.D. Thesis, Duke University, (2002).

[69] M. E. Gehm, *Preparation of an Optically-Trapped Degenerate Fermi Gas of 6Li: Finding the Route to Degeneracy*, Ph.D. Thesis, Duke University, (2003).

[70] L. D. Landau and E. M. Lifshitz, *Mechanics*, (Oxford, Pergamon 1976).

[71] S. Balik, A. L. Win, M. D. Havey, Phys. Rev. A 80, 023404 (2009).

[72] Yan Bo, Li Xiao-Lin, Ke Min, and Wang Yu-Zhu, Chin. Phys. B17, 1674 (2008).

[73] Pengfei Zhang, Haichao Zhang, Xingping Xu, and Yuzhu Wang, Chin. Opt. Lett. 6, 87 (2008).

[74] Kihwan Kim, Heung-Ryoul Noh, and Wonho Jhe, Optics Comm. 236, 349 (2004).

[75] T. Insperger and G. Stepan, Proc. R. Soc. Lond. A 458, 1989 (2002).

[76] M. Singh, M. Volk, A. Akulshin, A. Sidorov, R. McLean and P. Hannaford, J. Physics B. 41, 165301 (2008).

[77] S. Balik and M. D. Havey I. M. Sokolov and D. V. Kupriyanov, Phys. Rev. A 79, 033418 (2009).

[78] S. D. Gensemer, P. L. Gould, P. J. Leo, E. Tiesinga and C. J. Williams, Phys. Rev. A 62, 030702 (2000).

[79] G. Labeyrie, Mod. Phys. Lett. B 22, 73 (2008).

APPENDIX A

RANDOM WALK

Light propagation in ultracold gases can be thought as a random walk of the light wave where each scattering event can be considered as a step with the average step size being the mean free path of the light, ℓ. To develop a better understanding of the process let us consider a two dimensional random walk problem as shown in Fig. 61. In this model we will consider a total of N steps each in an arbitrary direction with random phase θ. The step size is defined as

$$\text{step size } = \ell e^{i\theta}. \tag{202}$$

The position of the light z after N scattering events in the complex plane is given by

$$z = \ell \sum_{n=1}^{N} e^{i\theta_n}. \tag{203}$$

The distance from the starting point to the last scattering event after N consecutive scattering is equal to the modulus of z, $|z|$:

$$\begin{aligned} |z|^2 &= z \cdot z^* \\ &= \ell^2 \sum_{n=1}^{N} e^{i\theta_n} \sum_{k=1}^{N} e^{-i\theta_k} \\ &= N + \ell^2 \sum_{n,k=1}^{N} e^{i(\theta_n - \theta_k)} \quad n \neq k. \end{aligned} \tag{204}$$

Then the expectation value of $|z|^2$ is

$$\left\langle |z|^2 \right\rangle = N + \ell^2 \left\langle \sum_{n,k=1}^{N} e^{i(\theta_n - \theta_k)} \right\rangle \quad n \neq k. \tag{205}$$

The second term in this equation is clearly equals zero as each displacement is random that averages the sum to zero. So the root mean square of the total displacement d_{rms} is given by,

$$d_{rms} = |z|_{rms} = \ell\sqrt{N}. \tag{206}$$

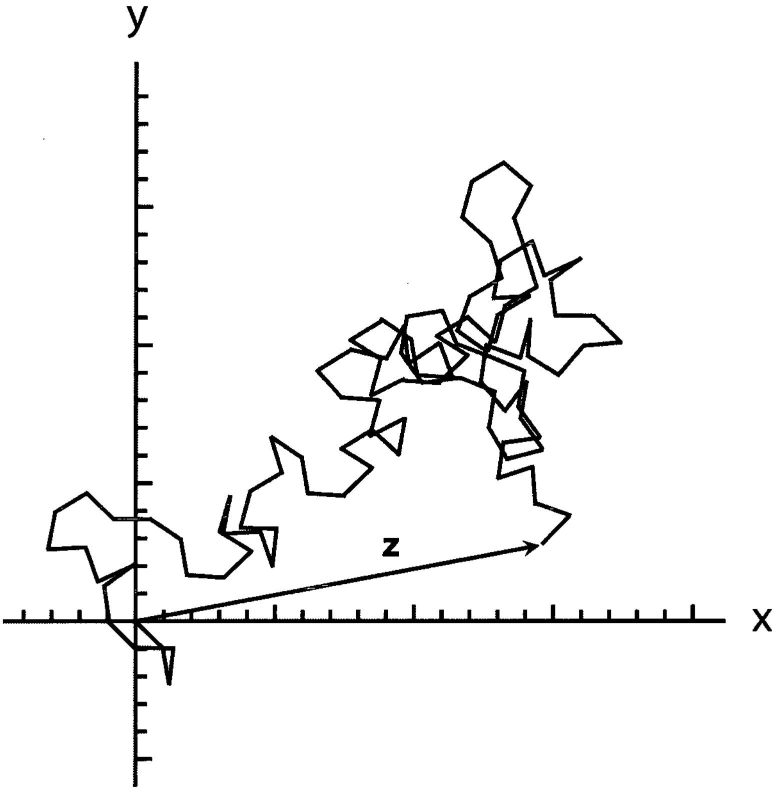

FIG. 61: Random walk problem in 2D.

APPENDIX B

VACUUM CHAMBER SETUP

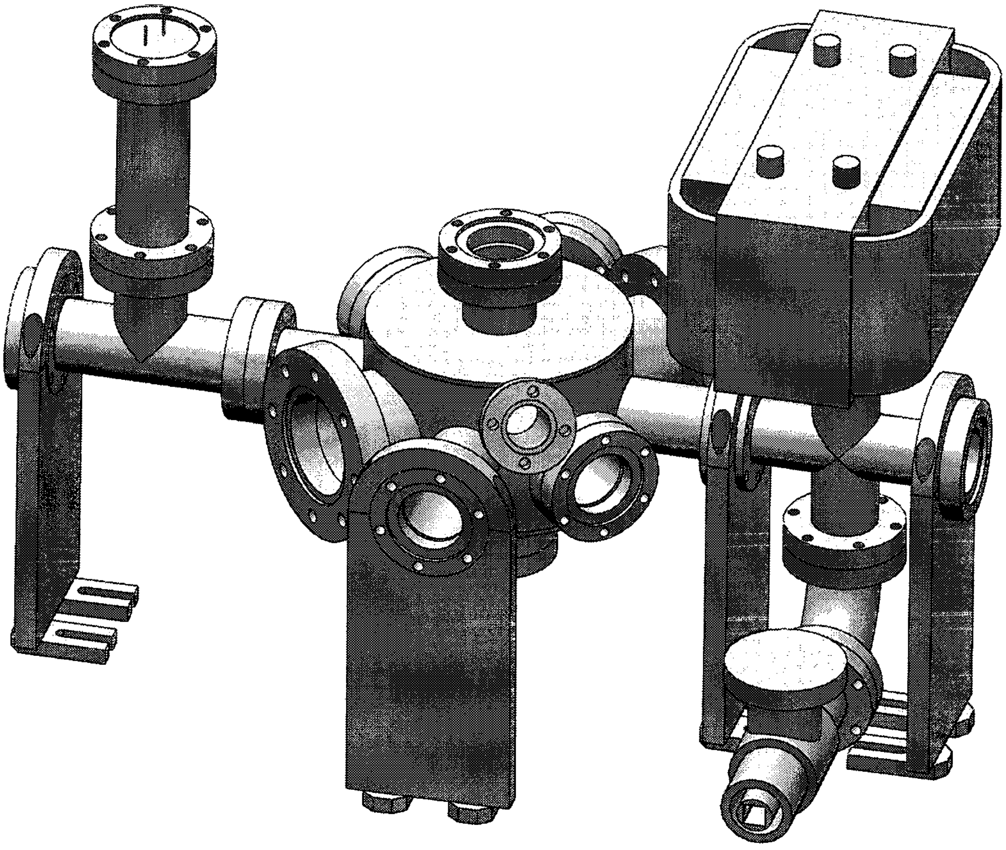

FIG. 62: The complete vacuum assembly consists of the main chamber, a 20 liter ion pump, SAES getters attached to electrical feedthrough and valve.

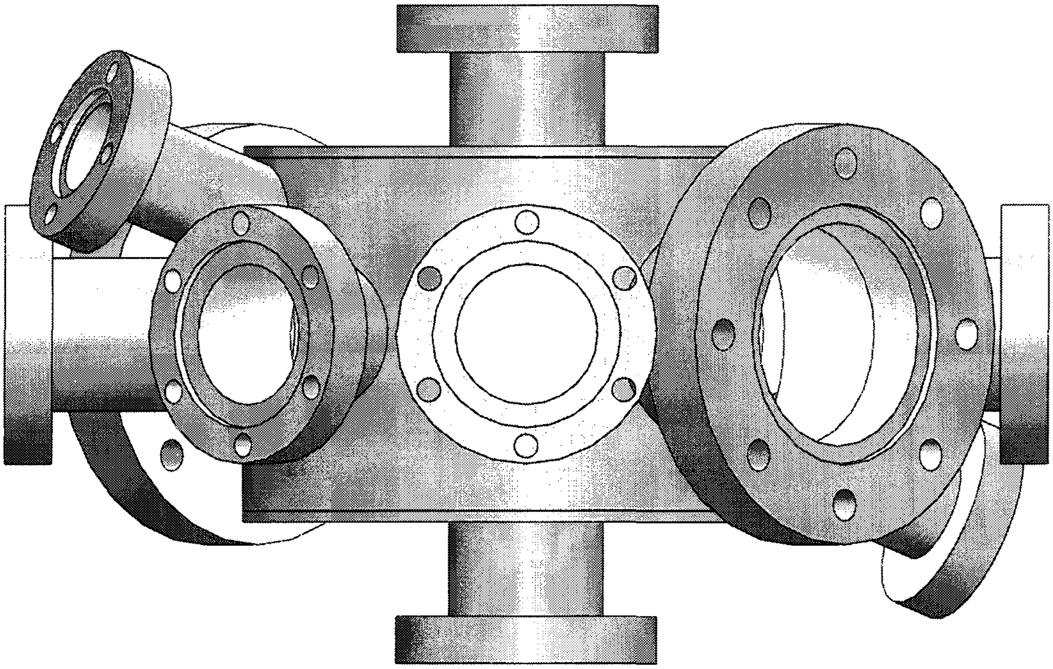

FIG. 63: The vacuum chamber consists of 12 viewports; 8 of 2-3/4" AR coated for 780nm, 2 of 2-1/8" and 2 of 4-1/2" ZnSe windows.

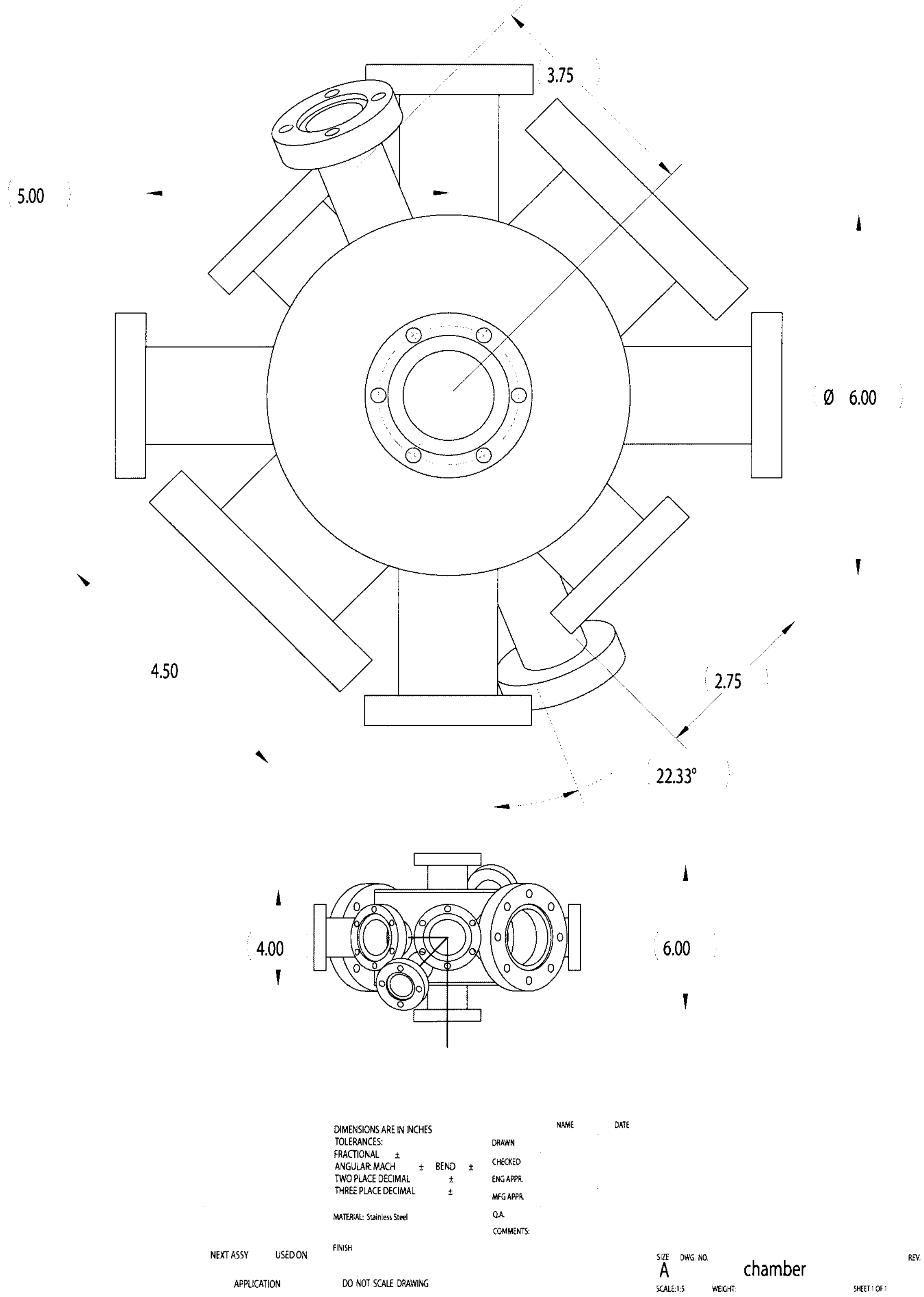

DIMENSIONS ARE IN INCHES
TOLERANCES:
FRACTIONAL ±
ANGULAR: MACH ± BEND ±
TWO PLACE DECIMAL ±
THREE PLACE DECIMAL ±

MATERIAL: Stainless Steel

FINISH

NAME DATE
DRAWN
CHECKED
ENG APPR.
MFG APPR.
Q.A.
COMMENTS:

NEXT ASSY USED ON
APPLICATION DO NOT SCALE DRAWING

SIZE A
DWG. NO. chamber
REV.
SCALE:1:5 WEIGHT: SHEET 1 OF 1

FIG. 64: The drawing of the vacuum chamber is showing only the important dimensions.; 8 of 2-3/4" AR coated for 780nm, 2 of 2-1/8" and 2 of 4-1/2" ZnSe windows.

APPENDIX C

DIODE LASER SETUP

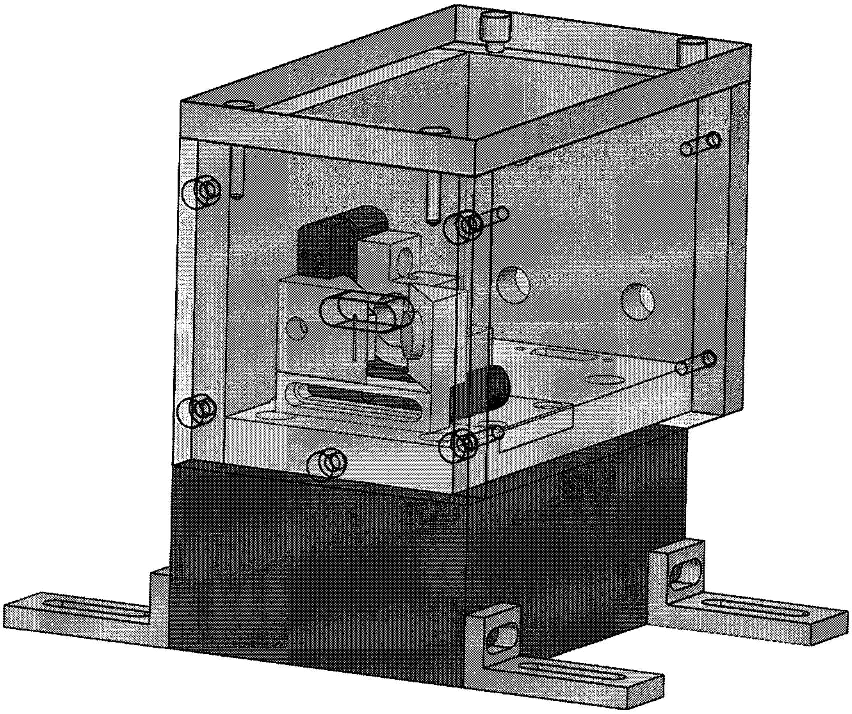

FIG. 65: Figure showing the complete diode laser assembly inside the box

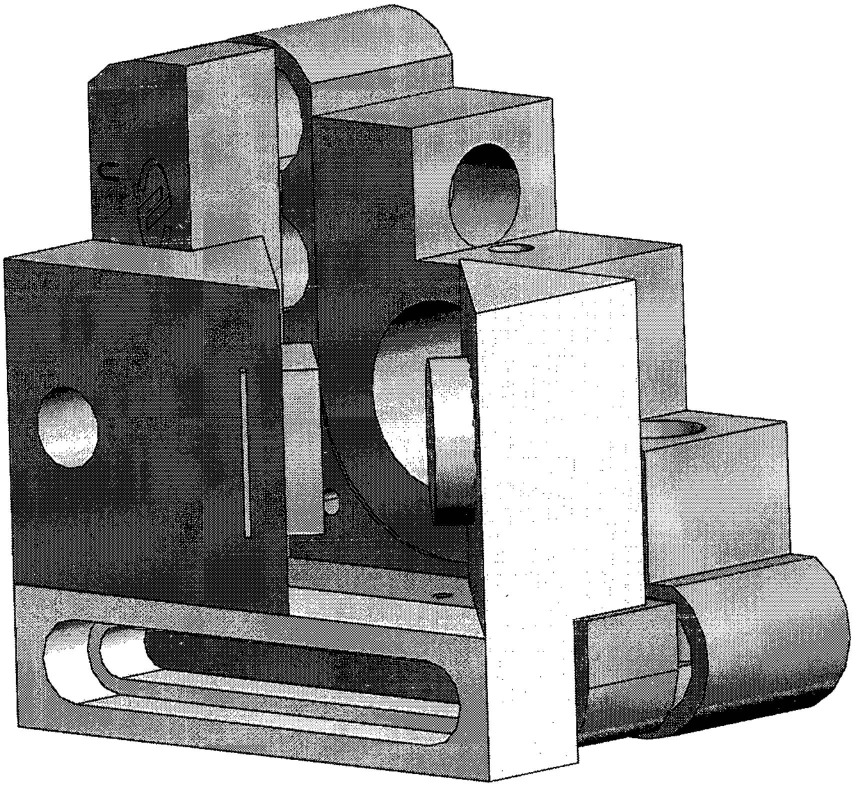

FIG. 66: ECDL configured in Littrow design. Everything is mounted on a single mirror mount.

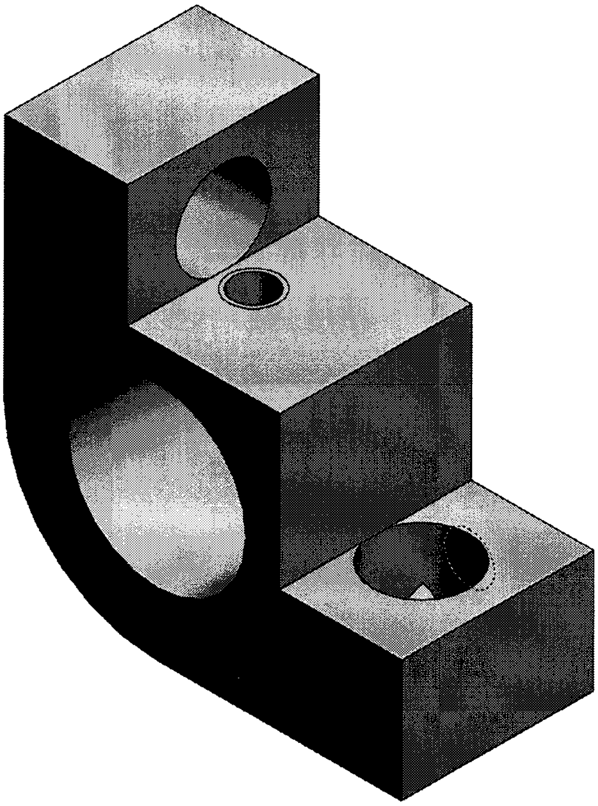

FIG. 67: Collimation tube holder

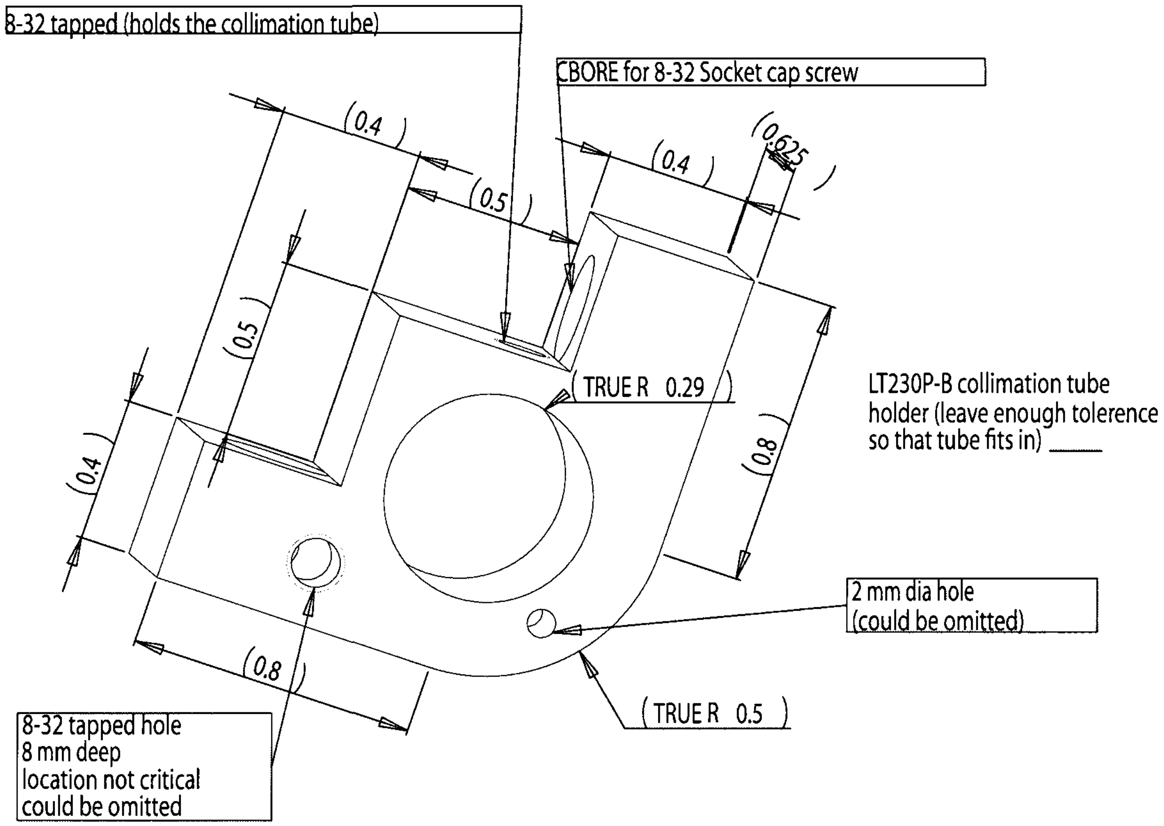

FIG. 68: Collimation tube holder drawing

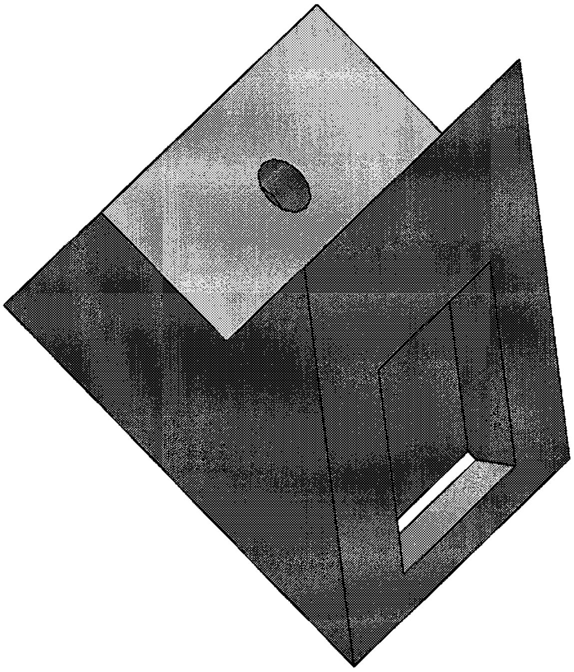

FIG. 69: Grating holder

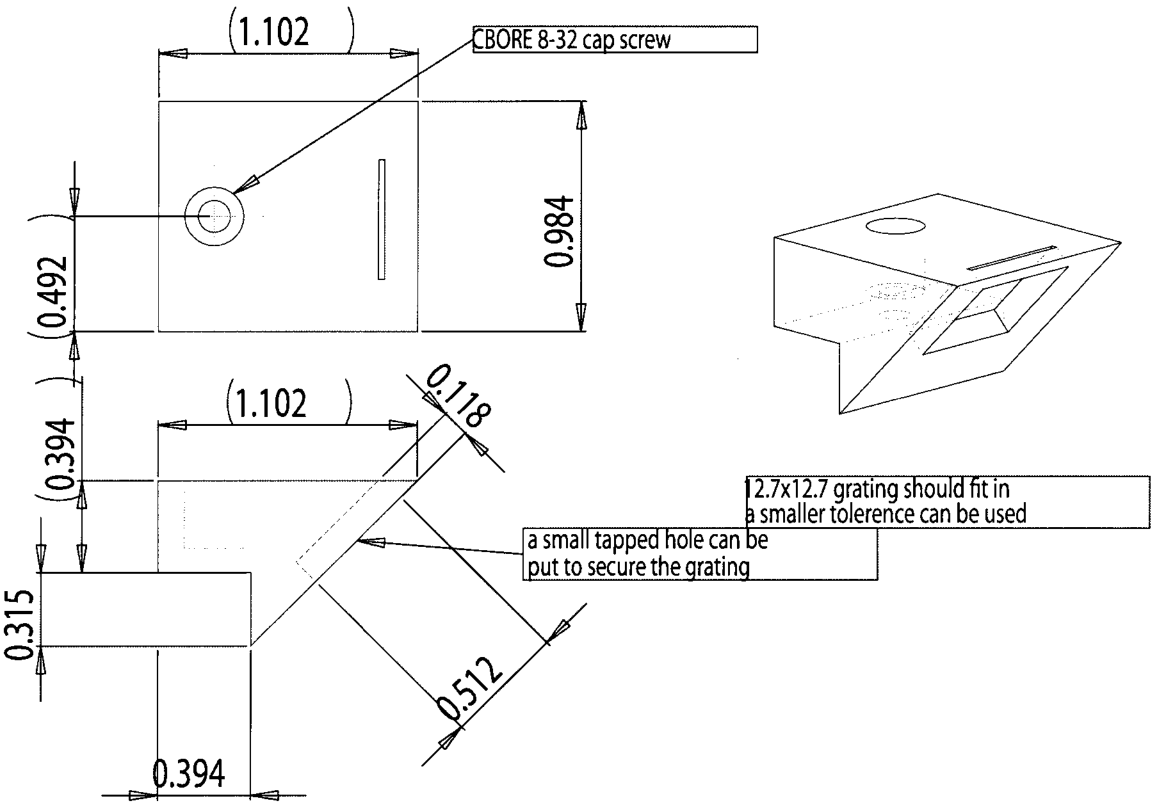

FIG. 70: Grating holder drawing

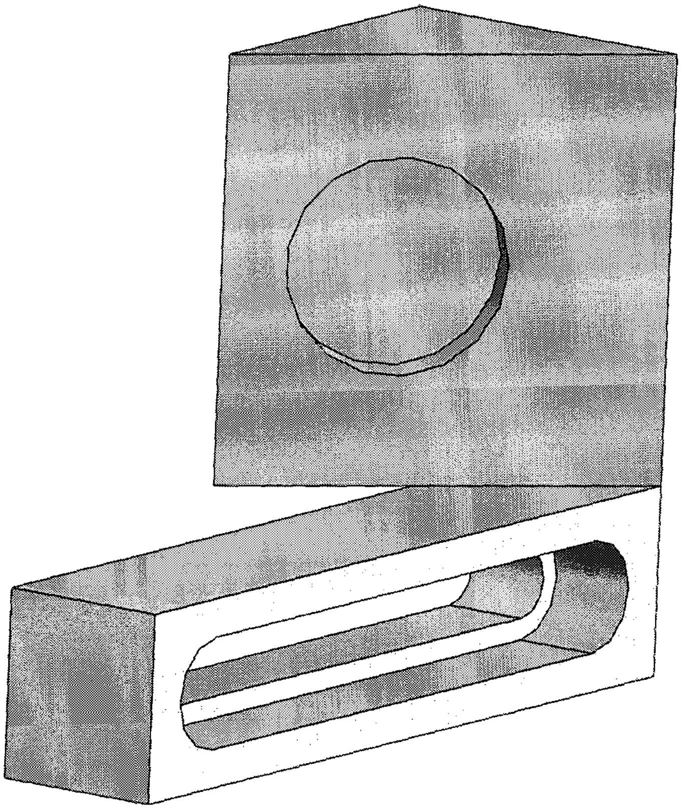

FIG. 71: Mirror holder

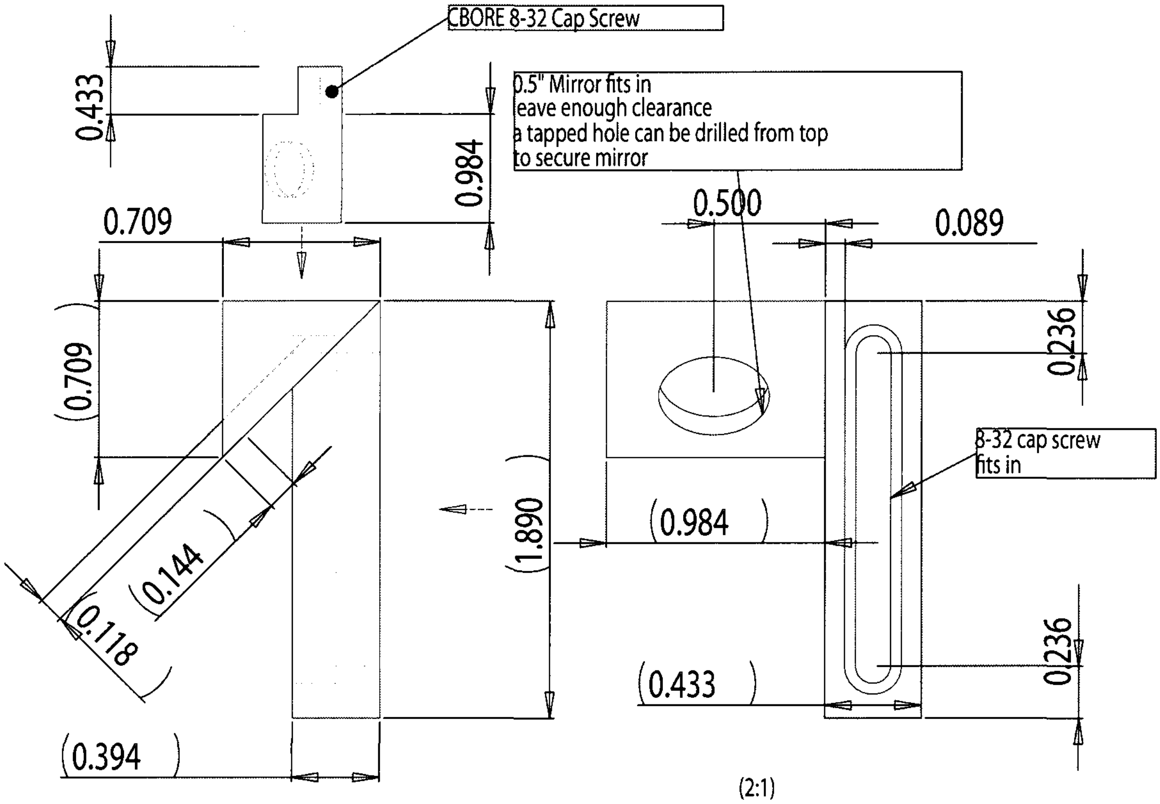

FIG. 72: Mirror holder drawing

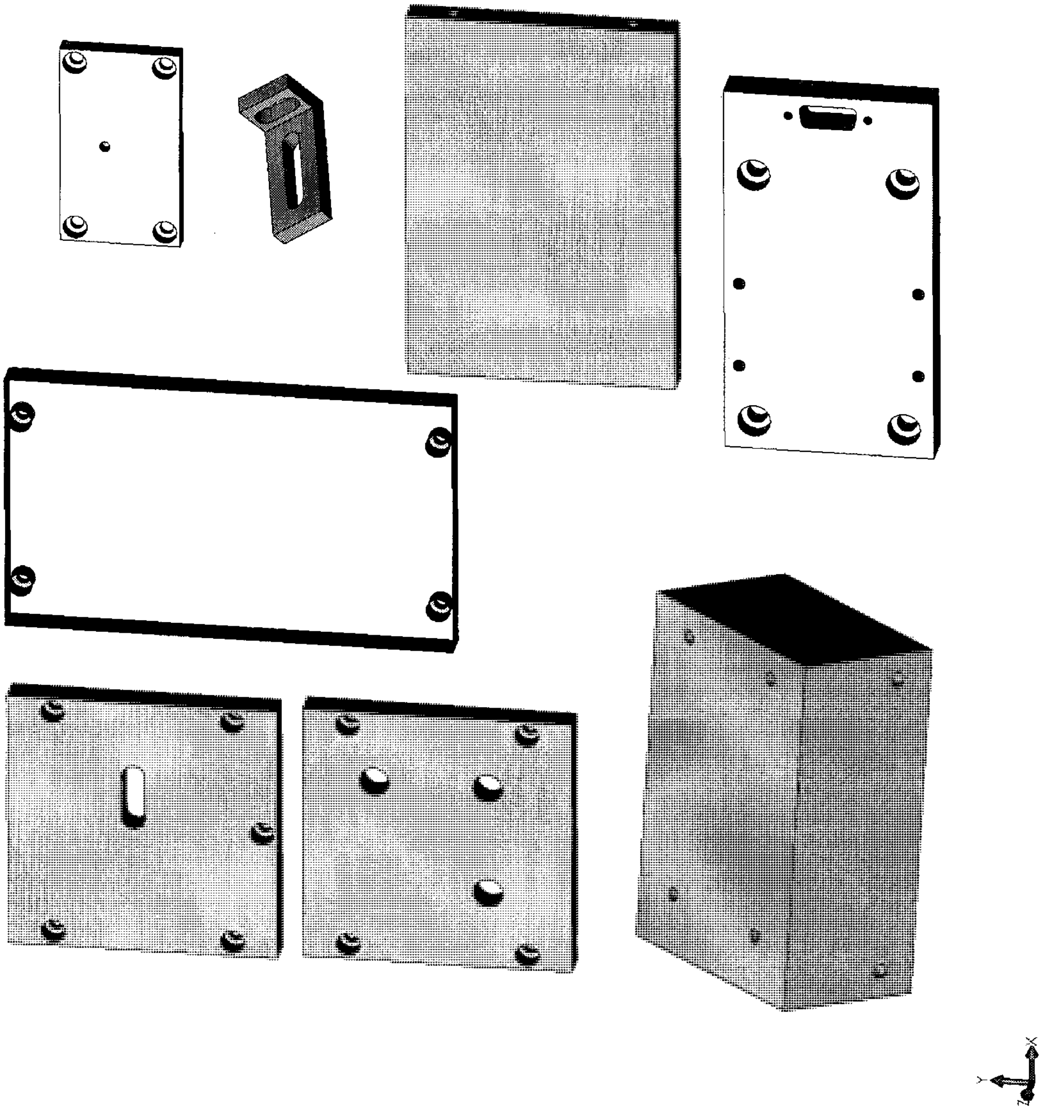

FIG. 73: Figure showing individual components of the box assembly

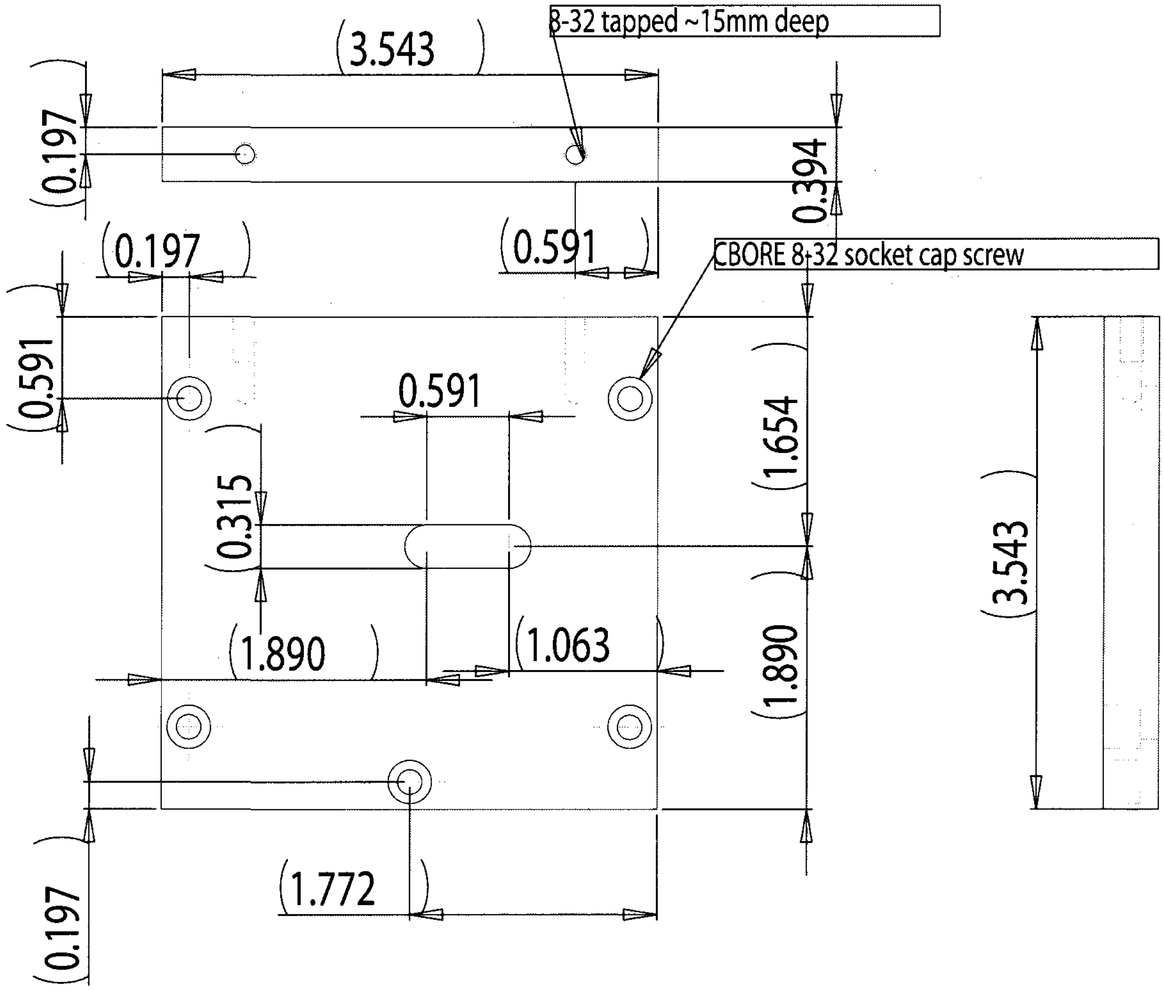

FIG. 74: Front of the laser box.

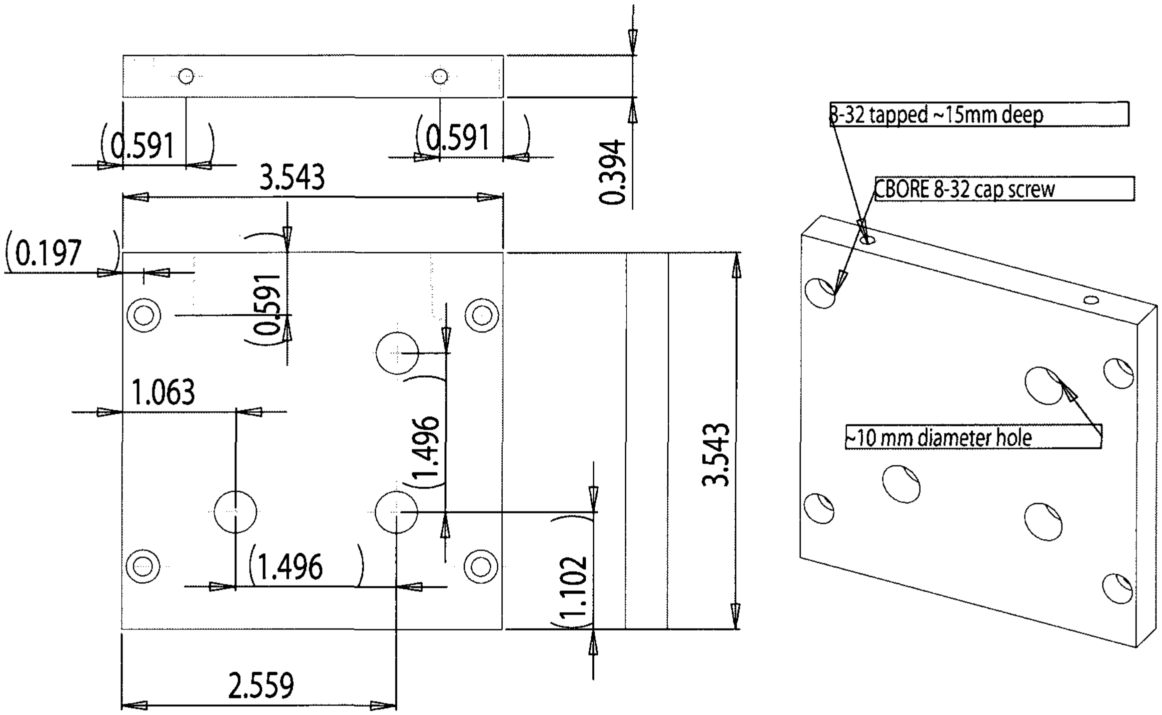

FIG. 75: Back of the laser box

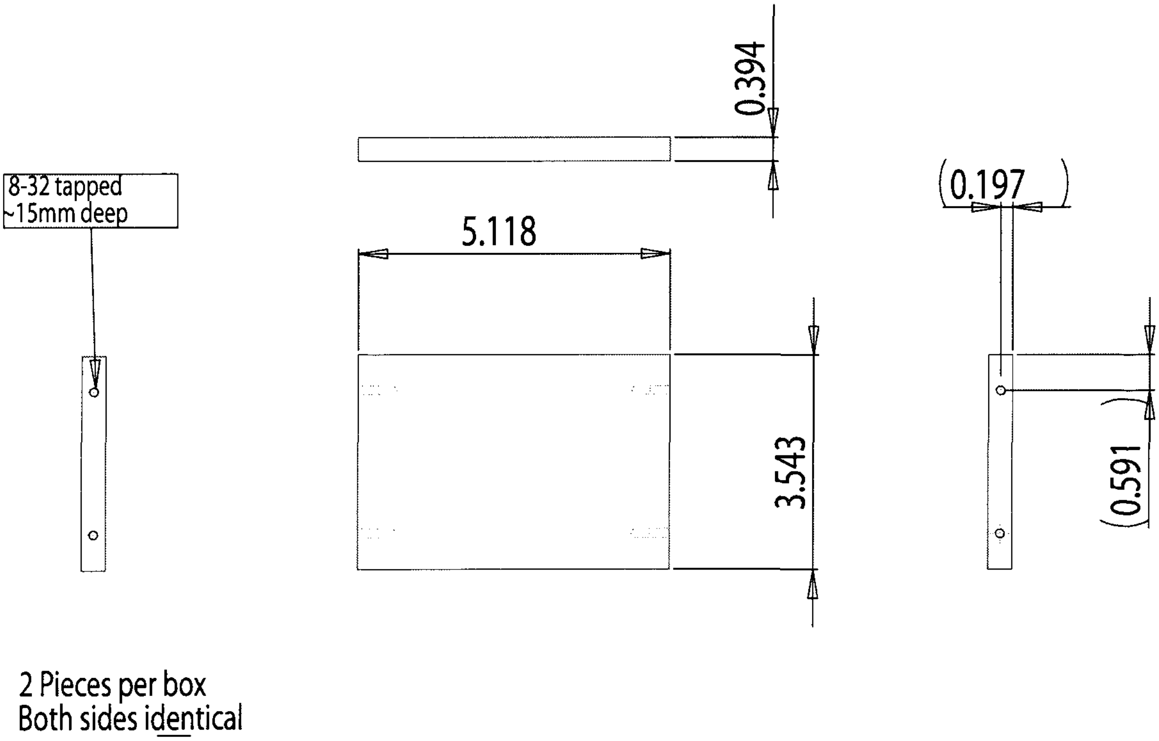

FIG. 76: Side of the laser box. Both sides are identical.

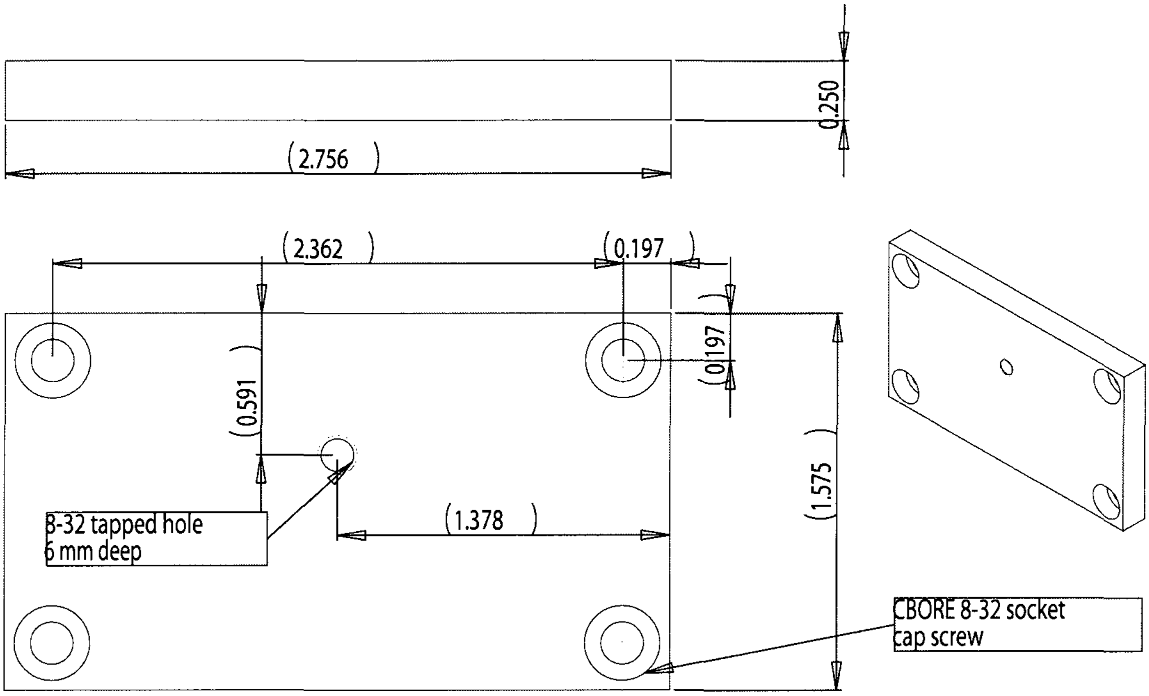

FIG. 77: Plate: Thorlabs mirror mount sits on this plate. There is TEC between this plate and the base.

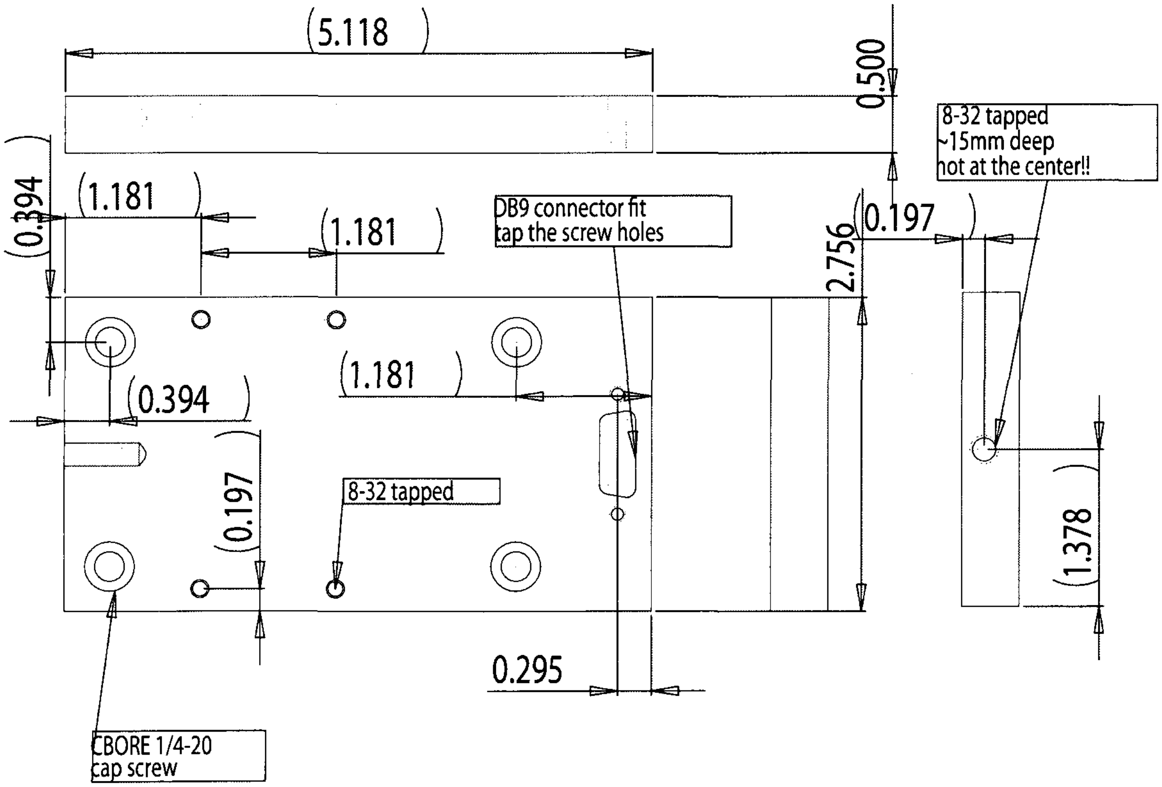

FIG. 78: Base of the laser box. Also holds the whole laser assembly.

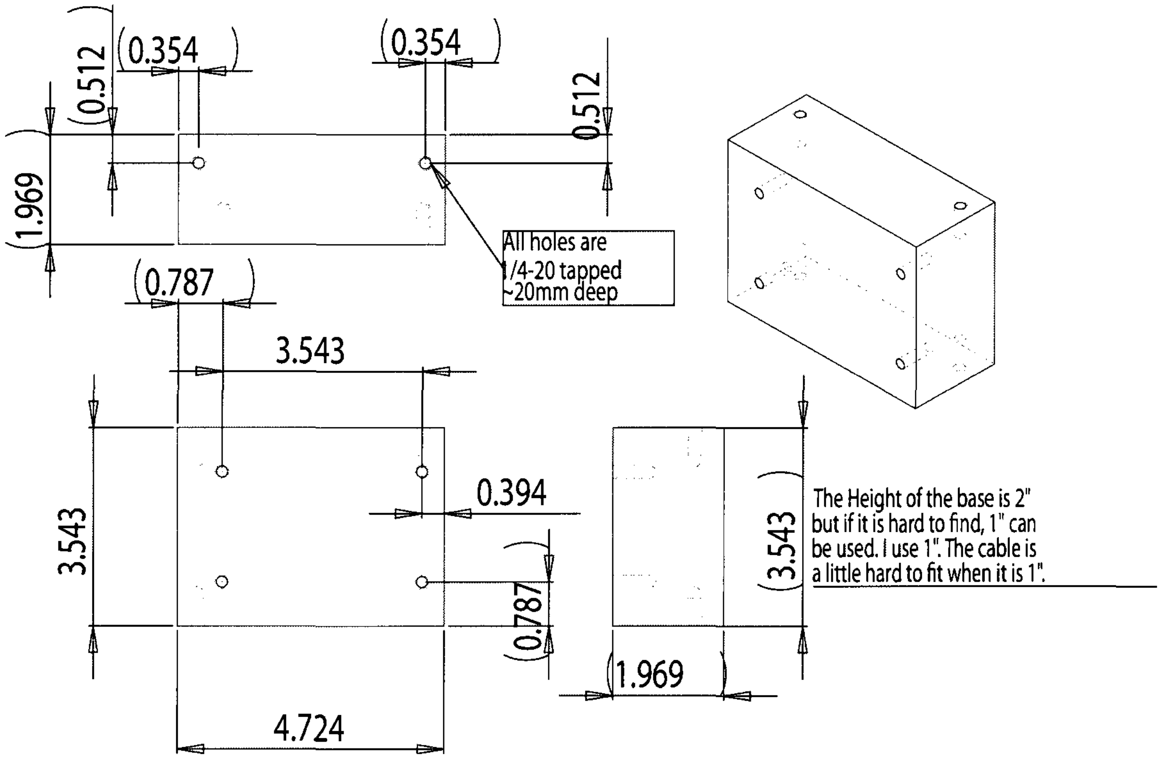

All holes are 1/4-20 tapped ~20mm deep

The Height of the base is 2" but if it is hard to find, 1" can be used. I use 1". The cable is a little hard to fit when it is 1".

FIG. 79: Heavy Base: 1” thick base of the laser box.

APPENDIX D

LABVIEW PROGRAM FOR PCI-DIO-32-HS

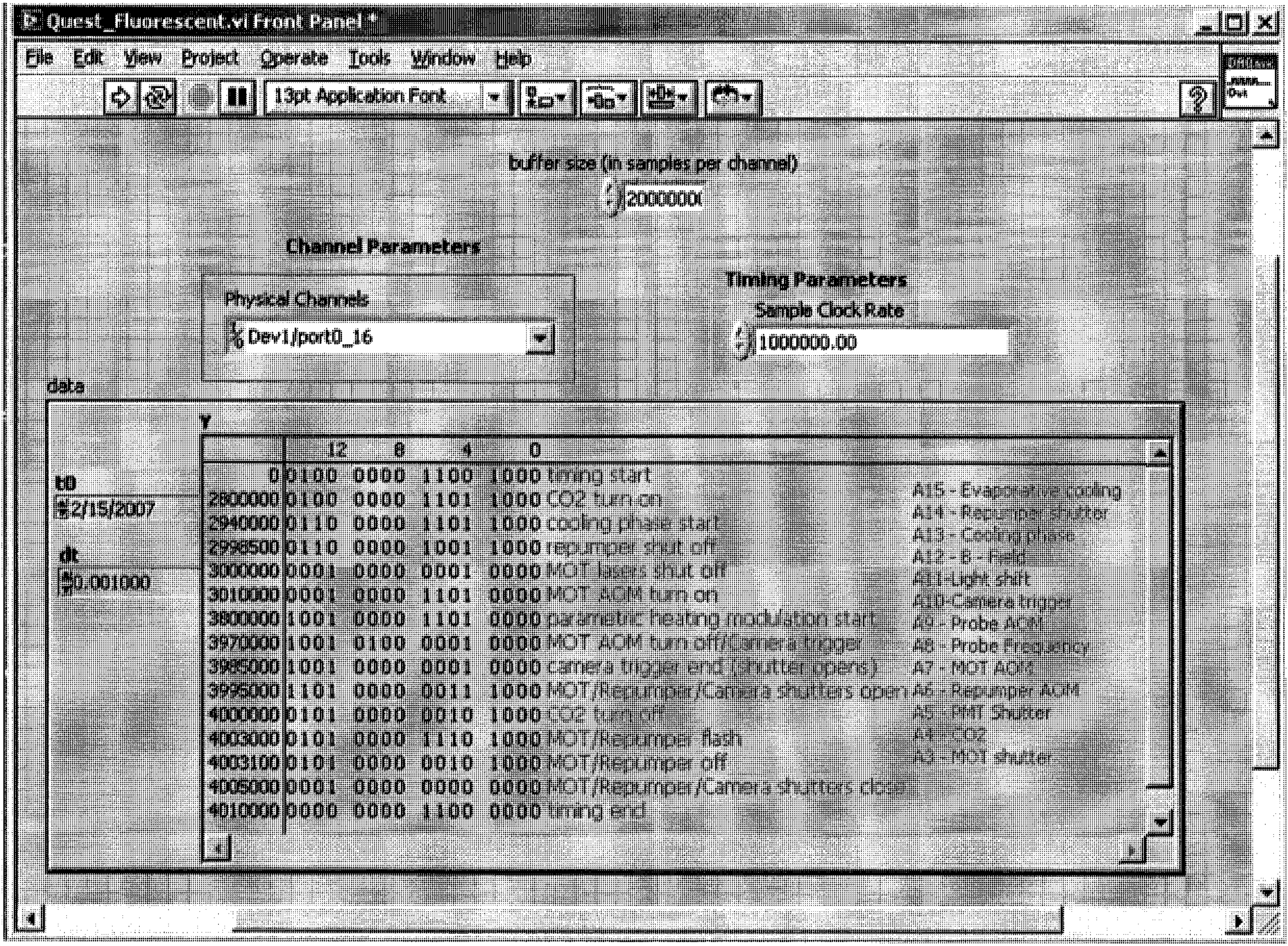

buffer size (in samples per channel): 20000000

Channel Parameters

Physical Channels: Dev1/port0_16

Timing Parameters

Sample Clock Rate: 1000000.00

data

t0: 2/15/2007

dt: 0.001000

```
             12     8     4     0
       0 0100  0000  1100  1000 timing start
 2800000 0100  0000  1101  1000 CO2 turn on
 2940000 0110  0000  1101  1000 cooling phase start
 2998500 0110  0000  1001  1000 repumper shut off
 3000000 0001  0000  0001  0000 MOT lasers shut off
 3010000 0001  0000  1101  0000 MOT AOM turn on
 3800000 1001  0000  1101  0000 parametric heating modulation start
 3970000 1001  0100  0001  0000 MOT AOM turn off/Camera trigger
 3985000 1001  0000  0001  0000 camera trigger end (shutter opens)
 3995000 1101  0000  0011  1000 MOT/Repumper/Camera shutters open
 4000000 0101  0000  0010  1000 CO2 turn off
 4003000 0101  0000  1110  1000 MOT/Repumper flash
 4003100 0101  0000  0010  1000 MOT/Repumper off
 4005000 0001  0000  0000  0000 MOT/Repumper/Camera shutters close
 4010000 0000  0000  1100  0000 timing end
```

```
A15 - Evaporative cooling
A14 - Repumper shutter
A13 - Cooling phase
A12 - B - Field
A11-Light shift
A10-Camera trigger
A9 - Probe AOM
A8 - Probe Frequency
A7 - MOT AOM
A6 - Repumper AOM
A5 - PMT Shutter
A4 - CO2
A3 - MOT shutter
```

FIG. 80: Labview program front panel

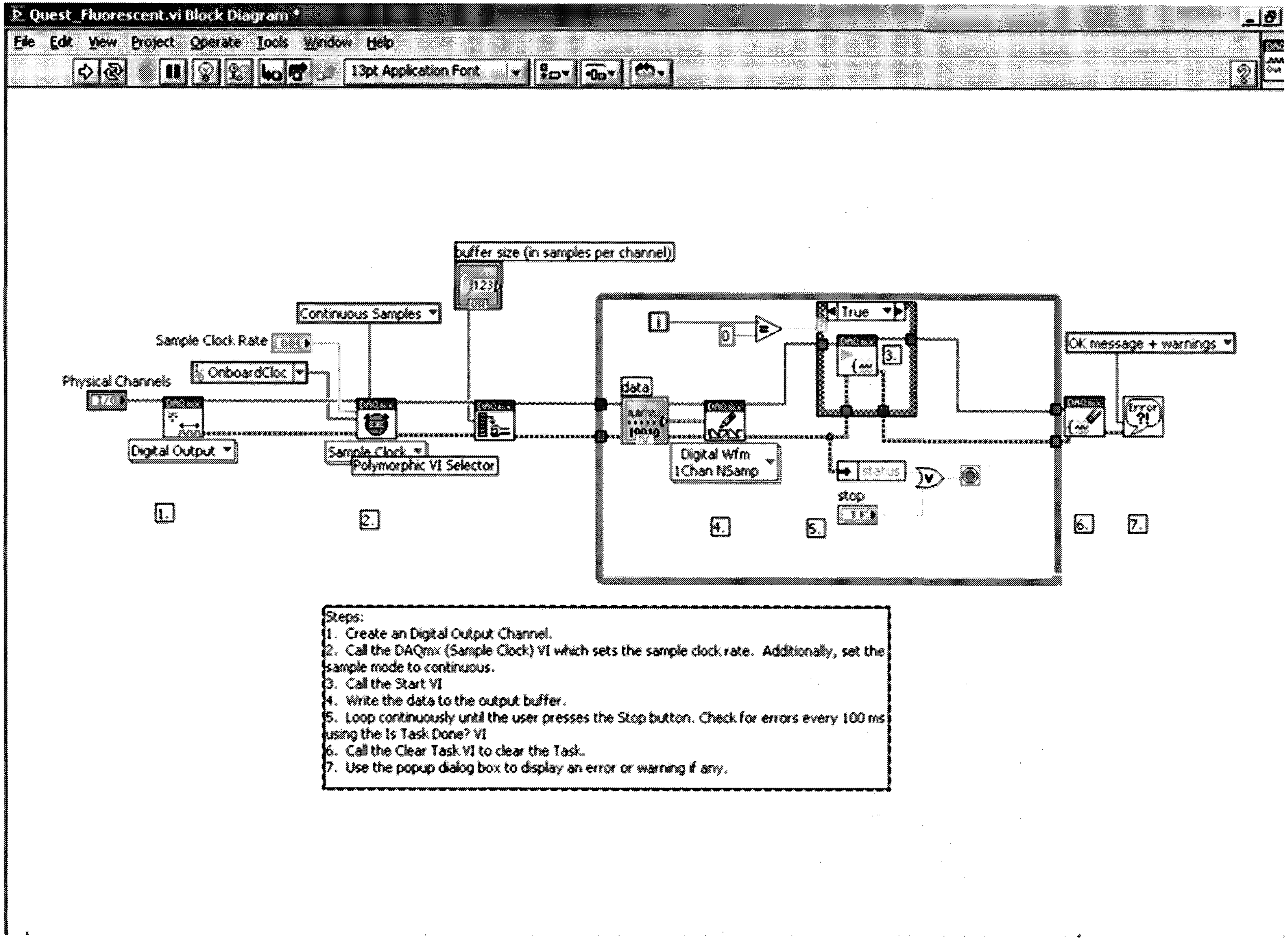

Steps:
1. Create an Digital Output Channel.
2. Call the DAQmx (Sample Clock) VI which sets the sample clock rate. Additionally, set the sample mode to continuous.
3. Call the Start VI
4. Write the data to the output buffer.
5. Loop continuously until the user presses the Stop button. Check for errors every 100 ms using the Is Task Done? VI
6. Call the Clear Task VI to clear the Task.
7. Use the popup dialog box to display an error or warning if any.

FIG. 81: Labview program control panel

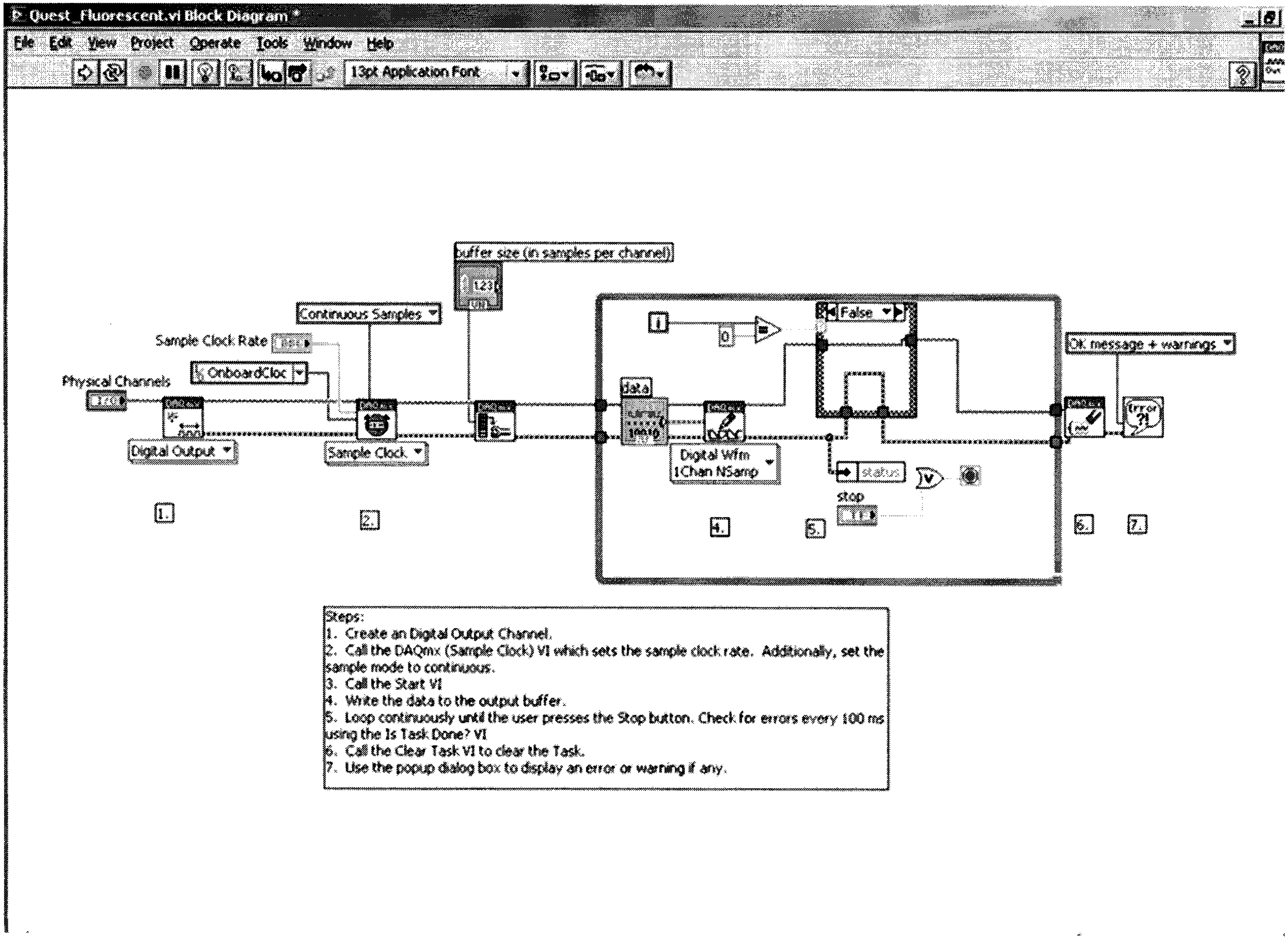

Steps:
1. Create an Digital Output Channel.
2. Call the DAQmx (Sample Clock) VI which sets the sample clock rate. Additionally, set the sample mode to continuous.
3. Call the Start VI
4. Write the data to the output buffer.
5. Loop continuously until the user presses the Stop button. Check for errors every 100 ms using the Is Task Done? VI
6. Call the Clear Task VI to clear the Task.
7. Use the popup dialog box to display an error or warning if any.

FIG. 82: Labview program control panel

VITA

Salim Balik
Department of Physics
Old Dominion University
Norfolk, VA 23529

EDUCATION

Doctor of Philosophy, Old Dominion University, Physics, December 2009

Master of Science, Old Dominion University, Physics, May 2004

Bachelor of Science, Bogazici University, Istanbul, Physics, June 2000

PUBLICATIONS

S. Balik, A.L. Win, M.D. Havey, Phys. Rev. A 80, 023404 (2009)

S. Balik, M.D. Havey, I.M. Sokolov, D.V. Kupriyanov, Phys. Rev. A 79, 033418 (2009)

S. Balik, R. Olave, C.I. Sukenik, M.D. Havey, V.M. Datsyuk, I.M. Sokolov, D.V. Kupriyanov, J. Mod. Optics 53, 2495 (2006)

S. Balik, R. Olave, C.I. Sukenik, M.D. Havey, V.M. Datsyuk, I.M. Sokolov, D.V. Kupriyanov, Phys. Rev. A72 (Rapid Communication), 051402 (2005)

S. Balik, P. Kulatunga, C.I. Sukenik, M.D. Havey, D.V. Kupriyanov, I.M. Sokolov, J. Mod. Optics 52, 2269 (2005)

D.V. Kupriyanov, I.M. Sokolov, N.V. Larionov, P. Kulatunga, C.I. Sukenik, S. Balik, and M.D. Havey, Phys. Rev. A69, 033801 (2004)

P. Kulatunga, C. I. Sukenik, S. Balik, M. D. Havey, D. V. Kupriyanov and I. M. Sokolov, Phys. Rev. A68, 033816 (2003)

Typeset using LaTeX.